

RESEARCH ARTICLE

10.1002/2016JE005135

Key Points:

- Depositional beds in Mars mountains dip away from peaks on all sides, showing that sediments piled up on high rather than in low points
- Unconformities in sedimentary mounds outline depositional units in a dome shape that thickens toward the center
- Modeling explains anticompensational stacking as a product of obliquity-driven intermittency and wind erosion at steep slopes

Supporting Information:

- Supporting Information S1
- Table S1

Correspondence to:

E. S. Kite,
kite@uchicago.edu

Citation:

Kite, E. S., J. Sneed, D. P. Mayer, K. W. Lewis, T. I. Michaels, A. Hore, and S. C. R. Rafkin (2016), Evolution of major sedimentary mounds on Mars: Buildup via anticompensational stacking modulated by climate change, *J. Geophys. Res. Planets*, 121, doi:10.1002/2016JE005135.

Received 5 AUG 2016

Accepted 12 OCT 2016

Accepted article online 14 OCT 2016

Evolution of major sedimentary mounds on Mars: Buildup via anticompensational stacking modulated by climate change

Edwin S. Kite¹, Jonathan Sneed¹, David P. Mayer¹, Kevin W. Lewis², Timothy I. Michaels³, Alicia Hore⁴, and Scot C. R. Rafkin⁵

¹Department of Geophysical Sciences, University of Chicago, Chicago, Illinois, USA, ²Morton K. Blaustein Department of Earth and Planetary Sciences, The Johns Hopkins University, Baltimore, Maryland, USA, ³SETI Institute, Mountain View, California, USA, ⁴Department of Earth Sciences, Brock University, St. Catharines, Ontario, Canada, ⁵Department of Space Studies, Southwest Research Institute, Boulder, Colorado, USA

Abstract We present a new database of >300 layer orientations from sedimentary mounds on Mars (Mount Sharp/Aeolis Mons, plus Nia, Juventae, Ophir, Ceti, Melas, Coprates, and Ganges Mensae). Together, these mounds make up ~1/2 of the total volume of canyon/crater-hosted sedimentary mounds on Mars. The layer orientations, together with draped landslides, and draping of rocks over differentially eroded paleodomes, indicate that for the stratigraphically uppermost ~1 km, the mounds formed by the accretion of draping strata in a mound shape. The layer-orientation data further suggest that layers lower down in the stratigraphy also formed by the accretion of draping strata in a mound shape. The data are consistent with terrain-influenced wind erosion but inconsistent with tilting by flexure, differential compaction over basement, or viscoelastic rebound. We use a simple model of landscape evolution to show how the erosion and deposition of mound strata can be modulated by shifts in obliquity. The model is driven by multi-Gyr calculations of Mars' chaotic obliquity and a parameterization of terrain-influenced wind erosion that is derived from mesoscale modeling. The model predicts that Mars mound stratigraphy emerges from a drape-and-scrape cycle. Our results suggest that mound-spanning unconformities with kilometers of relief emerge as the result of chaotic obliquity shifts. Our results support the interpretation that Mars' rocks record intermittent liquid-water runoff during a $\gg 10^8$ yr interval of sedimentary rock emplacement.

1. Introduction

Understanding how sediment accumulated is central to interpreting the Earth's geologic records [Allen and Allen, 2013; Miall, 2010]. The only other planet known to host an extensive sedimentary record is Mars. Gale crater and the Valles Marineris (VM) canyon system contain some of Mars' thickest (2–8 km) and best exposed sequences of sedimentary rock [Malin and Edgett, 2000; Milliken et al., 2010]. "The origin of (these sedimentary) mounds is a major unresolved question in Mars geology" [Grotzinger and Milliken, 2012]. The mounds are thought to have formed <3.7 Ga, relatively late in Mars' aqueous history and many contain sulfates that precipitated from aqueous fluids [Gendrin et al., 2005; Bibring et al., 2006; Mangold et al., 2008; S. L. Murchie et al., 2009]. The fluid source could be groundwater, rain, or snowmelt [Andrews-Hanna et al., 2010; Kite et al., 2013b]. Proposed depositional scenarios [Nedell et al., 1987; Lucchitta et al., 1992] range from primarily aeolian sedimentation in a climate dry enough that aeolian erosion could define moats around the growing mounds [Catling et al., 2006; Michalski and Niles, 2012; Kite et al., 2013a], through sand/dust cementation in horizontal playa-lake beds [Andrews-Hanna et al., 2010; Fueten et al., 2008; S. Murchie et al., 2009], to fluvial sediment transport from canyon/crater rims into canyon/crater-spanning lakes [Grotzinger et al., 2015]. At Gale crater, aeolian processes contributed to the deposition of the mound, evidenced by preserved bedforms within the stratigraphy [Milliken et al., 2014; Banham et al., 2016]. Following the depositional era, aeolian erosion cut into the rocks, exposing layers and perhaps deepening moats [Day and Kocurek, 2016].

These paleoenvironmental scenarios make contrasting predictions for the orientations of mound sediment layers and unconformities. If layers dip away from mound crests and layers have been little tilted since the time of deposition, then the mounds formed as mounds (similar to ice mounds within Mars' polar craters) [e.g., Brothers and Holt, 2016]. By contrast, gravity-driven deposition predicts layers that were originally flat lying or oriented away from crater walls or canyon walls, with the modern topography resulting entirely from

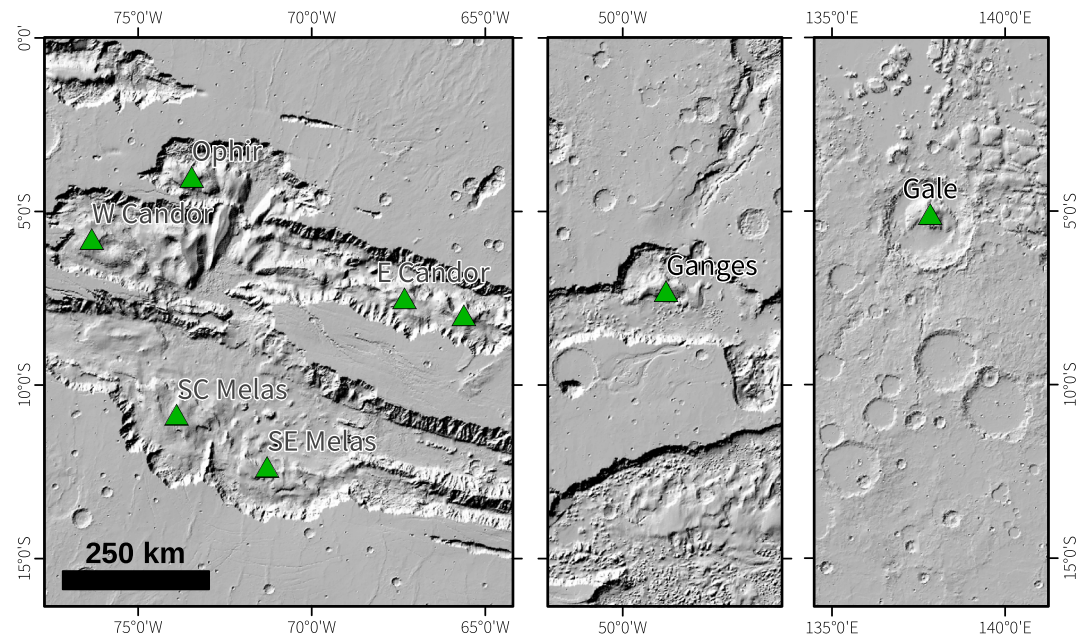


Figure 1. Location of mounds (green triangles) investigated in this work. Ophir Chasma contains Ophir Mensa, West Candor Chasma contains Ceti Mensa, East Candor Chasma contains Nia and Juventae Mensae, SC Melas Chasma contains Melas Mensa, SE Melas Chasma contains Coprates Chasma, Ganges Chasma contains Ganges Mensa, and Gale Crater contains Mount Sharp/Aeolis Mons. Background is Mars Orbiter Laser Altimeter shaded relief.

later erosion. The full internal architecture of Mars' largest sedimentary rock mounds cannot be directly observed but can be inferred from outcrop measurements of layer orientations and unconformities [Okubo *et al.*, 2008].

Layer-orientation measurements for Mars are obtained using orbiter image stereopairs to construct digital terrain models (DTMs) that form the basis for fitting planes to traces of stratigraphic surfaces [Lewis *et al.*, 2008]. From orbit it is usually not possible (due to limited resolution) to distinguish the traces of beds from the traces of lower order bounding surfaces, although both should closely correspond to basin topography at around the time of deposition (section 2.2). These fitted planes usually dip in a downslope direction but may suffer from downslope bias [e.g., Fueten *et al.*, 2006]. However, consensus on the interpretation of Mars layer data has been hindered by doubts about the accuracy of layer orientations measured from orbiter image data, the possibility that layer orientations do not reflect paleoslopes, and the absence of a physical mechanism that could account both for layer orientations and for Mars' large unconformities.

Corresponding to this lack of consensus in data interpretation, there are two end-member views of how Mars' mounds formed:

1. In one view, craters/canyons were fully filled by flat-lying or shallowly dipping strata, e.g., playa deposits or fluviodeltaic deposits (Figure 1a), and later underwent extensive erosion to their present form [Malin and Edgett, 2000; Andrews-Hanna *et al.*, 2010], presumably through wind erosion [Kite *et al.*, 2013a; Day *et al.*, 2016]. In this view, the primary cause of nonhorizontal layer orientations is downslope measurement bias and/or postdepositional distortion (by flexure, landslides, soft-sediment deformation, tectonics, and differential compaction) [e.g., Nedell *et al.*, 1987; Metz *et al.*, 2010; Grotzinger *et al.*, 2015]. Preferential infilling of topographic lows through deposition (compensational stacking) is ubiquitous in well-studied aqueous sedimentary environments on Earth [Straub *et al.*, 2009]. Therefore, it is tempting to assume that Earth analogy, which has been used effectively to interpret sedimentary structures viewed by rovers [McLennan and Grotzinger, 2008; Grotzinger *et al.*, 2015], also holds at the scale of Mars basins.
2. In another view, the downslope layer tilts are primary. If this is correct, then mounds grew in place by net deposition of layers on preexisting topographic highs (anticompensational stacking) [e.g., Michalski and Niles, 2012; Kite *et al.*, 2013a]. This distinctively Martian mechanism is suggested by (i) growth of polar ice + dust + sand mounds by anticompensational stacking [Holt *et al.*, 2010; Conway *et al.*, 2012; Brothers

et al., 2013; *Brothers and Holt*, 2016]; (ii) the importance of aeolian sediment transport and slope winds on modern Mars [*Spiga et al.*, 2011; *Spiga*, 2011; *Kok et al.*, 2012; *Bridges et al.*, 2013; *Silvestro et al.*, 2013; *Kite et al.*, 2013a]; and (iii) the strong inference of layered-sediment accumulation via anticompensational stacking for some Mars equatorial layered sediments (the Medusae Fossae Formation) [*Bradley et al.*, 2002; *Zimbelman and Scheidt*, 2012; *Kite et al.*, 2015]. Dry conditions bring aeolian processes to the fore, whereas vigorous and sustained fluvial erosion would inhibit mound construction. Therefore, anticompensational stacking corresponds to a paleoenvironment where fluvial sediment transport is infrequent, consistent with models of Mars paleoclimate [*Kite et al.*, 2013b; *Mischna et al.*, 2013; *Segura et al.*, 2013; *Urata and Toon*, 2013; *Halevy and Head*, 2014; *Wordsworth et al.*, 2013; *Ramirez et al.*, 2014; *Kerber et al.*, 2015; *Wordsworth et al.*, 2015; *Wordsworth*, 2016; *Ramirez and Kasting*, 2017].

1.1. Outline

Here we construct a new database (section 2) of layer orientations (section 3) and unconformities (section 4) within Martian mounds, in order to constrain accumulation of sedimentary rocks (section 5). We also present a new model (section 6) of mound emplacement. Implications and tests are discussed in section 7, and conclusions are listed in section 8.

Our work has three purposes:

a) *To address concerns with the mounds-grew-as-mounds hypothesis of Kite et al.* [2013a].

These concerns are as follows:

- That layer orientations “have not been independently confirmed” [*Grotzinger et al.*, 2015];
- That layer orientations can be accounted for by differential compaction of originally horizontal layers over basement relief (basement = rocks that predate sedimentary infill), removing the need for slope-wind erosion during the depositional era [*Grotzinger et al.*, 2015].

We resolve these concerns in sections 2–5:

- Exhaustive tests show that layer orientations are accurate and reproducible and that layer-orientation errors (including downslope bias) are insignificant for the purpose of determining mound origin (section 2).
 - Layer orientations in VM mounds show an outward dip—a direction opposite that predicted for differential compaction over basement relief (section 3). Layer orientations in Gale are unlikely to result from differential compaction over a central ring or central peak [*Gabasova and Kite*, 2016] (section 3). Unconformity data and draped-landslide data show that the mounds grew by anticompensational stacking at least for the topmost ~1 km of the mounds (section 4). Below this level, the data suggest two options: (i) accretion of draping strata in a mound shape and (ii) slope-wind erosion sculpts precompact sedimentary deposits, which subsequently act as a mound shaped form over which later sediments may be differentially compacted (section 5).
- b) *To expand the database of High Resolution Imaging Science Experiment (HiRISE)-derived layer orientation data for Mars.* Using HiRISE [*McEwen et al.*, 2007] data, we gathered 182 new layer orientations from seven VM mounds and increased the number of independent layer orientations for the mound in Gale crater from 80 to 126, for a total of 308 (section 3). Together, these mounds make up ~½ of the total volume of canyon/crater-hosted sedimentary mounds on Mars. Our work builds on previous studies [e.g., *Fuete et al.*, 2006] but uses a procedure that is more accurate, includes error bars, and has been validated (section 2). Our database (supporting information Table S1) can be applied to many Mars geology problems. As one example, we test the prediction of *Kite et al.* [2013a] that systematically outward oriented dips should be common in Mars mounds (section 5).
- c) *To propose a new model for the major unconformities in Mars' mounds.* Our new analysis of stratigraphic surfaces previously reported as mound-spanning unconformities show that these commonly have a dome shape (section 4). In order to match these data, we introduce a new model (section 6) that quantitatively integrates temporal variations and spatial variations in Mars sedimentation—for the first time for ancient Mars sedimentary-mound analysis [see also *Howard*, 2007]. Our model successfully reproduces the shape of the observed unconformities (section 6).

To support these goals, we improved the SWEET (Slope-Wind Enhanced Erosion and Transport) model of *Kite et al.* [2013a]. *Kite et al.* [2013a] showed how slope-winds create mounds, provided that the crater/canyon is

larger than a critical size, and that long-term-average deposition rate is neither much larger nor much smaller than long-term-average wind-erosion rate (consistent with data) [Bridges *et al.*, 2012a, 2012b; Lewis and Aharonson, 2014]. Two features inherent to the relatively simple SWEET model are the absence of a physically realistic relationship between slope and shear stress, together with the lack of any explanation of mound-spanning unconformities. (Although steady forcing in SWEET can produce autogenic unconformities, the younger layers grow off to one side—rather than building on top of the thickest point of the main mound, as is commonly observed for Mars' mountains.) We solve these problems in our improved model, which we term SOURED (Stratigraphy with Obliquity-triggered Unconformities and Relief-influenced Erosion and Deposition). Specifically, we include realistic multi-Gyr calculations of Mars obliquity and a more realistic parameterization of terrain-influenced wind erosion derived from mesoscale modeling (Appendix A and Appendix B).

1.2. Geologic Scope and Geologic Context

For this study we selected sedimentary mounds that are voluminous, light-toned, show well-exposed off-horizontal layering, have good HiRISE stereopair coverage, and either host sulfates or are stratigraphically associated with sulfates (Figure 1). We further selected only mounds that sit within deep, wide and steep-sided craters/canyons, attributes that favor slope winds. In both VM and Gale, the erodible sedimentary mounds are contained within craters/canyon walls made up of much-less-erodible basement materials. The eight mounds (mensae) that were selected are Nia (7.6°S, 67.2°W), Juventae (8.0°S, 65.6°W), Mount Sharp/Aeolis Mons (5.1°S, 137.8°E), Ophir (4.0°S, 73.5°W), Ceti (6.1°S, 75.8°W), Melas (10.7°S, 74.1°W), Coprates (12.5°S, 71.5°W), and Ganges (7.2°S, 48.9°W)—all at <15° latitude (Figure 1). We excluded the well-studied mounds Juventae Chasma [Catling *et al.*, 2006; Bishop *et al.*, 2009] and Candor Mensa [Mangold *et al.*, 2008; Ferguson *et al.*, 2014; Fueten *et al.*, 2014]. (The criteria exclude a large number of sedimentary accumulations on Mars: e.g., plateau deposits [Mawrth, Loizeau *et al.*, 2015; Meridiani Planum, Hynek and Phillips, 2008; NE Arabia, Fassett and Head, 2007], the clay-bearing Terby deposits [Ansan *et al.*, 2011], the free-standing Medusae Fossae mounds [Bradley *et al.*, 2002; Burr *et al.*, 2009; Zimbelman and Scheidt, 2012; Kite *et al.*, 2015], the NE Syrtis sulfate deposits [Ehlmann and Mustard, 2012] and veneers and smaller mounds in and around VM [e.g., Milliken *et al.*, 2008; Thollot *et al.*, 2012; Weitz and Bishop, 2016].) Gale's mound (Aeolis Mons; also known as Mount Sharp) is the largest among 50 documented crater-hosted mounds outside the polar regions [Bennett and Bell, 2016], is the primary science target of Mars Science Laboratory (MSL) [Mars Science Laboratory (MSL) Extended Mission Plan, 2014], and has the best HiRISE stereopair coverage of any within-crater mound, justifying our emphasis on this within-crater mound.

The eight mounds studied here were among the first Mars sedimentary rock accumulations to be described [Malin and Edgett, 2000; Malin *et al.*, 2010]. The rocks formed relatively late in Mars' aqueous history and contain hematite and sulfates [Christensen *et al.*, 2001; Gendrin *et al.*, 2005; Bibring *et al.*, 2007; Weitz *et al.*, 2008; S. L. Murchie *et al.*, 2009; Roach *et al.*, 2010; Fassett and Head, 2011; Ehlmann *et al.*, 2011; Ferguson *et al.*, 2014]. Most of our layer-orientation data comes from the VM mounds ("Interior Layered Deposits," ILD). Crosscutting relationships and contrasts in texture, thermal inertia, erodibility, and mineralogy between sedimentary-mound rocks and canyon-wall rocks all indicate that the ILD accumulated after the canyons formed [Peterson, 1981; Lucchitta, 2010; Okubo *et al.*, 2008; Schultz, 2002; Andrews-Hanna, 2012a; see also Montgomery *et al.*, 2009].

Mound stratigraphy (Figure 2), which usually includes at least one mound-spanning unconformity, is described in a large literature [e.g., Malin and Edgett, 2000; Le Deit *et al.*, 2013; Anderson and Bell, 2010; Milliken *et al.*, 2010; Thomson *et al.*, 2011; Grotzinger and Milliken, 2012]. The following trends are a useful guide to correlation. (1) Within-mound materials below the lowest mound-spanning unconformity within a mound usually, but not exclusively, correspond to the "laterally continuous sulfate" orbital facies of Grotzinger and Milliken [2012]. (2) Materials found above the lowest mound-spanning unconformity within a mound usually, but not exclusively, correspond to the "rhythmite" of Grotzinger and Milliken [2012]. (3) Darker-toned indurated materials draping the present topography usually correspond to the widespread "thin mesa" units of Malin and Edgett [2000] (Figure 2). We did not measure layer orientations on thin mesa units.

The VM and Gale mounds are no older than the Noachian/Hesperian boundary, based on the timing of VM formation, and on the crater-retention age of Gale's ejecta [Anderson *et al.*, 2001; Thomson *et al.*, 2011; Le Deit *et al.*, 2013]. The topmost sedimentary rocks could be as young as Upper Amazonian [Mangold

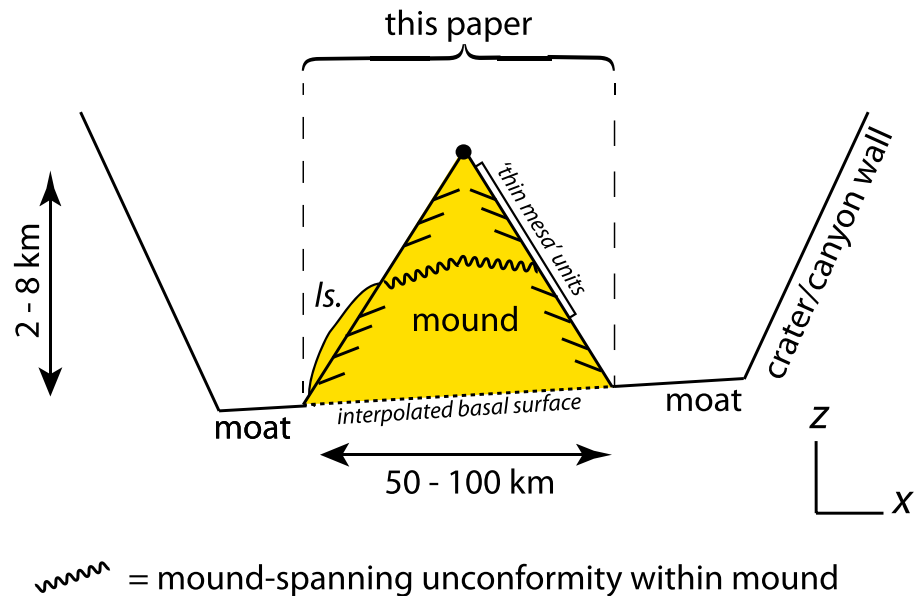


Figure 2. Schematic shows an idealized sedimentary rock mound within an erosion-resistant container (crater or canyon). In this paper, we focus on rocks within the topographically defined mound (ignoring moat rocks and wall rocks). We neglect $\ll 100$ m thick “thin mesa” units that drape modern topography (white outline). Layer orientations constrain mode (s) of mound emplacement (section 3). Unconformity data and associated isochores, as well as draped landslides (“Is.”), further constrain basin evolution for the upper part of the mounds (section 4).

et al., 2010; Thollot *et al.*, 2012]. Therefore, crater chronology permits a $\gg 100$ Myr interval of sedimentary rock accumulation. This is consistent with other methods [Lewis and Aharonson, 2014].

The physical processes and patterns of deposition for all these rock units are uncertain, and in the words of Grotzinger and Milliken [2012], “[m]easurements of the strike, dip, and stratal geometries of layers within these units would help to place further constraints on their mode(s) of emplacement.” Such measurements are the focus of the work presented here. Remarkably, despite the size of the mound-spanning unconformities of Mars, we are not aware of any previous physical model for their origin.

1.3. Relation to Rover Data

Coanalysis of rover data and orbiter data can increase the science value of both [Arvidson *et al.*, 2006; Fraeman *et al.*, 2013; Arvidson *et al.*, 2015; Lapôtre *et al.*, 2016; Stack *et al.*, 2016]. In 2012 the Mars Science Laboratory (MSL) rover landed successfully in Gale crater, ~ 6 km away from the layers in Mount Sharp/Aeolis Mons where layer orientations are reported [Le Deit *et al.*, 2013; Kite *et al.*, 2013a; Stack *et al.*, 2013]. Rover results to date from Gale crater are interpreted as primarily fluviolacustrine deposits [Grotzinger *et al.*, 2014], which are overlain unconformably by later aeolian sands [Lewis *et al.*, 2015; Fraeman *et al.*, 2016]. Our unconformity results based on analysis of orbiter data echo recent rover discoveries in the Gale moat [Watkins *et al.*, 2016]. As MSL continues its drive [MSL Extended Mission Plan, 2014], the rover’s instruments may decisively constrain the sediment transport mechanism for the lower layers of Gale crater’s mound (section 7). As of mid-2016, the rover is ~ 5 km from the sulfate-bearing layers where layer orientations are reported. Throughout the traverse to date, Mastcam rover imagery has resolution at the sulfate-bearing layers where layer orientations are reported that is inferior to HiRISE. Specifically, the Mastcam M100 has an angular resolution of $74 \mu\text{rad/pixel}$ (85 cm/pixel for a 25° slope, 37 cm/pixel for a vertical target at 5 km) [Malin *et al.*, 2010]. This compares to HiRISE (from 250 km: 28 cm/px for a 25° slope, 25 cm/px for a horizontal target). Due to foreground obstructions, and edge-on views, layers are more easily visualized in orbiter imagery. The ChemCam Remote Micro-Imager (RMI) has a nominal resolution of $20 \mu\text{rad/pixel}$ and its potential for long-range stereophotogrammetry is exciting [Le Mouélic *et al.*, 2015]. However, we are not aware of any suitable Mount Sharp/Aeolis Mons RMI stereopairs. Because of the (current) superiority of orbiter images compared to rover images for the purposes of stereo determination of layer orientations within the sulfate-bearing layers,

Table 1. Table of DTMs

Crater/Canyon	Mound	DTM Location	Image 1	Image 2	DTM Posting
<i>DTMs Produced for This Study</i>					
SE Melas	Coprates Mensa	13°S 289°E	ESP_027723_1670	ESP_027746_1670	1 m/pixel
SE Melas	Coprates Mensa	13°S 290°E	ESP_035450_1670	ESP_034250_1670	1 m/pixel
SE Melas	Coprates Mensa	13°S 288°E	ESP_028567_1680	ESP_027657_1680	2 m/pixel
Ophir	Ophir Mensa	4°S 286°E	ESP_034949_1760	ESP_034738_1760	1 m/pixel
Ophir	Ophir Mensa	4°S 286°E	ESP_015974_1760	ESP_020220_1760	1 m/pixel
Ophir	Ophir Mensa	4°S 286°E	PSP_008893_1760	PSP_008458_1760	1 m/pixel
Ophir	Ophir Mensa	4°S 286°E	ESP_017886_1760	ESP_017675_1760	1 m/pixel
SC Melas	Melas Mensa	10°S 286°E	PSP_010660_1700	PSP_007812_1700	1 m/pixel
SC Melas	Melas Mensa	10°S 286°E	PSP_005953_1695	PSP_002630_1695	1 m/pixel
SC Melas	Melas Mensa	11°S 286°E	PSP_001377_1685	PSP_001852_1685	2 m/pixel
SC Melas	Melas Mensa	11°S 286°E	ESP_012361_1685	ESP_012572_1685	2 m/pixel
SC Melas	Melas Mensa	11°S 285°E	ESP_033169_1690	ESP_032747_1690	1 m/pixel
SC Melas	Melas Mensa	10°S 285°E	ESP_028633_1695	ESP_034382_1695	1 m/pixel
West Candor	Ceti Mensa	6°S 283°E	PSP_003896_1740	PSP_002841_1740	1 m/pixel
East Candor	Juventae Mensa	8°S 294°E	ESP_017411_1715	ESP_017266_1715	1 m/pixel
East Candor	Juventae Mensa	7°S 294°E	ESP_037586_1725	ESP_037731_1725	1 m/pixel
East Candor	Nia Mensa	8°S 293°E	ESP_034896_1725	ESP_036452_1725	1 m/pixel
East Candor	Nia Mensa	7°S 292°E	ESP_031982_1730	ESP_031916_1730	1 m/pixel
East Candor	Nia Mensa	7°S 292°E	ESP_014154_1730	ESP_014431_1730	2 m/pixel
Gale	Mt. Sharp/Aeolis Mons	5°S 137°E	PSP_006855_1750	PSP_007501_1750	1 m/pixel
Gale	Mt. Sharp/Aeolis Mons	5°S 137°E	ESP_012195_1750	ESP_012340_1750	1 m/pixel
Gale	Mt. Sharp/Aeolis Mons	6°S 138°E	PSP_003176_1745	PSP_002464_1745	1 m/pixel
Gale	Mt. Sharp/Aeolis Mons	5°S 138°E	ESP_016375_1750	ESP_016520_1750	1 m/pixel
Gale	Mt. Sharp/Aeolis Mons	5°S 138°E	ESP_030880_1750	ESP_030102_1750	1 m/pixel
Gale	Mt. Sharp/Aeolis Mons	5°S 137°E	ESP_012907_1745	ESP_013540_1745	1 m/pixel
<i>Additional DTMs From Kite et al. [2013a], Produced and Analyzed by K.W. Lewis. 2° (Worst-Case) Error Assumed</i>					
Gale	Mt. Sharp/Aeolis Mons	5°S 138°E	PSP_008437_1750	/PSP_008938_1750	1 m/pixel
Gale	Mt. Sharp/Aeolis Mons	5°S 137°E	ESP_023957_1755	ESP_024023_1755	1 m/pixel
Gale	Mt. Sharp/Aeolis Mons	5°S 137°E	PSP_001488_1750	PSP_001752_1750	1 m/pixel
Gale	Mt. Sharp/Aeolis Mons	5°S 137°E	PSP_009149_1750	PSP_009294_1750	1 m/pixel
Gale	Mt. Sharp/Aeolis Mons	6°S 138°E	ESP_014186_1745	ESP_020410_1745	1 m/pixel
<i>Additional DTM Produced and Traced by Okubo [2014], Traces Not Included in the Main Database</i>					
West Candor	Ceti Mensa	7°S 284°E	PSP_001641_1735	PSP_002063_1735	1 m/pixel
<i>Additional DTMs Produced and Analyzed by Alicia Hore [Hore, 2015], Summarized in Figure 8f but Not Included in the Main Database</i>					
Ganges	Ganges Mensa	7°S 311°E	PSP_006519_1730	PSP_007020_1730	n.a.
Ganges	Ganges Mensa	7°S 311°E	ESP_013059_1725	ESP_012993_1725	n.a.
Ganges	Ganges Mensa	7°S 311°E	PSP_002550_1725	PSP_003618_1725	n.a.
Ganges	Ganges Mensa	7°S 312°E	ESP_011648_1730	ESP_011582_1730	n.a.
Ganges	Ganges Mensa	7°S 311°E	ESP_018162_1730	ESP_018633_1730	n.a.
Ganges	Ganges Mensa	7°S 311°E	PSP_007877_1725	PSP_007521_1725	n.a.

our work is largely based on orbiter data analysis. Rover imagery shows apparent dips in Mount Sharp/Aeolis Mons layers that are qualitatively consistent with dips obtained from HiRISE DTMs.

2. Data Analysis Methods

2.1. DTM Production Method

HiRISE DTMs and orthoimages were used as the basis for layer tracing (section 1.3). We produced Context Camera (CTX) and HiRISE DTMs using the NASA Ames Stereo Pipeline (ASP) [Moratto et al., 2010; Beyer et al., 2014; Shean et al., 2016]. As part of this processing, we developed a set of scripts that act as wrappers around the ASP routines, which increase the level of automation and computational efficiency of the DTM production [Mayer and Kite, 2016]. Initial CTX point clouds were aligned to Mars Orbiter Laser Altimeter (MOLA) shot data using an iterative closest points algorithm before being interpolated to DTMs and orthoimages with a grid spacing of 18 m. Initial HiRISE point clouds were then similarly aligned to the CTX DTMs before being interpolated to DTMs and orthoimages with a grid spacing of 1 m (2 m for HiRISE input collected in 2 × 2 binning mode; Table 1).

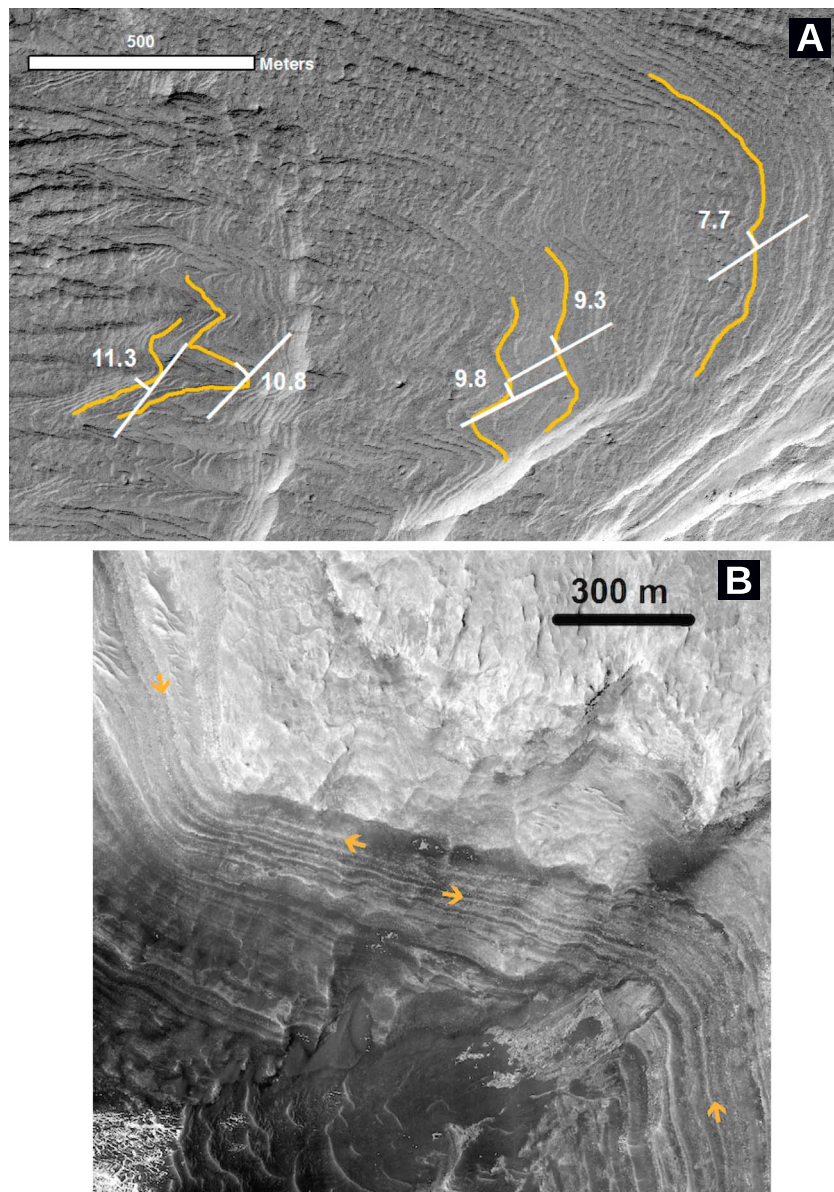


Figure 3. (a) Traces and corresponding dips ($^{\circ}$) for part of the ESP_017411_1711/ESP_017266_1715 stereopair. (b) Detailed trace identification for part of the reentrant canyon shown in Figure 4a (ESP_012907_1745/ESP_013540_1745 stereopair.)

As an independent check on the quality of our DTM production workflow, we compared three of our HiRISE DTMs to DTMs generated from the same HiRISE stereopairs and available from the Planetary Data System (these PDS DTMs were produced using SOCET SET) [Kirk *et al.*, 2008]. Because we are primarily interested in the vertical differences between DTMs produced using different methods, we coregistered the PDS-released products to our products by using tie points selected manually on the orthoimages and then applying the resulting transform to the DTMs in order to eliminate any horizontal offsets. We then subtracted the elevation values of our DTMs from the PDS-released DTMs to create a series of difference rasters. For the purposes of the layer orientation measurements in this paper, the most important differences were broad tilts across the entire image. We inspected the resulting difference rasters to characterize tilts. These tilts were 0.2° , 0.17° , and 0.09° for the three DTMs investigated, which is much smaller than our error bars.

In addition to the stereo DTMs, digital models of each mound were extracted from MOLA gridded data. Mound basal surfaces were defined from the MOLA elevation data using cubic polynomial interpolation

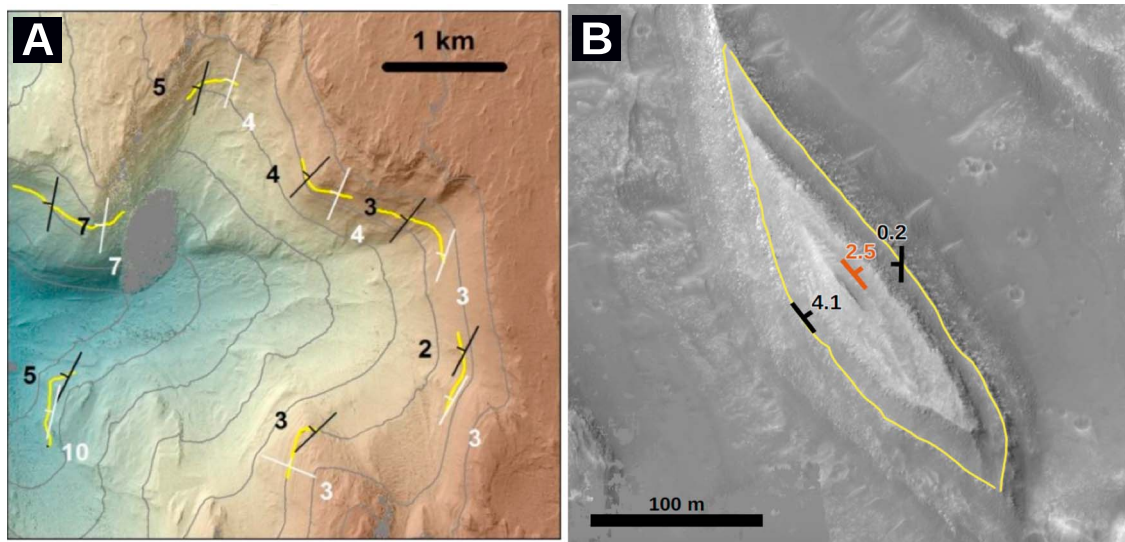


Figure 4. To show that downslope bias does not affect our conclusions. (a) Examples of layers (yellow) showing similar dips whether traced on CTX DTMs (white) or HiRISE DTMs (black) in a reentrant canyon at 137.2°E 5.3°S. Gray contours show 100 m topographic intervals. Brown is high. Backdrop is HiRISE DTM shaded relief. (b) Example of arcuate subsets of a layer (yellow) on a circular mesa. Mesa-flanks slope at $\sim 23^\circ$, yet plane fits to arcuate subsets of the layer (black symbols) show no downslope bias relative to the plane fit to the entire elliptical trace (red symbol).

within-mound edges. This allowed us to estimate the volume of all mounds. Mound crestlines and edges were drawn by visual inspection of Thermal Emission Imaging System (THEMIS) mosaics.

2.2. Layer Tracing Method

Layer traces were carried out by visual inspection using orthorectified HiRISE images and corresponding DTMs (Figure 3), following the method of Lewis *et al.* [2008]. Most traces were >150 m long. For Gale's mound, we included data from Kite *et al.* [2013a]. Layer orientations were calculated for the best fit plane for each layer trace. Layers were rejected if their pole error was $>2^\circ$ (calculated following Lewis *et al.* [2008], which is a conservative approximation to a 95% regression-error estimate). The mean pole error in the whole database is 0.98° .

Layers were traced on the HiRISE DTMs listed in Table 1. Linear subhorizontal features observed in Mars outcrops from orbit might correspond to depositional beds, first-order bounding surfaces, deflation surfaces, diagenetic bands, or even buttress unconformities or wave runup features [Rubin and Hunter, 1982; Kocurek, 1988; Edgar *et al.*, 2012; Parker *et al.*, 2014]. Where rovers have explored sulfate-rich rocks on Mars, shallow/early diagenesis blurs the distinction between diagenetic bands and depositional beds. (Later diagenetic fronts need not be parallel to depositional beds) [Davies and Cartwright, 2002; Borlina *et al.*, 2015]. Therefore, we aimed to trace stratigraphic surfaces that closely corresponded to basin-scale topography at the time of deposition (we refer to these stratigraphic surfaces as "layers"). To maximize the likelihood of tracing layers, we followed Lewis [2009] and avoided drawing traces that crossed faults in the rocks where displacement may have occurred, and areas adjacent to faults where folding can distort layers into nonplanar surfaces. We avoided tracing on landslides, convolute folding [Metz *et al.*, 2010], superscoops, zones of apparent soft-sediment deformation, and thin mesa materials [Malin and Edgett, 2000]. Examples of the trace locations and corresponding results are shown in Figure 3. The fine scale and high degree of lateral continuity of layers (e.g., Figure 3) is strong evidence that the observed layering represents true depositional bedding and not, for instance, diachronous facies boundaries or late-diagenetic alteration horizons [Le Deit *et al.*, 2013; Stack *et al.*, 2013; Milliken *et al.*, 2014].

Errors in tracing a layer on a slope on an orthorectified image will produce a downslope bias in plane fits to the trace using the corresponding DTM. Four tests show that downslope bias in our data set does not affect our conclusions:

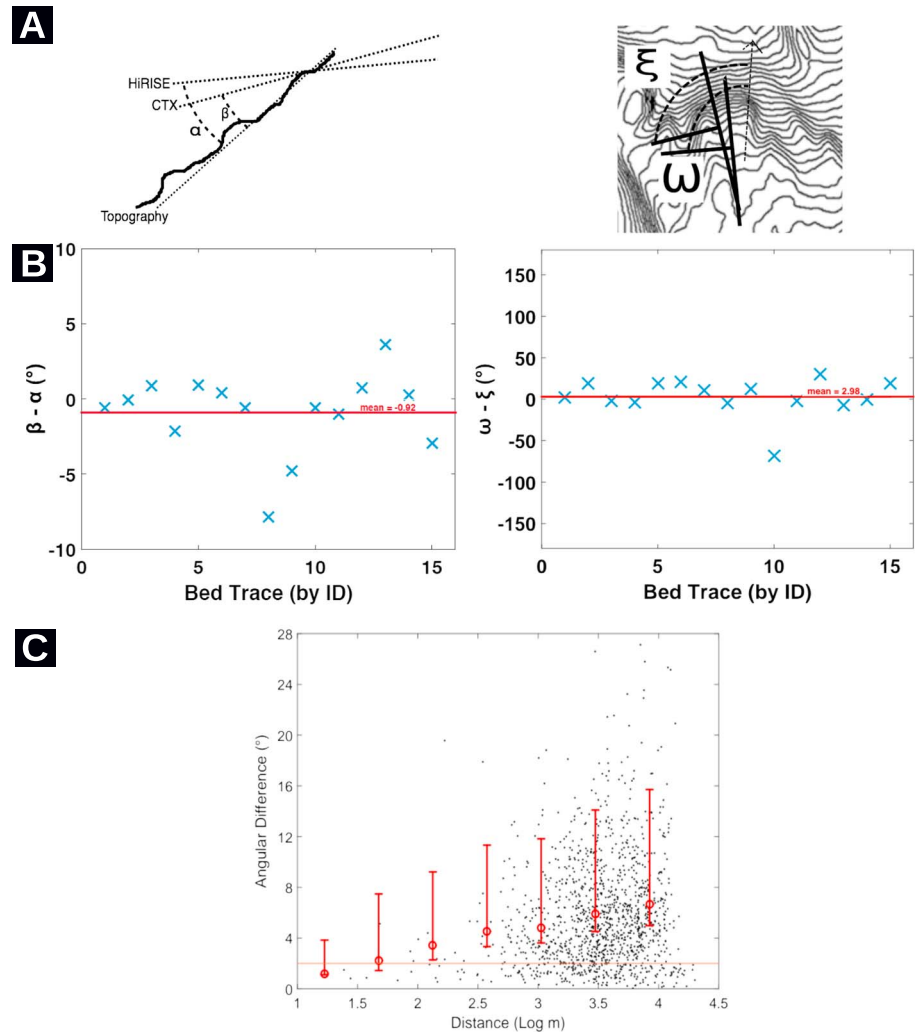


Figure 5. CTX-versus-HiRISE layer orientation test using layer traces from the area of Figure 4a. (a) Cartoon showing how CTX-derived and HiRISE-derived layer orientations are projected onto the plane containing the downslope (topography) vector. (b) Results of HiRISE-CTX comparison. (c) Quantifying geologic noise: showing divergence between pole-fits to layers as a function of separation. Orange line shows 2° threshold. Red circles mark the mean of angular differences, binned by separation. Red whiskers correspond to the standard deviation of the logarithms of the binned data.

1. *Reentrant-canyon test* [Kite et al., 2013a]. For the reentrant canyon at $137.2^\circ\text{E } 5.3^\circ\text{S}$ (Figure 4a), a dominant direction of layer azimuth contrasts with a nearly complete radial rotation in dominant downslope direction. We found that layers dip in a systematic direction, typically perpendicular to local downslope. This rules out severe downslope bias.
2. *Resolution-sensitivity test.* We compared the traces of identical layers at different image grid spacings (Figure 5). If downslope bias affects the HiRISE layer orientations (1 m/pixel elevation model), then the same layers traced on CTX (18 m/pixel DTM) will suffer a bias that is more severe. For layers in the canyon at $137.2^\circ\text{E } 5.3^\circ\text{S}$ (Figure 5), we obtained two metrics of downslope bias (Figure 5): (a) the angle between the best fit plane and local topography projected onto the vertical plane parallel to steepest topographic slope and (b) the map-plane angle between the best fit plane and the topographic downslope. We do not find any systematic tendency for the CTX layer orientations to be rotated downslope relative to the HiRISE layer orientations, suggesting that the HiRISE bias is itself small.
3. *Circular-mesa test* (Figure 4b and Table 2). In rare cases, conical topographic features show layers that can be traced in a closed loop, rather than an open curve. Because there is no obvious “downslope direction” for closed-loop traces, the topography-induced measurement error (downslope bias) of closed-loop

Table 2. Downslope Bias Is Shown to Be Small by Elliptical-Mesa Check (Figure 4b)^a

HiRISE Image No.	Mesa Latitude (deg)	Mesa Longitude (deg)	Full Dip (deg)	Full Direction (° CCW From East)	Dip (deg)	Dip Direction (° CCW From East)	Topographic Dip (deg)	Topographic Dip Direction (° CCW From East)	Full Difference From Topographic (deg)	Cut Difference From Topographic (deg)	Proximity to Topographic Versus Full (deg)
ESP_012551_1750	-4.852	137.255	3.03	-150.44	1	1.09	-105.03	21.67	21.67	21.01	2.34
ESP_012551_1750	-4.948	137.242	3.53	149.11	2	1.77	-151.54	23.40	20.45	-163.19	-1.21
ESP_012551_1750	-4.97	137.271	2.62	117.80	1	8.51	166.50	28.19	25.17	178.68	5.22
ESP_016375_1750	-5.346	138.528	2.50	39.00	2	2.04	44.01	29.52	32.39	6.61	4.46
ESP_016375_1750	-5.335	138.533	0.62	89.42	1	10.42	174.76	33.70	34.58	10.01	-9.24
ESP_012361_1685	-11.290	-74.68173	5.21	172.61	2	2.66	98.69	16.19	15.06	178.11	-0.85
ESP_012361_1685	-11.220	-74.69151	3.13	-108.08	1	0.16	179.08	26.73	24.23	34.38	-2.62
ESP_012361_1685	-11.220	-74.69151	3.13	-108.08	2	4.11	36.29	18.46	20.91	-153.49	-1.61
ESP_012361_1685	-11.220	-74.69151	3.13	-108.08	2	0.73	127.35	26.73	26.38	34.38	-0.40
ESP_012361_1685	-11.220	-74.69151	3.13	-108.08	2	4.11	36.29	18.46	18.75	-153.49	-3.77
ESP_012361_1685	-11.220	-74.69151	3.13	-108.08	1	7.07	169.71	12.65	7.75	-171.69	1.40
ESP_012361_1685	-11.220	-74.69151	3.13	-108.08	2	5.21	-169.60	8.10	12.78	25.84	-0.41
ESP_012361_1685	-11.220	-74.69151	3.13	-108.08	1	3.32	-78.37	6.09	6.36	-27.64	1.62
ESP_012361_1685	-11.220	-74.69151	3.13	-108.08	2	3.87	-144.70	10.65	9.86	-175.29	2.29

^aFull refers to the entire elliptical trace. "Cut" refers to an arcuate subset of the elliptical layer, chosen to be oriented along the long axis of the elliptical mesa (this is the worst case). The final column shows the rotation of the pole to the best fit plane into the downslope direction, which is positive when data are consistent with downslope rotation and negative when the data show upslope rotation. The highlighted rows correspond to traces that are shown in Figure 4b.

traces is close to zero. After tracing seven such mesa-encircling layers, we split each elliptical trace along its ~200 m long major axis (the worst case for downslope bias). This creates 14 test traces with a clear downslope direction and a high aspect ratio (Table 2)—again, the worst case for downslope bias. The DTM under each trace was clipped by minimum bounding rectangle, and best fit planes were fit to each of the traces and to the elevation data contained within the minimum bounding rectangle for that trace. The best fit poles to the halved test cuts are consistent with zero downslope rotation. For $n = 14$, test cuts are -0.2° closer to topography on average (i.e., we find the unexpected result of upslope rotation), with a standard deviation of 3.7° , minimum of -9.2° , and maximum of 5.2° .

4. *Geologic-control test.* HiRISE DTM layer-dip measurements made using the same technique show near-horizontal layers in areas where near-horizontal layers are expected from geological context. Specifically, near-horizontal layers have been measured from Eberswalde's delta topsets, Holden's delta topsets, and the Juventae plateau layered deposits [Irwin *et al.*, 2015; Stack *et al.*, 2013]. These near-horizontal measurements are reported from places where the present-day erosional surface slopes steeply and so might be expected to produce large downslope bias. This geologic "control case" strongly suggests that off-horizontal Mars layer orientations measured from HiRISE DTMs are not artifacts of downslope bias, but rather geological.

Although our checks indicate that downslope bias does not affect our conclusions, our database includes a small number (<5) of measurements where downslope bias may set the dip azimuth. These measurements all have a minimum bounding rectangle that has an aspect ratio greater than 8:1, i.e., small curvature.

We found same-worker reproducibility within error. Formal DTM precision makes a negligibly small contribution to the error. Consistency between measurements by workers in the University of Chicago and Johns Hopkins University labs using the same procedure was demonstrated. Between lab reproducibility for poles-to-layer-planes in NW Gale (JHU versus Chicago) was 1.3° on average (standard deviation

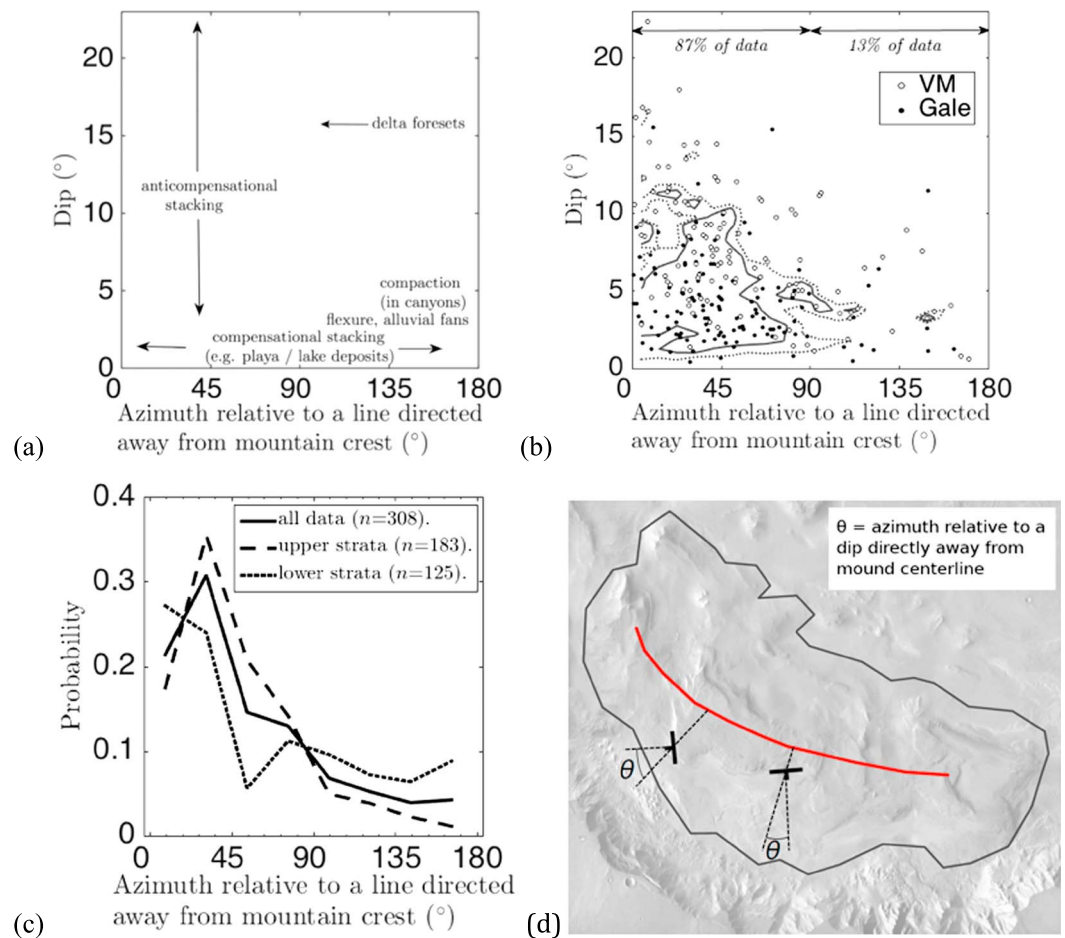


Figure 6. Layer-orientations summary: (a) Expectations for primary depositional orientation [Leeder, 2011; Moore and Howard, 2005; Davis, 2007; Kite et al., 2013a; Grotzinger et al., 2015]. “Delta foresets” refers to a container-wall sediment source. (b) Results, for measurements above the interpolated basal surfaces of the mounds. Solid and dashed contours enclose 50% and 68% of data, respectively, after accounting for heteroskedastic error. Marginalizing over dip, 87% of the azimuth data lie within 90° of a line directed away from mountain crest. (c) Distribution of layer orientations relative to elevation above interpolated basal surface of mound (lower strata are ≤ 0.5 km above mound base; upper strata are > 0.5 km above mound base; 22.5° bins).

tion 1.0°, worst-case 3.7°, $n = 17$), which is less than our error bars. Outward dips at Mount Sharp/Aeolis Mons have been independently confirmed by Fraeman et al. [2013], Le Deit et al. [2013], and Stack et al. [2013].

Same-worker reproducibility averaged 1.3°, with a standard deviation of 1.0°. The same-worker reproducibility check layers were chosen to systematically span a range from smallest to largest ΔZ , where ΔZ is the absolute range of elevation values. We did not find any tendency for reproducibility to get worse with decreasing ΔZ . However, small- ΔZ traces remain sensitive to small-scale geologic variation (e.g., fractures and boulders), so caution is warranted in interpretation of individual traces with $\Delta Z < 3.5$ m (supporting information Table S1).

To quantify between measurement variations (geologic noise), we plotted (for each DTM) pairwise angular differences between the poles-to-layer-planes as a function of the pairwise separation between median $\{x, y\}$ positions of individual traces (Figure 5c). We found that the pairwise differences are well fit by a line that increases log-linearly with separation and intersects 180 m at $\sim 4^\circ$ (Figure 5c). Within-DTM differences in layer orientation can greatly exceed our error bars, and so are likely real (geological). These layer-orientation differences could be primary depositional features, or the result of short-wavelength postdepositional tilting.

Together, these tests show that our measurements are accurate and reproducible and that downslope bias does not affect our conclusions. We cannot exclude a selection bias (layers that dip close to slope will have corrugated outcrops that are easier to measure). However, our measurements cover many mounds and a broad range of stratigraphic elevation, minimizing this effect. For the purpose of understanding mound buildup, within-DTM scatter in the measurements (kilometer-wavelength geologic noise) sets the practical limit on interpretation—not measurement precision or accuracy.

Results are given in Figures 6–9 and section 3.

2.3. Fitting of Stratigraphic Surfaces Interpreted as Erosional Unconformities

We traced stratigraphic surfaces (interpreted by previous workers as erosional unconformities) in West Candor, Ophir, and Gale [Anderson and Bell, 2010; Thomson et al., 2011; Le Deit et al., 2013; Lucchitta, 2015]. We interpret the traces as unconformities on the basis of a sharp break in tone, erosional or layering style, crater density, or slope, at a stratigraphic level that, in at least one location, corresponds to an unconformity (shown by buried craters or by truncated layers) (e.g., Figure 9). In none of these cases is definitive unconformity mapping possible using CTX data alone, and complete HiRISE coverage is not available. In West Candor and Gale, we believe that the traces do correspond to major unconformities (e.g., Figure 9) and that our traces follow a stratigraphic surface sufficiently closely to determine the qualitative paleotopography (dome, trough, saddle, or roughly flat) and to put lower bounds on isochore measurements. Next, we made use of DTMs constructed using CTX stereo data (for Gale) or using MOLA data (for West Candor). For segments of the trace where we were confident about the location of the unconformity, we calculated the total relief (maximum elevation—minimum elevation) of the unconformity trace. Next, the digitized points were interpolated to form unconformity surfaces using (i) inverse distance weighting, (ii) planar interpolation, and (iii) quadratic global polynomial interpolation. In principle, the interpolation procedure is subject to a dome bias that is analogous to the downslope bias in layer-orientation fits. In practice, however, the greater than km total relief of the unconformity traces means that any such bias is unimportant for the purpose of determining the best fit shape of the stratigraphic surface. Following interpolation, we subtracted these surfaces from present-day topography to create thickness contours (isochores) for the material above the within-mound unconformities. Results are given in Figures 10–12 and section 4.1.

2.4. Identification of Draped Landslides

We identified mass-wasting units (flows, slides, spreads, falls, and topples), which we refer to as “landslides,” using THEMIS and CTX images. Comparison with a preliminary U.S. Geological Survey geologic map of the Central Valles Marineris [Fortezzo et al., 2016] shows that our identifications of mass-wasting zones agree. We additionally looked for locations where undeformed layered materials superposed the source zones of the landslides, indicating layered material deposition after moat formation [Anderson and Bell, 2010; Okubo, 2014; Neuffer and Schultz, 2006]. Results are given in Figures 13 and 14 and section 4.2.

3. Layer-Orientation Results

3.1. Overview

Among our measurements (308 layer dips extracted from 30 DTMs), most strata within VM and Gale’s mound were found to dip away from mound crests (Figure 6b). For layers above the mound base, the dip azimuth of 87% of the measured layers falls within 90° of the vector directly away from the nearest mound crest (mound centroid for Gale); 57% are aligned within 45°. This tendency is equally strong in Gale’s mound ($n = 126$) and VM ($n = 182$) (Figure 7d). The median dip of the measurements in our database (5°) corresponds (for an 80 km wide mound) to 3.5 km of relief on a stratigraphic surface. Indeed, canyons carved into Gale’s mound show easily observable relief of 500 m on individual layers.

Lowermost strata (≤ 0.5 km above the interpolated basal surface), which will soon be visited by the MSL rover, still dip preferentially away from mound crests (Figure 6c). This structural consistency with elevation contrasts with the mineralogical variability observed at Gale and elsewhere [Milliken et al., 2010]. Sulfate detections specifically correspond to outward dipping layers at Ganges Mensa, Melas Mensa, and Gale’s mound [Chojnacki and Hynes, 2008; Fueten et al., 2014] (Figure 8), as well as for Hebes and Candor Mensae [Schmidt, 2016; Jackson et al., 2011; Fueten et al., 2014]. Furthermore, draping layers in SW Melas Chasma show sulfate signatures [Weitz et al., 2015], suggesting that sulfate-bearing rocks on Mars can form at primary

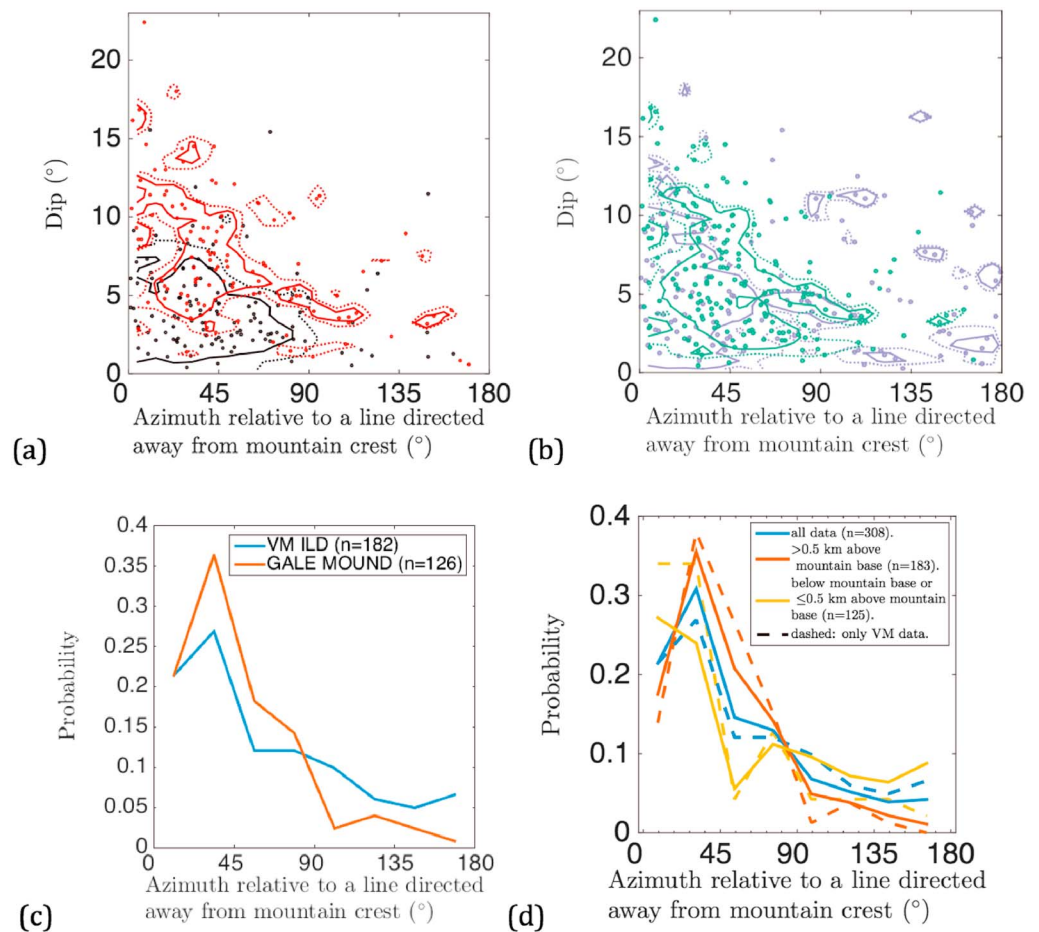


Figure 7. Layer-orientation details: (a) Data from Gale (black) compared to data from VM (red). Solid and dashed contours enclose 50% and 68% of measurements, respectively. (b) Layer orientations ≤ 0.5 km elevation above interpolated basal surface (purple) compared to layer orientations > 0.5 km above interpolated basal surface (green). Solid and dashed contours enclose 50% and 68% of measurements, respectively (compare Figure 6c). (c) Dip azimuth of all layers in Gale compared to dip azimuth of all layers in VM. (d) Distribution of layer orientations relative to elevation above interpolated basal surface of mound (22.5° bins).

depositional angles that are far from horizontal. Therefore, preferentially outward dips are not restricted to the spectrally bland, capping rhythmite facies identified in many sedimentary deposits on Mars, including the uppermost Gale strata [Grotzinger and Milliken, 2012; Lewis and Aharonson, 2014]. Although the rhythmite facies lies topographically above the northern rim of Gale crater, its induration still suggests cementation involving liquid water [Lewis et al., 2008]. Just as the mineralogical transitions up-section does not correspond to the end of surface liquid water on Mars, our measurements further suggest that they need not be accompanied by a change in the physical process of deposition.

Median dip > 2 km below mound summit is 4.7° ($n = 216$), less than median dip ≤ 2 km below mound summit (7.0° , $n = 92$). Similarly, layers > 1.5 km above the interpolated basal surface ($n = 99$) dip more steeply (median 7.5°) than layers ≤ 1.5 km above the interpolated basal surface ($n = 209$, median dip 4.5°). Gale data are shallow dipping and > 3 km below mound summit, and removal of Gale data (or removal of VM data) would remove the dip-versus-elevation correlation in our database.

The tendency for layers above mound base surface to dip away from the center of the mounds is insensitive to the error threshold (cutoff) beyond which data are discarded. Our nominal cutoff of 2° gives 87% of layers dipping away from the mound center. A cutoff of 1° gives 84% of layers dipping away from the mound center. Accepting all measurements, with no cutoff, yields $\sim 10\%$ more layer traces but no change in the percentage of layers that dip away from the mound center (87%).

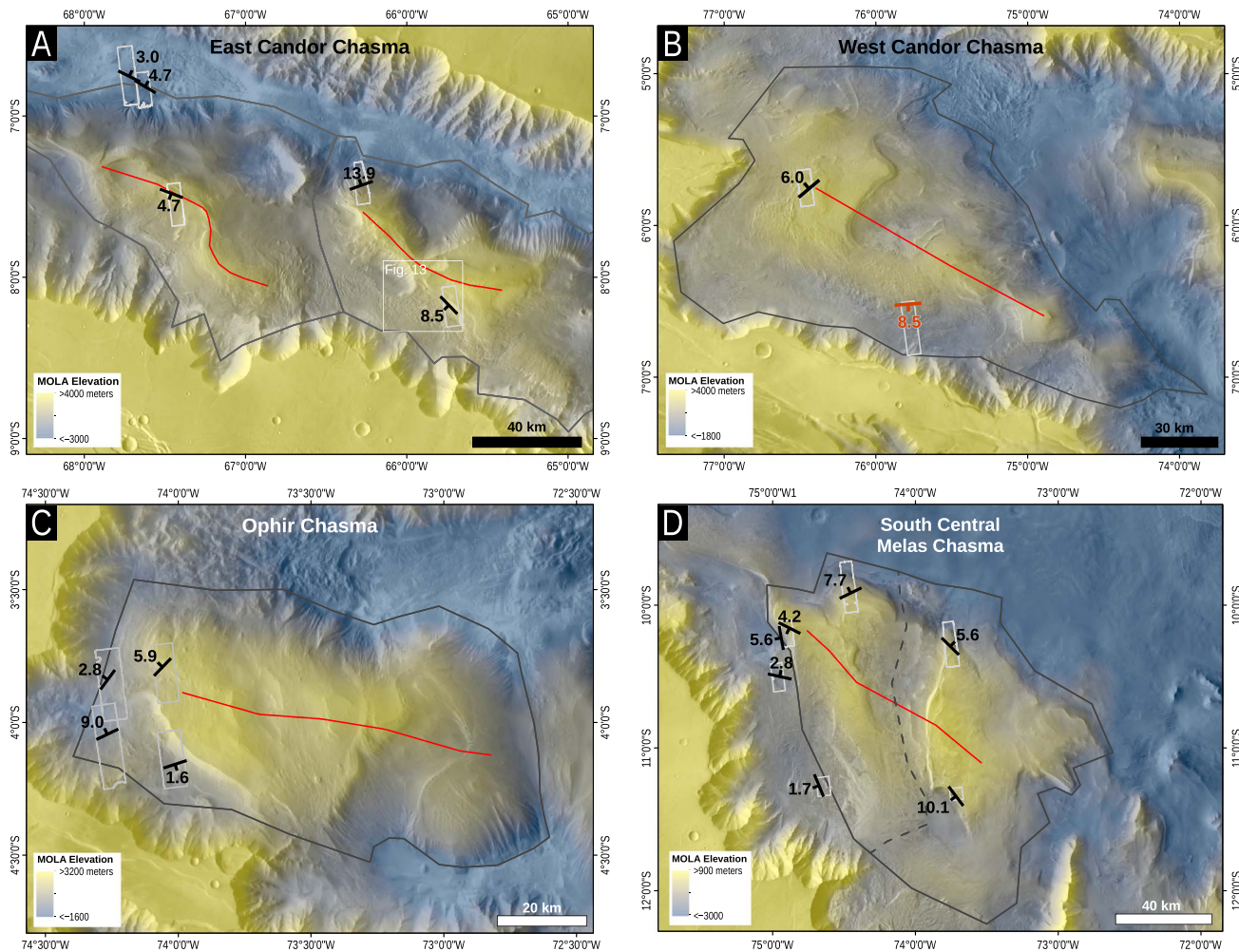


Figure 8. Mound-by-mound layer-dip data (dips in degrees). Color scale is clipped at high and low elevations in order to emphasize mound topography. Light gray shows the outlines of the HiRISE orthoimages/DTMs. Dark gray lines enclose the topographically defined mounds. Red lines show the mound crestlines. Strike-dip symbols and labels indicate average orientations of all layers traced on the corresponding orthoimage/DTM. (a) East Candor Chasma contains Nia Mensa (west) and Juventae Mensa (east). White rectangle shows the location of the draped landslide shown in Figure 13. (b) West Candor Chasma contains Ceti Mensa (drawn to include Nia Tholus). Crestline is drawn across a late-stage erosional window in central Ceti Mensa. See also *Fuente et al.* [2006], *S. Murchie et al.* [2009], and *S. L. Murchie et al.* [2009]. (c) Ophir Chasma contains Ophir Mensa. Crestline is drawn to cut across a late-stage erosional window in the east of the mound. See also *Wendt et al.* [2011]. (d) South central Melas Chasma contains Melas Mensa. Crestline is drawn to crosscut a topographic low that is interpreted as an erosional trough. An alternative scenario, in which Melas Mensa is in fact two mensae, is indicated by the dashed line. Data for the NWmost DTM show a clear break with elevation, so high-elevation data and low-elevation data are averaged separately. (e) Southeast Melas Chasma contains Coprates Mensa. Crestline is drawn to cut across some small troughs. (f) Ganges Mensa (data from *Hore* [2015]). For DTMs that straddle the mound centerline, we plot the average for data north of the centerline separately from the average for data south of the centerline. (g) Gale crater contains Mount Sharp/Aeolis Mons. Gray star shows the centroid of Gale's mound. Main canyon of Gale's mound is to the west. White rectangles show location of draped landslide and draped canyon in Figures 14a and 14b, respectively. Red data points are from *Kite et al.* [2013a]. (h) Showing Gale data in relation to Gale crater. Range rings (white dashed lines) show distance of candidate peak ring [*Allen et al.*, 2014] from Gale's central peak (red star).

The data indicate a strong preference for layers to be oriented away from mound centerlines.

3.2. Seven of the Eight Mounds Investigated Individually Exhibit the Outward Dips Predicted by *Kite et al.* [2013a]

Mound-by-mound analysis shows that seven of these eight mounds studied in this paper individually exhibit the outward dips predicted by *Kite et al.* [2013a]—Gale's mound, plus Ceti, Ophir, Melas, Ganges, Nia, and Juventae Mensae (Figure 8). For each mound, we visually inspected the intersections of layers in our CTX orthophotos with contour lines generated using our mound-spanning CTX DTM mosaics and confirmed that these structure contours are qualitatively consistent with the patterns described below using HiRISE data.

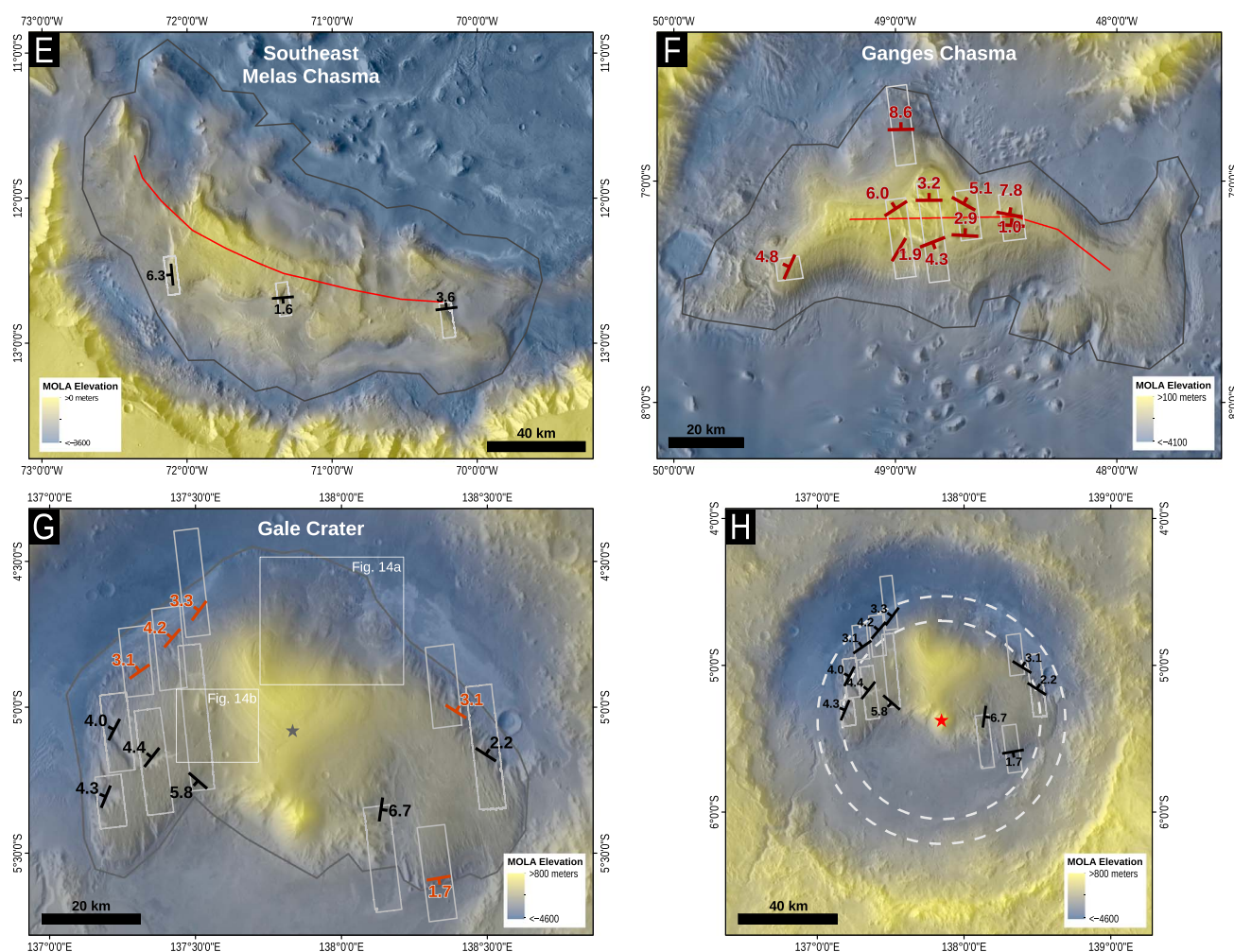


Figure 8. (continued)

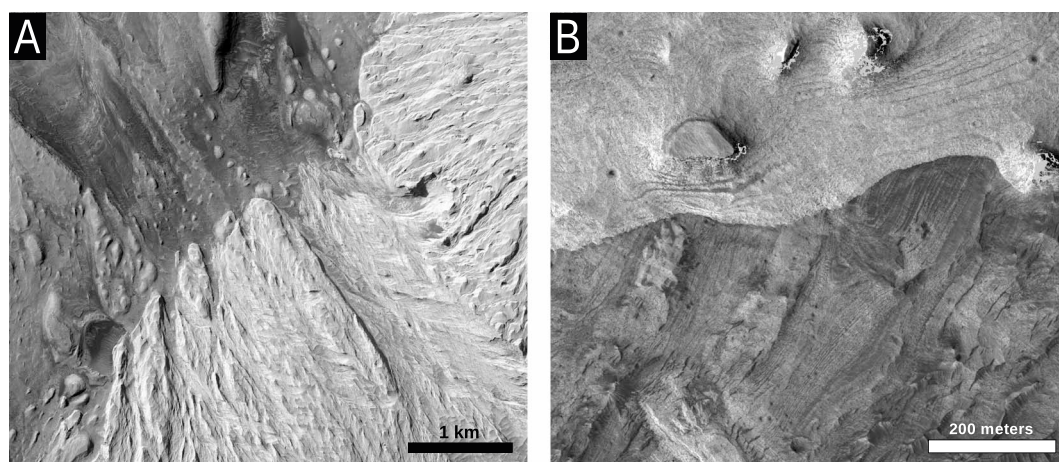


Figure 9. Examples of unconformities. (a) HiRISE snapshot of a mound-spanning unconformity in a within-crater mound (Gale's mound, near 4.83°S 137.41°E). Note embedded crater in bottom left. (b) HiRISE snapshot of a large unconformity in a within canyon mound (Ceti Mensa, near 5.80°S 76.47°W).

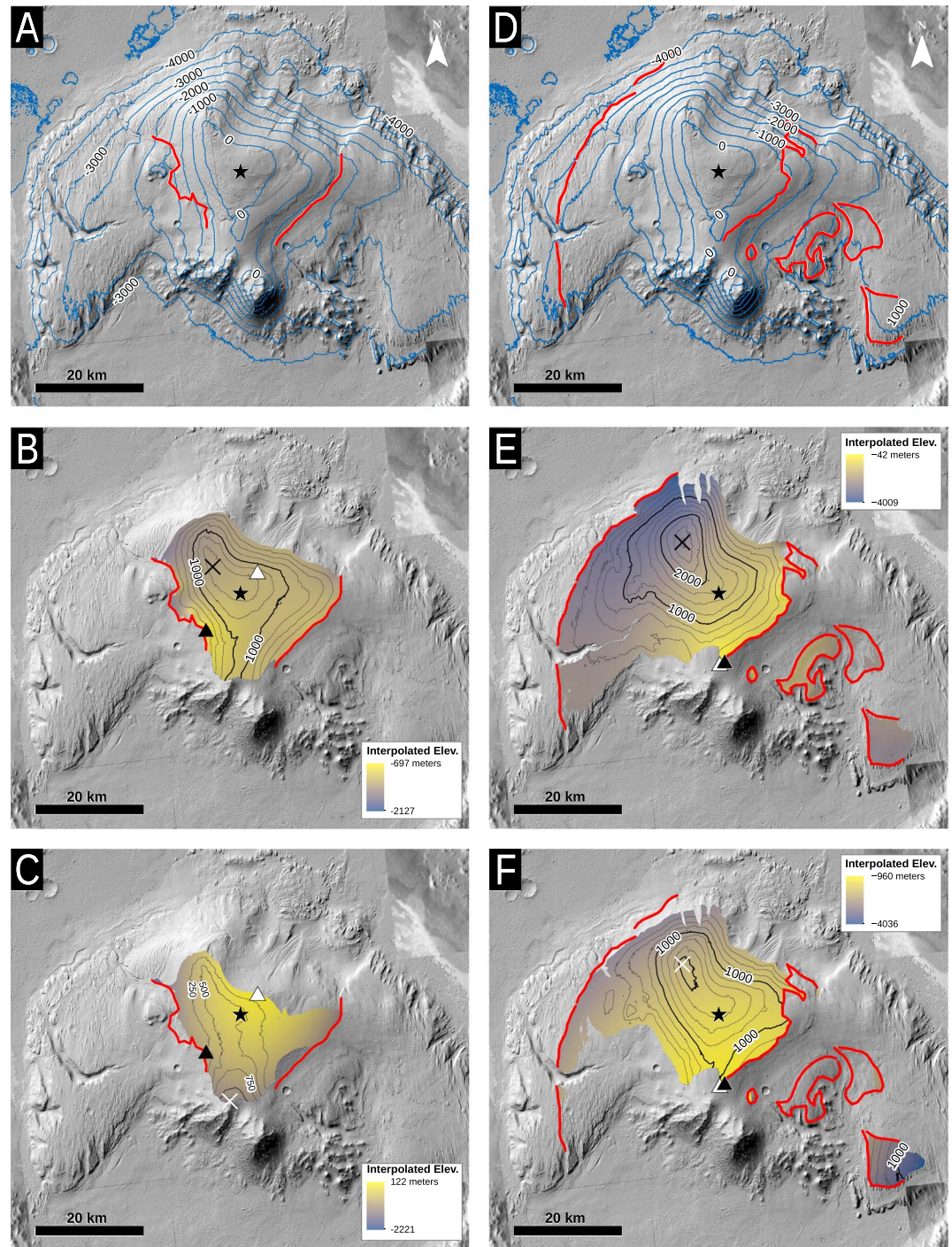


Figure 10. Paleodomes within Mars mounds. (a) Topography (blue contours) for Gale's mound (Gale is 155 km diameter). Red lines show the trace of stratigraphic surface interpreted as unconformity by *Anderson and Bell* [2010], which has >1 km of relief. Star = sedimentary-mound summit. (b and c) Colors show paleotopography of Gale's mound, interpolated using inverse-distance weighting (Figure 10b) and quadratic polynomial interpolation (Figure 10c). Black contours show isochores for late-deposited material. Filled and open triangles = high points of unconformity surfaces (filled for Inverse Distance Weighting (IDW) interpolated, open for quadratic interpolated). Cross = locations of maximum thickness for upper units. (d–f) Same as Figures 10a–10c but for stratigraphic surface interpreted as unconformity from *Thomson et al.* [2011]. Background is shaded relief of CTX DTM mosaic.

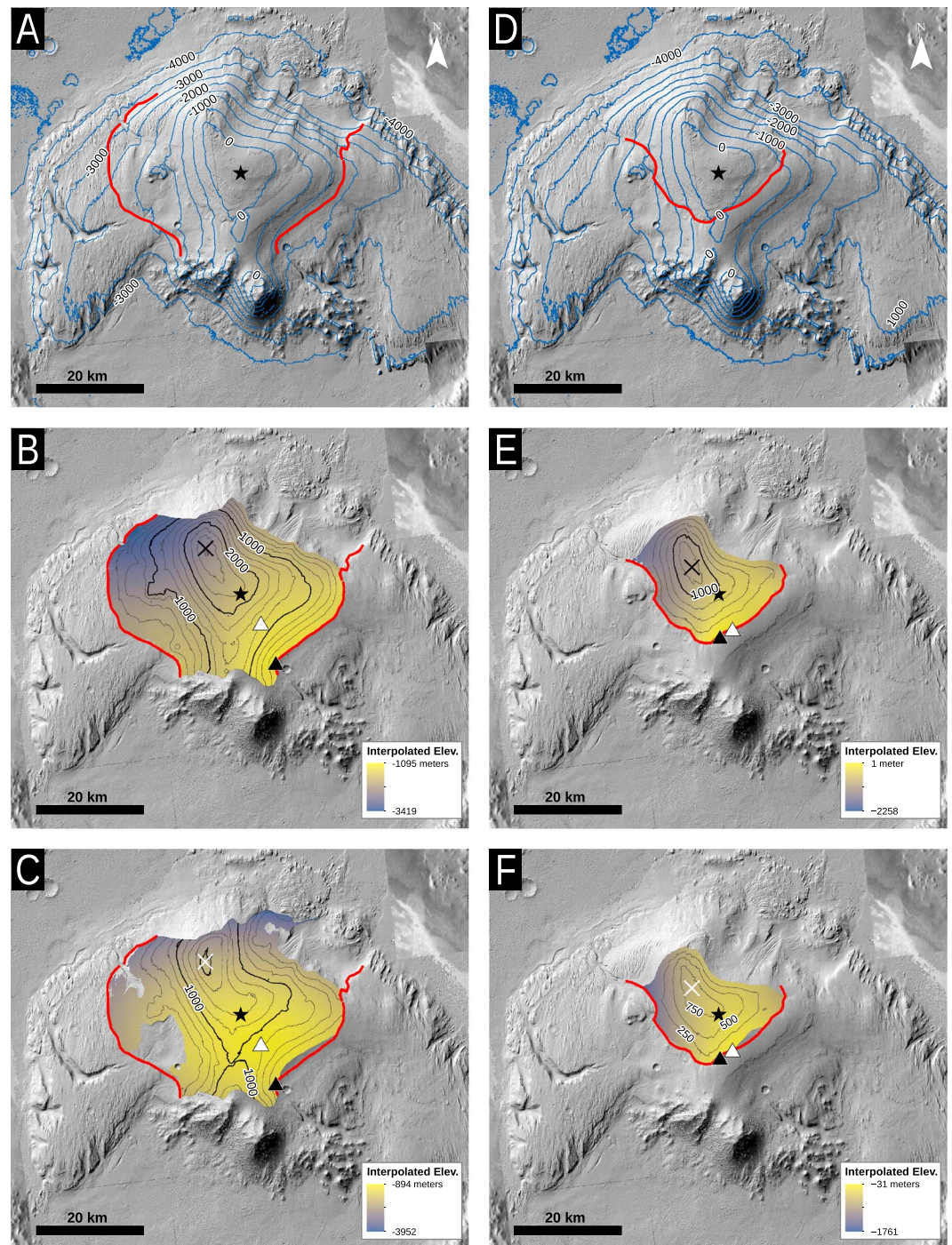


Figure 11. Paleodomes within Mars mounds. (a) Topography (blue contours) for Gale's mound (Gale is 155 km diameter). Red lines show the trace of the base Syu surface interpreted as unconformity by *Le Deit et al.* [2013], which has >1 km of relief. Star = sedimentary-mound summit. (b and c) Colors show paleotopography of Gale's mound, interpolated using inverse-distance weighting (Figure 11b) and quadratic polynomial interpolation (Figure 11c). Black contours show isochores for late-deposited material. Filled and open triangles = high points of unconformity surfaces (filled for IDW-interpolated, open for quadratic interpolated). Cross = locations of maximum thickness for upper units. (d–f) Same as Figures 11a–11c but for base Bu surface interpreted as unconformity from *Le Deit et al.* [2013] (this surface is best fit by a saddle: see Table 3).

Table 3. Table of Mound-Spanning Stratigraphic Surfaces Interpreted as Unconformities^a

Location	Mound	Stratigraphic Surface (Interpreted as Unconformity)	RMS Error on		Quadratic Fit	Quadratic Fit	Relief on Stratigraphic Surface (Interpreted as Unconformity)	Maximum Thickness Above Unconformity (IDW Interpolation) ^a	Maximum Thickness Above Unconformity (Quadratic Interpolation)
			Planar Fit	Quadratic Error	Fit	Fit			
West Candor	Ceti Mensa	Base caprock ^b [Lucchitta, 2015]	500 m	204 m		Saddle, high axis oriented 95° CW from north, saddle located near 76.3°W 5.8°S.	3.2 km	1.4 km	0.7 km
West Candor	Ceti Mensa	Base caprock [Lucchitta, 2015], high confidence region	301 m	77 m		Dome, ellipticity 1.4, centered at 76.35°W 5.87°S, long axis 6° CW from north	1.8 km	0.4 km	0.3 km
West Candor	Ceti Mensa	Base Rimrock ^b [Lucchitta, 2015]	475 m	168 m		Dome, ellipticity 3.2, centered 76.16°W 5.71°S, long axis 32° CCW from north	2.7 km	1.4 km	1.5 km
Gale	Mt. Sharp/Aeolis Mons	Base Bu [Le Deit et al., 2013]	154 m	86 m		Saddle, high axis oriented 13° CCW from north, saddle located near 137.8°E 4.7°S.	2.4 km	1.5 km	0.9 km
Gale	Mt. Sharp/Aeolis Mons	Base (Syu2 + Cyu) [Le Deit et al., 2013]	220 m	132 m		Dome, ellipticity 1.6, center 137.86°E 5.08°S, long axis 96° CW from north	3.3 km	2.7 km	2.1 km
Gale	Mt. Sharp/Aeolis Mons	Base "Upper mound (Um) formation" [Thomson et al., 2011]	826 m	426 m		Dome, ellipticity 1.3, center 137.80°E 5.25°S, long axis 41° CW from north	4.0 km	2.8 km	2.1 km
Gale	Mt. Sharp/Aeolis Mons	Base "Upper unit" [Anderson and Bell, 2010]	219 m	114 m		Dome, ellipticity 1.7, center 137.88°E 4.77°S, long axis oriented 13° CW from north	1.4 km	1.6 km	0.6 km.
Ophir ^c	Ophir Mensa ^c	"Marker horizon" [Wendt et al., 2011]/Peralta et al., 2015]	850 m ^c	339 m ^c		Dome, center 73.54°W 3.99°S, ellipticity 1.8, long axis 86° CW from north.	5.2 km ^c	1.2 kmv	1.1 km ^c

^aThe 1000 nearest-neighbouring points (i.e., vertices on unconformity trace), 1000 km search radius, cubic weighting.

^bThe "idu" of Fortezzo et al. [2016] corresponds to base rimrock in places and to base caprock in other places. However, fitting a quadratic surface to the Fortezzo et al. [2016] idu would also produce a dome.

^cDoubtful. The "marker horizon" trace follows the top of a cliff near 74°E 4°S, in an area without stratigraphic cues; all measurements associated with this trace are lower confidence.

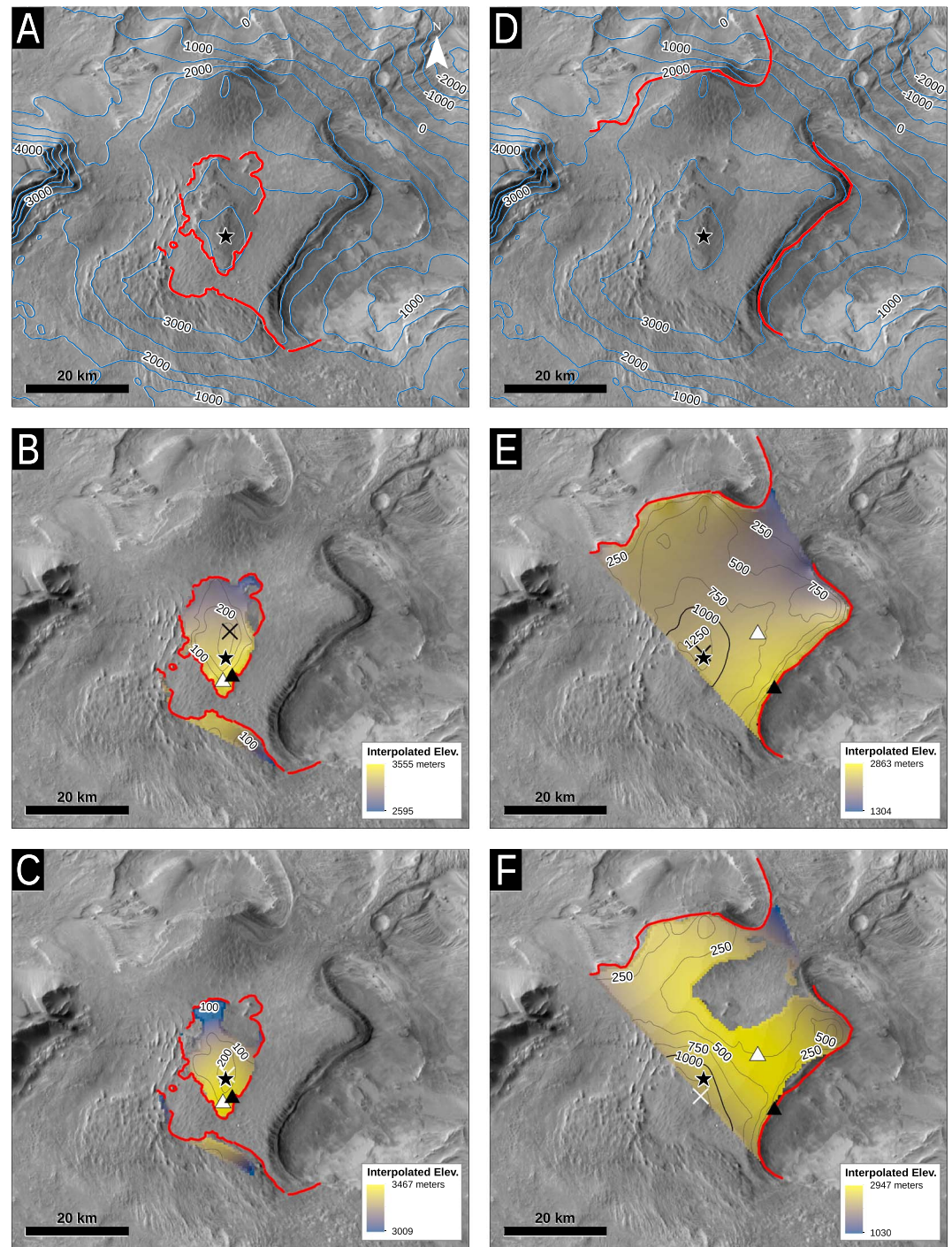


Figure 12. Paleodomes within Mars mounds. (a) Topography (blue contours) for Ceti Mensa (Candor Chasma is ~120 km wide). Red lines show the trace of base Caprock surface interpreted as unconformity by *Lucchitta* [2015], which has >1 km of relief. Star = sedimentary-mound summit. (b and c) Colors show paleotopography of Ceti Mensa, interpolated using inverse-distance weighting (Figure 12b) and quadratic polynomial interpolation (Figure 12c). Black contours show isochores for late-deposited material. Filled and open triangles = high points of unconformity surfaces (filled for IDW-interpolated, open for quadratic interpolated). Cross = locations of maximum thickness for upper units. (d–f) Same as Figures 12a–12c but for base Rimrock surface interpreted as unconformity by *Lucchitta* [2015]. Background is THEMIS VIS mosaic.

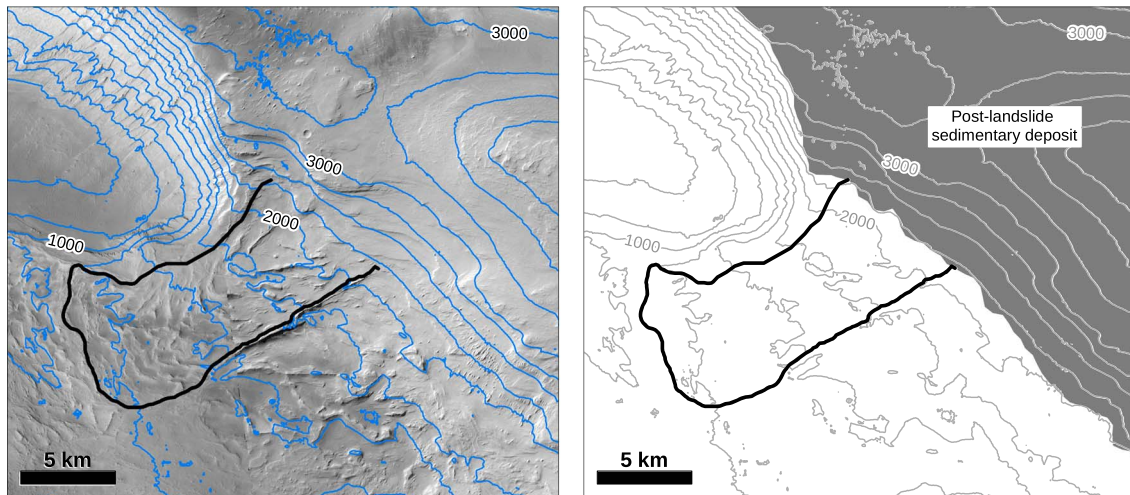


Figure 13. Draped landslides in East Candor. (left panel) Landslide on south side of Juventae Mensa (65.9°W 8.1°S). Range of elevations ~3 km. (right) Sketch interpretation (200 m topographic contours). Crosshatching denotes postslide sedimentary rock. All parts of figure use CTX DTMs. Location indicated in Figure 8a.

3.2.1. East Candor Chasma (Figure 8a)

East Candor contains the tallest sedimentary rock mounds on Mars: Juventae Mensa, and Nia Mensa. Five HiRISE DTMs were obtained, whose mean dips ($n=46$) systematically point away from the present-day mound crests (Figure 8a). One DTM (ESP_034896_1725/ESP_036542_1725) has only two traces within the 2° error threshold. Near the base of Nia Mensa, an arcuate feature has been interpreted as a delta [Le Deit *et al.*, 2008]: in our layer-trace database, this feature shows northward dips that lack the fanning-out dip-directions expected of a delta. Nia Mensa and Juventae Mensa are dusty, and we are not aware of published sulfate detections there [Roach, 2009].

3.2.2. West Candor Chasma (Figure 8b)

Measured dips within Ceti Mensa are outward. Our Ceti Mensa observations support Okubo's [Okubo *et al.*, 2008; Okubo, 2010, 2014] interpretation of a paleomoat. The red point in Figure 8b was calculated by taking the average of the 210 dips reported by Okubo [2014] from the northernmost (highest in elevation) outcrop of the CeM_k unit as defined in Okubo [2014]. Sulfate minerals are found at levels stratigraphically equivalent to many of the outward dips [Gendrin *et al.*, 2005; Mangold *et al.*, 2008; S. L. Murchie *et al.*, 2009; S. L. Murchie *et al.*, 2009]. Our one additional DTM west of the mound centerline has three good traces, showing generally west directed dips.

3.2.3. Ophir Chasma (Figure 8c)

Four HiRISE DTMs ($n=48$), all from the western end of the Ophir Mensa mound, show dips that are directed away from the mound crest except for the lowest elevation DTM, which shows dip directions that parallel the mound crest. The DTM marked "2.8°" shows layers that drape the lowest part of the canyon wall in the west of the DTM and layers that dip steeply toward the canyon wall in the E of the DTM. Dust on Ophir Mensa complicates spectroscopy. We know of one kieserite detection on Ophir Mensa at the level of our measurements [Gendrin *et al.*, 2005; Chojnacki and Hynek, 2008].

3.2.4. South Central Melas Chasma (Figure 8d)

SC Melas Chasma hosts Melas Mensa, an ~3 km high mound with 6 HiRISE DTMs ($n=60$). Layers dip away from the mound centerline around the mound. Sulfate minerals are found at levels stratigraphically equivalent to many of the outward dips [Gendrin *et al.*, 2005; Chojnacki and Hynek, 2008]. However, DTMs of sedimentary rock layers at the base of the mound show more variable layer orientations, including some layers dipping back toward the mound. Melas Mensa has a N-S aligned medial trough. If this trough is used to divide the mound into two mounds, then traces from two elevation maps are most strongly affected (ESP_012361_1685_ESP_012572_1685 and PSP_005953_1695_PSP_002630_1695), totaling 21 traced layers. Under likely measures of two central ridge features for each mound considered separately, 9 of these traces would be oriented more directly away from central ridges, and 13 would be oriented less

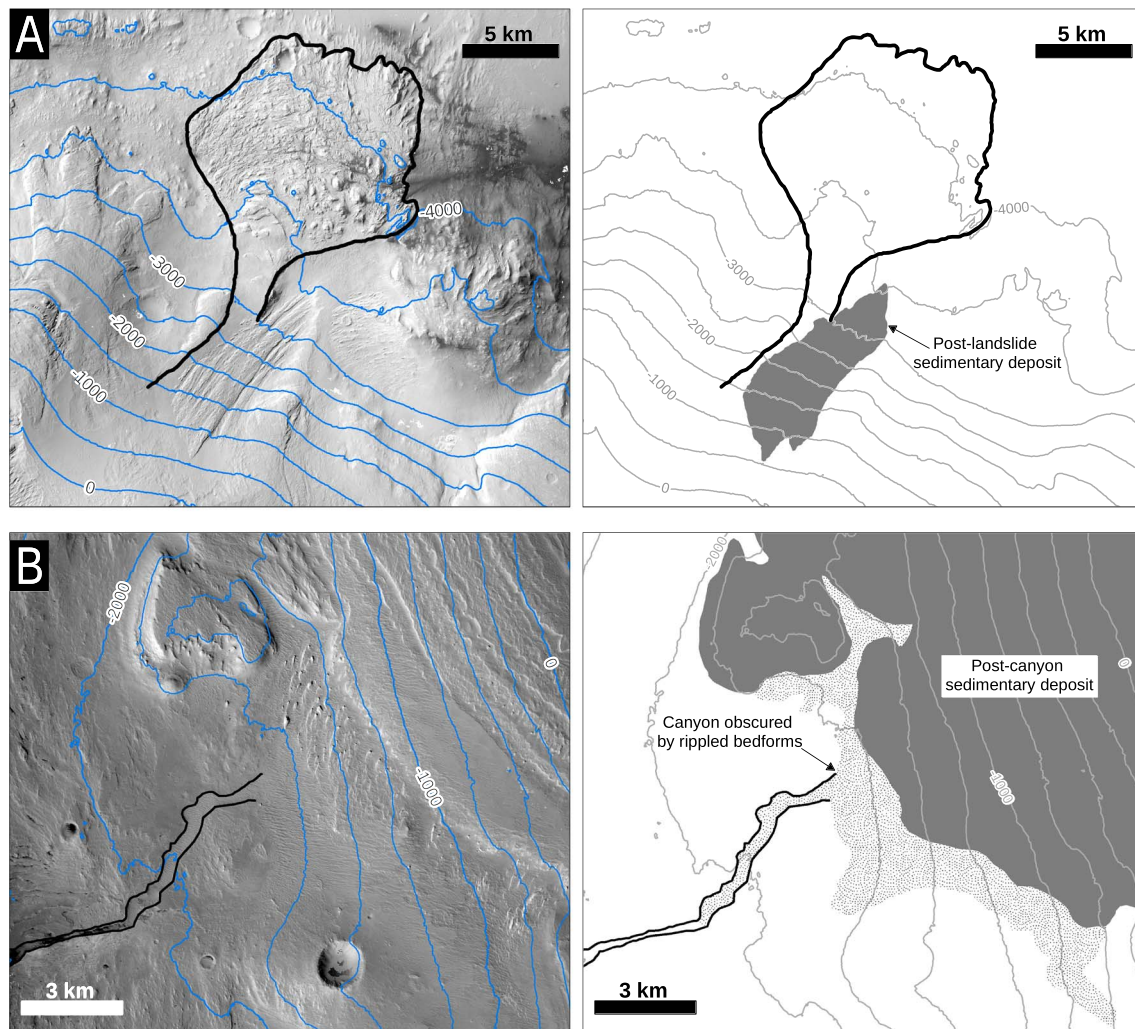


Figure 14. Draped landslides and draped canyons in Gale. (a, left) Landslide on north side of Gale's mound (137.9°E 4.8°S). Range of elevations ~4 km. (right) Sketch interpretation (200 m topographic contours). (b, left) Draped landslide on west side of Gale's mound (137.5°E 5.1°S). Range of elevations ~2 km. (right) Sketch interpretation (200 m topographic contours). Diamonds denote postcanyon sedimentary rock. Stippling denotes mobile cover. All parts of figure use CTX DTMs. Locations indicated in Figure 8f.

directly. Therefore, our conclusion is not affected by whether Melas Mensa is considered as 1 or 2 mountains.

3.2.5. Southeast Melas Chasma (Figure 8e)

SE Melas Chasma hosts Coprates Mensa, a relatively low (~2 km) mound with layer orientations that do not match those predicted by Kite *et al.* [2013a]. Two of our three DTMs ($n = 23$) show layer orientations that are variable, but average out to dips that are parallel to the mound crest; the remaining DTM shows dips that slope back toward the mound crest. Sulfates exist at the level of some of our measurements in the east of Coprates Mensa [Gendrin *et al.*, 2005; Chojnacki and Hynek, 2008].

3.2.6. Ganges Chasma (Figure 8f)

A comprehensive (six DTMs) study of Ganges Mensa [Hore, 2015] shows systematic outward dips (Figure 8f). Hore [2015] does not provide error bars, so we do not include Ganges data in Figures 6 and 7. Sulfates are common in Ganges Mensa [Chojnacki and Hynek, 2008], including at the stratigraphic level of our measurements.

3.2.7. Gale Crater (Figures 8g and 8h)

Our database for Gale's mound, Mount Sharp/Aeolis Mons ($n = 126$) includes new measurements for six DTMs. We combine these with layer orientations from five DTMs presented in Kite *et al.* [2013a]. Layers dip systematically away from the mound center, including up the main canyon of Mount Sharp/Aeolis Mons

and close to the center of the mound. However, we did not find many traceable layers in HiRISE stereopairs close to the center of the mound, and the two DTMs closest to the center of the mound each have only three traces within the 2° error threshold. The observed persistence of outward layer dips up the main canyon of Gale's mound rules out the hypothesis that a peak ring is solely responsible for the layer orientations. Arcuate mounds between 40 km and 50 km from Gale's central peak may be eroded remnants of a peak ring [Allen *et al.*, 2014]. If this central ring persists underneath Gale's mound, then it might affect layer orientations locally. We did not find clear evidence for a peak ring effect on layer orientations; it is possible that further analysis of HiRISE DTMs might turn up such evidence. Whether or not a "peak ring effect" is detectable in the orientation of some the layers of Mount Sharp/Aeolis Mons, the outward layer dips we observe occur at a wide range of distances from Gale's central peak—too wide a range for a peak ring to explain the outward dips. Because Gale's central peak is volumetrically negligible compared to the volume of Mount Sharp's lower unit and is visibly intact, erosion of Gale's central peak cannot account for the deposits contained within Aeolis Mons/Mount Sharp's lower unit.

Hebes Mensa (not shown) shows systematic outward dips, and sulfate detections, but a flat unconformity [Jackson *et al.*, 2011; Schmidt *et al.*, 2015; Schmidt, 2016].

4. Stratigraphic Unconformities and Draped Landslides

4.1. Stratigraphic Unconformities

We analyzed the major unconformities reported at Gale and West Candor [Anderson and Bell, 2010; Lucchitta, 2015; Thomson *et al.*, 2011; Le Deit *et al.*, 2013] (Figures 9–12). In every case (Table 3), present-day exposures of these surfaces show large (1–4 km) relief [Malin and Edgett, 2000; Fueten *et al.*, 2014]. Using procedures described in section 2.3, we identify and interpolate these stratigraphic horizons across each deposit. The interpolated unconformity surfaces dip steeply [Thomson *et al.*, 2011], analogous to the modern mound forms, and consistent with past wind erosion [Heermance *et al.*, 2013]. Interpolated surfaces typically define paleodomes within the interior of each mound (Table 3). Paleodome summits are usually close to modern topographic highs (Figure 9). Furthermore, isochores show preferential deposition near paleodome summits (Figures 9–12). These paleodomes, defined by unconformable surfaces deep within the stratigraphy, strongly suggest the existence of moats during the interval of deposition (i.e., net anticompensational stacking).

Our data suggest that the mound-spanning unconformities truncate underlying layers, usually dip toward the canyon edge or crater rim, and are draped by parallel layers [Anderson and Bell, 2010; Holt *et al.*, 2010; Okubo, 2014]. Draping implies that post-unconformity sediments were wind transported (similar to Holt *et al.* [2010]). Water-transported sediments would onlap the paleodome. We looked for, but did not find, evidence for onlap. We are not aware of basin-scale unconformities of this type on Earth.

4.2. Draped Landslides

Gravity-slide deposits, when interstratified with sedimentary rocks, point away from paleohighs on unconformity surfaces [Sharp, 1940]. Landslides encircling Ceti, Coprates, and Juventae Mensae, Gale's mound, and possibly Melas Mensa, flowed away from mound crests and are overlain by sedimentary rocks, especially at locally high elevations [Lucchitta, 1990; Neuffer and Schultz, 2006; Okubo, 2014] (Figures 13 and 14). (A moatward draining canyon at Gale's mound is also draped by sedimentary rocks; Figure 12). Therefore, sedimentary rock emplacement on topographic highs continued after moats were defined. Therefore, draped landslides are diagnostic for paleomoats. Draped landslides exclude a scenario in which paleodomes result from rapid differential compaction of initially horizontal layers, because that scenario does not permit dome-shaped syndepositional paleotopography. To the contrary, draped landslides suggest that the paleodome unconformities had an erosional origin.

5. Assessment of Mound Emplacement Hypotheses, Emphasizing Valles Marineris

The VM mound-emplacement hypotheses that are most frequently discussed are the compensational stacking (playa/lake or fluviodeltaic infill) and anticompensational stacking (e.g., slope winds) models (section 1).

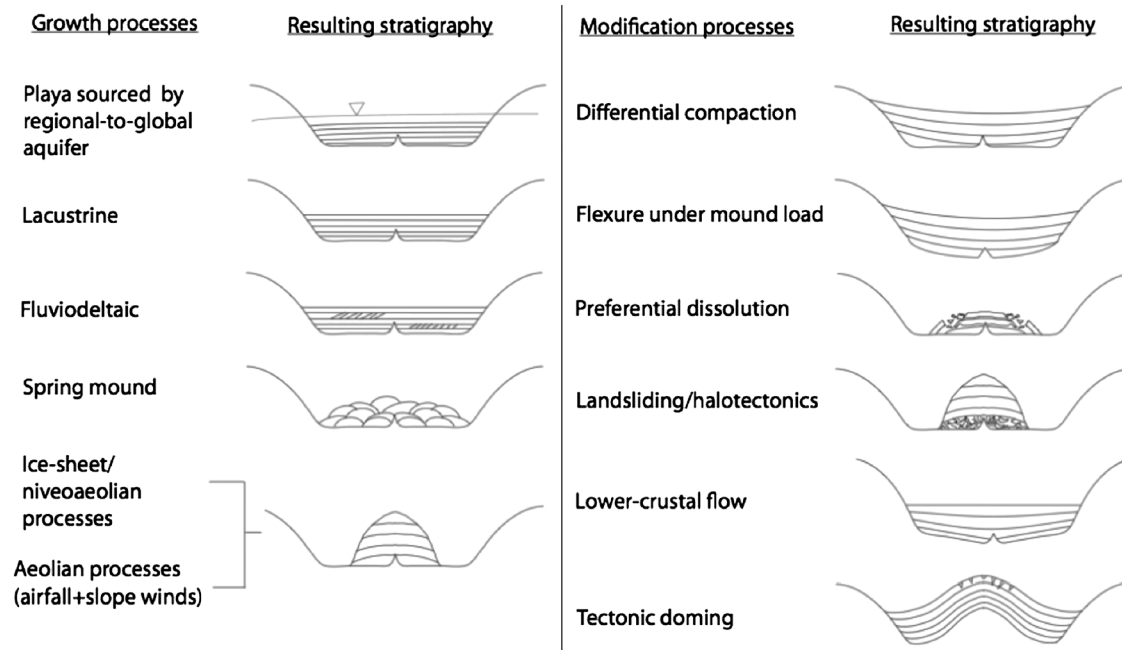


Figure 15. (Modified from Kite *et al.* [2013a]). Comparison of the layer orientations predicted by different mound growth hypotheses, for an idealized cross section of a mound-bearing crater. Inverted triangle marks past water table.

Other VM ILD formation models [Nedell *et al.*, 1987; Lucchitta *et al.*, 1992] include nunutaks [Gourronc *et al.*, 2014], tuyas [Chapman and Tanaka, 2001], spring mounds [Rossi *et al.*, 2008], salt-sheet outliers [Montgomery *et al.*, 2009], salt tectonics [Jackson *et al.*, 1991, 2011; Baioni, 2013], and carbonate deposits [McKay and Nedell, 1988] (Figure 15). The tuya and carbonate mound hypotheses fail to match post-2004 spectroscopic data. We cannot logically exclude a scenario in which the VM mounds are volcanoclastic/ash/pyroclastic deposits emplaced on the flanks of a dyke or a central volcano. However, this possibility is disfavored by (i) the tendency of fissure eruptions to evolve to pipe eruptions geologically quickly [Wylie *et al.*, 1999], in contrast with the elongated shapes of the VM mounds, and (ii) the regular layering of the rhythmite, suggesting quasiperiodic deposition as opposed to the power-law behavior exhibited by volcanic eruptions [Lewis *et al.*, 2008; Pyle, 1998]. The salt-sheet outliers hypothesis invokes a laterally continuous salt layer (extending under the plateaus encircling VM). This hypothesized layer is hard to reconcile with VM wall rock observations that do not show salt layers or that show salt layers which drape onto wall rock. The nunutaks hypothesis invokes wet-based glaciers for which there is little uncontested evidence. The spring mounds hypothesis has difficulty explaining the great lateral continuity of observed layers.

We cannot exclude the possibility that the VM mounds are giant salt domes. However, salt movement [Jackson *et al.*, 1991, 2011] after moat formation would be sideways, not upward (as a salt glacier). Salt diapirism before moat erosion would not lead to systematic outward dips in outcrop. Where diapirism is inferred on Mars, it has a horizontal length scale that is comparable to the thickness of the sedimentary layer and is so much less than the $\sim 10^2$ km length of the VM mounds [Bernhardt *et al.*, 2016]. Faulting can and does tilt layers [Lewis and Aharonson, 2014], but syndepositional basement uplifts beneath (and only beneath) mounds are unlikely. In particular, we disagree with the syndepositional-tilting proposal of Fueten *et al.* [2008] because the upper materials—the “caprock” and “rimrock” of Lucchitta [2015]—lack obvious major faults. Predepositional tectonic uplifts might nucleate draping deposition, but draping deposition on highs is an example of anticompensational stacking, not an alternative. Landslides are common, but are easy to identify, and are excluded from our layer orientation measurements (Figure 11).

Differential compaction of sedimentary layers over basement relief has been proposed to reconcile deposition of flat-lying strata with observed layer orientations [Grotzinger *et al.*, 2015]. This is inconsistent with VM data. In VM, the basement surfaces of canyon floors that are not covered by thick sedimentary deposits are observed to be flat (e.g., East Coprates Chasma, Ganges Chasma, and Noctis Labyrinthis). The implication

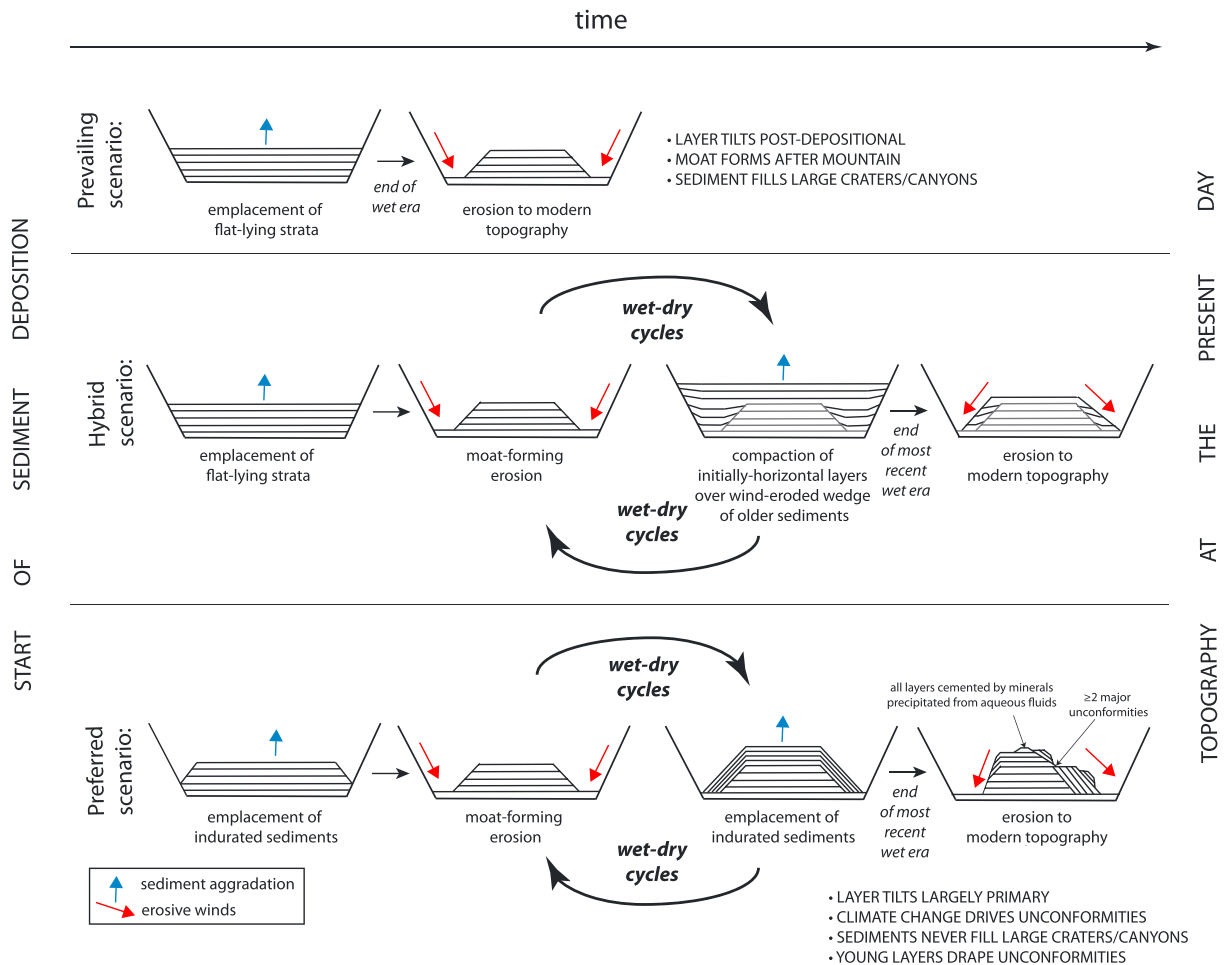


Figure 16. Cartoon cross-sections of craters/canyons and evolving mounds, summarizing “prevailing view,” “hybrid scenario,” and “preferred view” of mound formation.

that the central Valles Marineris canyons formed via near-vertical tectonic subsidence is strongly supported by independent tectonics data and modeling [Andrews-Hanna, 2012b]. If the basement of the VM canyon floors is flat before sedimentary loading, flexural adjustment to the loading the basement will dip inward. This inward dip should set the sign of differential compaction tilts for initially flat-lying strata with uniform grain size. If grain size is not uniform, then differential compaction can tilt layers away from coarse-grained deposits. However, fluviolacustrine processes will preferentially deposit coarse grains near the margins of the canyon, again leading to inward dips. Therefore, if differential compaction caused layer dips in VM, we should not see outward dips on both sides of a mound. However, we do observe outward dips on both sides of mounds (Figures 6 and 8), contradicting the hypothesis of differential compaction for layer orientations in VM mounds.

A hybrid hypothesis could reconcile VM layer orientations with initially horizontal deposition. In this hypothesis, early-deposited sediments were first precompacted by thick overburden and then eroded into wedge-shaped outliers. A later generation of sediments was differentially compacted over these wedge-shaped outliers, leading to the observed outward dipping layers (Figure 16). This hypothesis is a hybrid because terrain-influenced winds are required to erode the precompacted sediments into a correctly shaped wedge prior to further sediment deposition. Even if a buried wedge of ancient sediments exists and was precompacted sufficiently to act as a rigid floor for later differential compaction, compaction is at best marginally sufficient to explain the large amplitude of observed dips [Gabasova and Kite, 2016]. Furthermore, if hypothetical wedge-shaped remnant deposits exist, then they exist mainly in subcrop, because inspection of HiRISE images does not show the large-scale within-mound onlap predicted by this scenario.

Other mechanisms that rotate layers outward during mound construction are quantitatively insufficient to explain the data, require fine tuning, or both. For example, flexural tilting due to late-stage volcanism is $<0.1^\circ$ [Isherwood *et al.*, 2013]; outward tilting by the flexural response to erosional unroofing is $<0.2^\circ$ [Davis, 2007] and can only partly recover inward tilting during sedimentary rock loading; and post-Noachian crustal flow is minor [Karimi *et al.*, 2016].

These considerations favor the interpretation that the dip directions are primary, i.e., that the mounds grew as mounds and that present-day mound crests are close to the crests of the growing mounds [Anderson and Bell, 2010] (Figures 2 and 3). In combination with the paleodome and draped-landslide evidence, the layer dips suggest anticompensational stacking.

One mechanism that predicts anticompensational stacking is slope-wind intensification of erosion on steep topographic slopes [Kite *et al.*, 2013a; Day and Kocurek, 2016]. In this model, terrain-induced winds inhibit sedimentary rock emplacement on crater/canyon walls, creating paleomoats. These paleomoats serve as the basal surface for subsequent deposition. Slope-wind controlled sedimentary-basin buildup combines processes that individually have a well-understood terrestrial analog but which rarely occur in combination on Earth. For example, katabatic winds drain the Antarctic plateau [Parish and Bromwich, 1991], deep incision into rock by wind erosion has been reported from the Atacama [Perkins *et al.*, 2015], and the Qaidam basin is being exhumed by wind erosion [Heermance *et al.*, 2013].

Slope-wind dynamics are not the only means of producing anticompensational-stacking kinematics: snow destabilization by föhn winds [Brothers *et al.*, 2013], reduced saltation transport to higher elevations due to lower pressure, and greater availability of abrasive sand at lower elevations, could all cause preferential net erosion of sediments at lower elevations—and thus favor anticompensational stacking. Sediment can be delivered by suspension transport (“airfall”) and also by saltation transport. Saltation transport to paleohighs need not be prevented by moats; sand dunes flow uphill in modern VM and on polar mounds [Chojnacki *et al.*, 2010; Conway *et al.*, 2012] (another example is visible in ESP_029504_1745).

These slope-dependent models have the common advantage that they all predict that outward directed dips should be ubiquitous, provided that craters/canyons have long, steep walls [Kite *et al.*, 2013a, Figure DR2]. This matches our observations—outward dips are very common (section 3).

6. Model: Anticompensational Stacking and Climate Change

Anticompensational stacking implies that layers steepen over time. Steepening could occur via layer truncation at unconformities, mound-scale layer pinch out, or both. We did not find evidence for mound-scale layer pinch out. Instead, we found layer truncation at a small number of large unconformities. We interpret these unconformities as paleomoat bounding surfaces (Figures 8 and 9 and Table 3) [Okubo, 2014]. We infer that anticompensational stacking arises from long depositional intervals separated by major erosive intervals (Figure 16)—a drape-and-scrape cycle.

Wind erosion can form paleomoats. Wind-induced saltation-abrasion is widely accepted to erode mound material in the present epoch [Grotzinger, 2014], to have formed present-day moats [Kite *et al.*, 2013a; Day and Kocurek, 2016] and to have had greater erosive power in Mars' past. To parameterize moat and paleomoat formation, we used Mars Regional Atmospheric Modeling System (MRAMS) simulations [Rafkin *et al.*, 2001], a realistic day-night cycle, and idealized mound-and-moat topography (Appendix B). MRAMS results indicate that slope effects are crucial to moat formation at low atmospheric pressure, with wind stresses ~ 5 times greater on steep slopes relative to flat floors within-craters/canyons (Figure B3). Higher wind stresses are likely correlated with faster long-term wind erosion, because wind stress is observed to exert strong control on aeolian sediment transport rates, including on Mars [Ayoub *et al.*, 2014; Martin and Kok, 2016], and because aeolian sediment transport is required to provide abrasive particles for sandblasting and/or to remove debris.

Mars' obliquity (ϕ) varies quasiperiodically at 10^5 yr timescales, but chaotically at longer timescales, ranging from 0° to 70° [Laskar *et al.*, 2004], with significant effects on climate. At low ϕ , models indicate that water is less available at the low latitude of VM and Gale [e.g., Jakosky and Carr, 1985; Mischna *et al.*, 2003; Madeleine *et al.*, 2009; Andrews-Hanna and Lewis, 2011; Mischna *et al.*, 2013; Wordsworth *et al.*, 2013; Kite *et al.*, 2013b; Fastook *et al.*, 2008]. Without water for cementation, sediment does not get preserved in the

sedimentary rock record. Sedimentary rock formation is also disfavored by surface condensation of atmospheric CO₂ at low ϕ [Forget *et al.*, 2013; Soto *et al.*, 2015]; atmospheric collapse suppresses aeolian-sediment supply and surface liquid water. At high ϕ , by contrast, water is progressively driven to lower latitudes as polar regions receive greater insolation [e.g., Mischna *et al.*, 2013]. Additionally, sediment deposition rates may be enhanced by globe-spanning storms expected at high ϕ [Haberle *et al.*, 2003; Armstrong and Leovy, 2005; Newman *et al.*, 2005]. These considerations suggest an important role for ϕ in modulating sedimentary rock buildup [Lewis *et al.*, 2008]. In the words of Metz *et al.* [2009], “Obliquity-driven climate [...] may be a more significant factor in the development of the stratigraphic record of Mars as compared to Earth.”

To model mound buildup including chaotic ϕ forcing and paleomoat formation, we carried out >100 simulations of Mars ϕ history. Each simulation combines 3 Gyr long eight-planet MERCURY6 [Chambers, 1999] simulations and an obliquity model [Armstrong *et al.*, 2004, 2014] (Appendix A.3). For each simulation, we assume sedimentary rock accumulation (assumed, for simplicity, to occur at a spatially uniform rate) competes with terrain-influenced erosion at VM and Gale when Mars’ obliquity (ϕ) > 40°, but that erosion alone operates when ϕ < 40°. The critical obliquity value is somewhat arbitrary, although all low-atmospheric-pressure models predict a nonlinear increase in the abundance of surface water ice at the latitude of VM and Gale at ϕ > (40⁺⁵_{−8})°. We do not model the between-basin variation in availability of liquid water needed for cementation; previous work shows [Andrews-Hanna and Lewis, 2011; Kite *et al.*, 2013b] that between-basin variability can match the scenario presented here. We also do not model the <10⁵ year timescale cycles that are responsible for the development of the layers whose orientation we measure, because these cycles occur at much shorter timescales than the overall mound construction modeled here [Lewis and Aharonson, 2014]. Possible causes of layering are discussed in, e.g., Kite *et al.* [2013b] and Andrews-Hanna and Lewis [2011]. These simplifications ensure that the details of the model do not obscure the processes modeled by SOURD (slope-wind control of within basin spatial variations, and nonlinear obliquity control of mound-spanning unconformities variations). To combine obliquity forcing and wind-terrain feedback, we use a 2-D (horizontal-vertical) landscape evolution model. The horizontal dimension corresponds to a cross section from the mound summit to the container edge. Gale’s central peak is not included because it is offset (by 0.3 crater radii) from the mound summit (Figures 10 and 11). Sediment is supplied from distant sources, and eroded material is removed to distant sinks. Consistent with CTX-scale morphology, thermal inertia, and the paucity of craters on sedimentary mounds [Malin *et al.*, 2007], we assume that sedimentary rocks are much more erodible than igneous “basement.” We adjust accumulation rate so that modeled mounds are ~3 km tall. The model produces mounds of the correct height with a mound-sediment deposition rate $D \approx 25 \mu\text{m/yr}$, a rate that is independently suggested by the thicknesses of orbitally paced layers [Lewis and Aharonson, 2014]. Model maximum deposition rates are similar to maximum erosion rates. Higher wind-erosion rates 3 Ga are consistent with ~10² nm/yr modern-era wind-erosion rates [Grindrod and Warner, 2014; Farley *et al.*, 2014; Kite and Mayer, 2016] if the supply of abrading particles is not limiting, wet-era atmospheric pressure was ~60 mbar [Catling, 2009; Brain and Jakosky, 1998], and sandblasting rate increases faster than linearly with atmospheric pressure.

Model output (Figures 17 and 18) shows that aeolian sedimentary rock emplacement forced by chaotic ϕ change, and including the wind-terrain feedback effect, can produce free-standing mounds within a crater/canyon [Kite *et al.*, 2013a]. The basic implications of obliquity forcing for slope winds are illustrated in Figure 17. At mound scale, the layers documented in Figures 6–8 would closely parallel the colored lines shown in our model output figures. Figure 17a uses square-wave deposition forcing, and Figure 17b uses an example realistic forcing. In reality, obliquity is chaotic; many simulations are needed to bracket the range of possible behavior (e.g., Figure 18). As expected, the dominant behavior is anticompensational stacking.

A key attribute of modeled sedimentary deposits (Figures 17 and 18) is that both layers and internal unconformities dip away from mound crests, consistent with data (Figure 6–8). Though the mound topography and pattern of outward dip directions observed within Mars’ sedimentary rock mounds are the most prominent features explained by this mechanism, the predicted stratigraphy simultaneously matches a range of observed physical attributes. These include the average dip magnitudes (which cluster at the mound height:width ratio), the thinning upward of unconformity-bounded stratigraphic packages [Malin and Edgett, 2000], the layer thicknesses, and the outward dip of unconformities (Figures 2 and 3) [Banham *et al.*, 2016]. The results explain why layer orientations frequently conform to modern topographic slope [Fueter *et al.*, 2008]. Because deposition occurs by progressive draping on preexisting mound topography, only

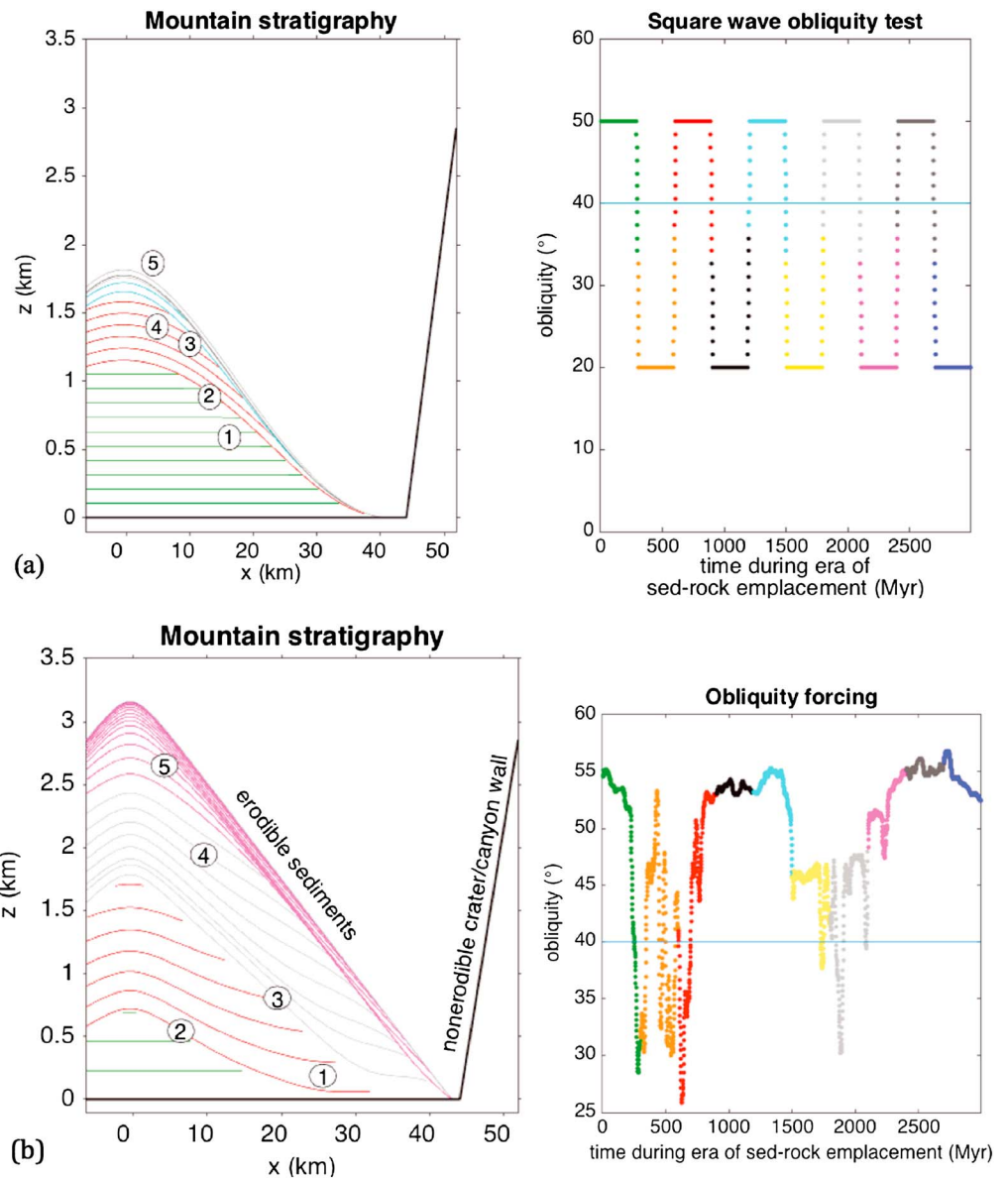


Figure 17. Model of how Mars mound stratigraphy might encode chaotic climate change. (a) Square-wave demonstration of how obliquity forcing and slope winds combine to explain the basin-scale stratigraphy of the largest sedimentary rock mounds on Mars. (right) Alternations every 300 Ma between high mean obliquity (deposition) and low mean obliquity (no deposition, erosion only). Critical obliquity shown by horizontal blue line. (left) Sedimentary stratigraphy shown by colored lines (cross section of mound). Black line is nonerodible container. Lines are drawn at 20 Myr intervals. Colors change every 300 Myr. The numbered properties of the model output are consistent with the data. 1 First-deposited stratigraphic package has layers that gently dip away from the mound center (Figure 6c). 2 Unconformities slope away from mound center, defining paleodomes (Figures 9 and 10). 3 Unconformities steepen up-mound. 4 Dips of late-deposited sediments conform to modern topographic slope. 5 Unconformity-bounded stratigraphic packages thin moving up-mound (Table 3). (b, right) One possible history of orbital forcing. Horizontal line shows critical obliquity above which sedimentary rock emplacement is permitted. (left) Stratigraphy of mound formation for this orbital forcing (late-stage erosion is not shown). Colored lines show stratigraphy. Black line is nonerodible container.

strongly nonuniform erosion (e.g., the canyons incised into Gale's mound) can create slopes that greatly differ from layer orientations. In Mars' mounds, layers are predicted to steepen upward in the stratigraphy, as subsequent layers jacket a more-gently-dipping mound core; the opposite of the geometry encountered in mountains on Earth. Although modeled dips tend to steepen up-stratigraphy, the dips of *exposed* layers can either steepen up-mound or remain constant, depending on the depth of late-stage erosion. Dip-steepness

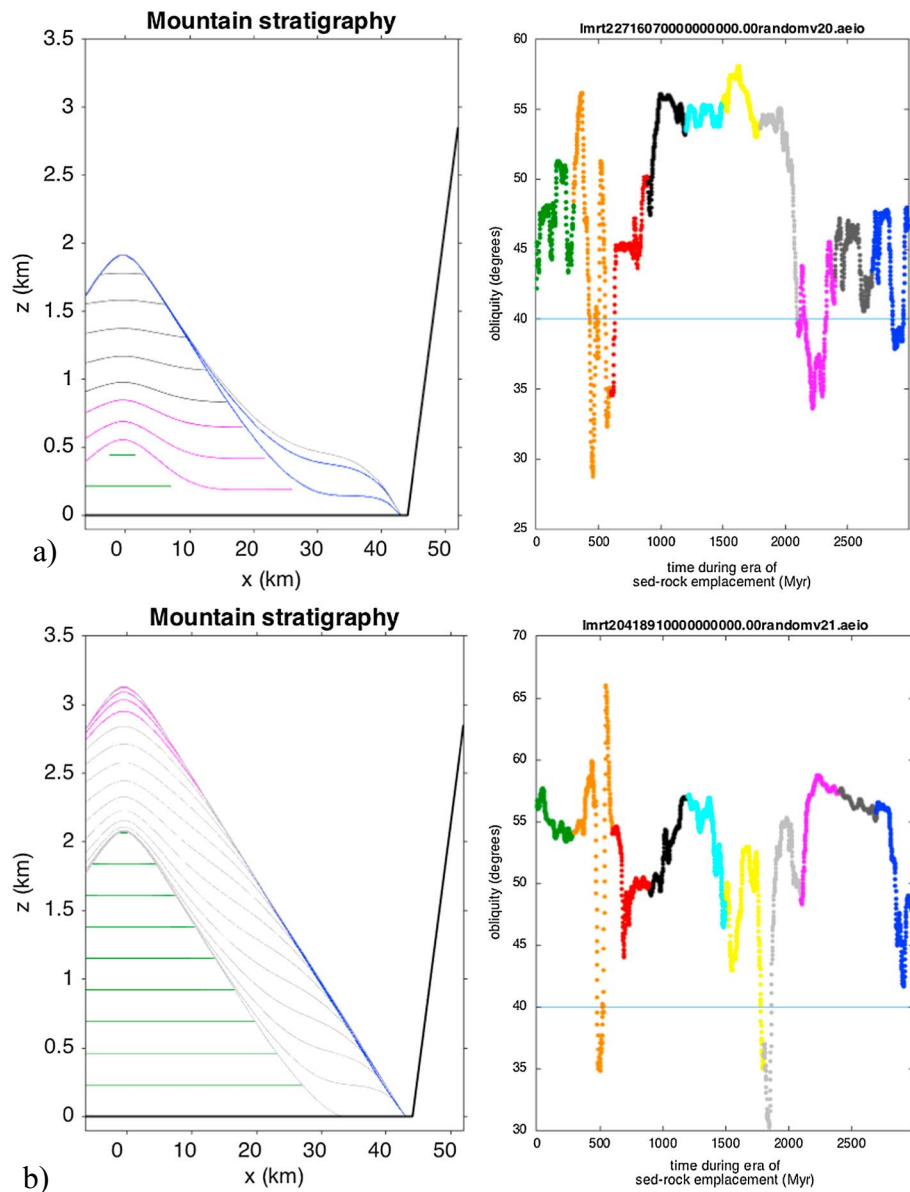


Figure 18. Additional examples of mound stratigraphies with their corresponding obliquity forcing, chosen to illustrate a range of interesting behavior. Text above the right-hand panels corresponds to the specific orbital forcing file used to force the simulation. These files are available from the lead author. Layers drawn every 20 Myr of simulated time, color change every 300 Myr. Notice the (a) within moat depositional package and the (c and d) “scabbed” depositional packages on the mound flank.

data show no clear trend with elevation, consistent with the model. Because chaotic shifts in mean obliquity are infrequent [Lissauer et al., 2012; Li and Batygin, 2014], the 1-2 large unconformities observed in some mounds suggest a (discontinuous) span of liquid water $\gg 100$ Myr long. This is consistent with the ~ 100 Myr lower bound estimated by rhythmic layering using only the thickness of the preserved sedimentary rock, and not accounting for unconformities [Lewis and Aharonson, 2014].

7. Discussion

7.1. Limitations of Data Interpretation

Anticompensational stacking can explain most of the layer orientations of most >1 km thick sulfate-dominated stratigraphies within deep and steep-sided craters/canyons. (The residuals might be due to gravity-driven slumping, or to deposition onto a paleosurface that had been wind-eroded into a

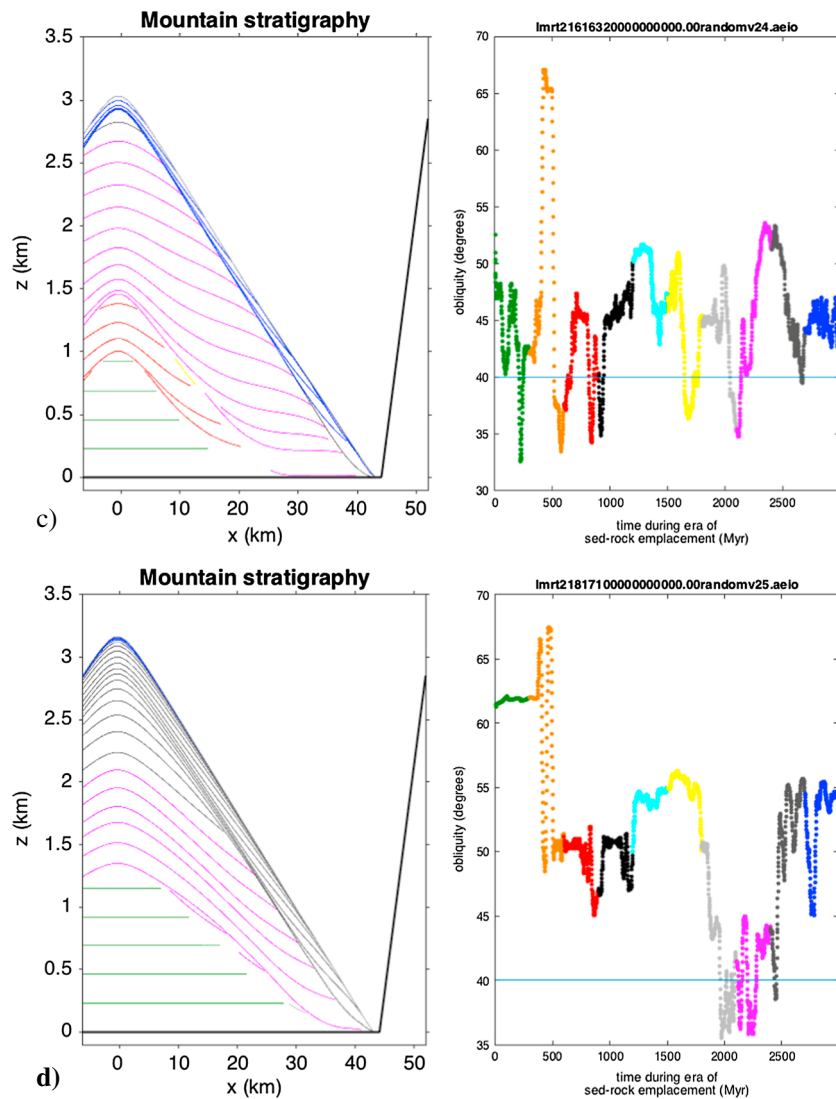


Figure 18. (continued)

nonaxisymmetric shape—e.g., the present topography of the mound in Nicholson crater). However, many Mars mound stratigraphies do not fall into this category. For example, sedimentary mounds in Terby crater [Ansan *et al.*, 2011] show a complicated 3-D stratal architecture that cannot be reproduced by the 2-D slope-winds model used here [Wilson *et al.*, 2007; Ansan *et al.*, 2011]. Mounds within-craters in West Arabia Terra have been argued to be outliers of a formerly more extensive deposit on the basis of geographic continuity [Zabrusky *et al.*, 2012; Bennett and Bell, 2016]. Geographic continuity makes predictions regarding the ice mounds encircling Mars' North Polar Layered Deposits that are known to be incorrect [Conway *et al.*, 2012; Brothers *et al.*, 2013; Brothers and Holt, 2016]; therefore, geographic continuity is inconclusive. Layer dip data are unavailable for these Arabia mounds.

A second key limitation of the anticompensational-stacking interpretation is that it does not work for small deposits. For example, small catenae contain layered deposits that dip inward [e.g., Weitz and Bishop, 2016], and small craters in Arabia show inward dipping layers in anaglyph (e.g., HiRISE PSP_001981_1825/PSP_0012258_1825). This proves that for small container size ($\ll 100$ km), anticompensational stacking is not effective. In turn, this suggests a critical length/depth scale above which slope winds are most effective (Appendix B). This means that our MRAMS mesoscale results need not contradict the Day *et al.* [2016] large-eddy simulation study (which emphasizes the role of unidirectional winds) but could simply refer to a different ($\gtrsim 100$ km) scale of Mars crater/canyon.

7.2. Assumptions and Limitations of Model

The biggest uncertainty in our landscape evolution model is sediment availability. Sediment is assumed to be available for sedimentary rock emplacement during depositional intervals, and sand is also assumed to be available for sandblasting. This assumption of “sufficient” sand/dust/ash in Mars’ past is motivated by modern data. Today, sand is present almost everywhere but (except in a few places) is probably not pervasive and persistent enough to armor steeply sloping bedrock over geologic time [Hayward *et al.*, 2014]. Present-day gross dust accumulation rates are not much less than inferred ancient sediment accumulation rates [Kinch *et al.*, 2007; Lewis and Aharonson, 2014]. The rate of production of fine-grained material would be greater in the past because the rates of volcanism, impacts, physical erosion, and chemical weathering were all greater in the past [e.g., Golombek *et al.*, 2006; Levy *et al.*, 2016; Carter *et al.*, 2013]. This motivates the assumption that over long timescales, sediment is not limiting. On shorter timescales that are not resolved by the landscape evolution model, peaks in both erosion and deposition will probably be tied to the passage of supplies of abundant sand (so sediment starvation might control mound buildup at <1 km stratigraphic scales). Even if sediment is available, it will not stay in one place for billions of years unless liquid water is available to indurate it. Because our data indicate that mound buildup continued after a topographic moat was defined (consistent with Okubo [2014]), regional groundwater flow is implausible as a water source for those upper layers, and so the water needed for upper mound cementation must be from a topdown water source such as rain or snowmelt [Clow, 1987; Niles and Michalski, 2009; Kite *et al.*, 2013b; Fairén *et al.*, 2014].

The most important assumption in the wind erosion model is that output from 6 mbar simulations is relevant to the times when most erosion (and sedimentation) occurred, when the atmospheric pressure was likely higher [e.g., Catling, 2009; Brain *et al.*, 2015]. Since the absolute erosion rate is nondimensionalized in our model, only the pattern of wind erosion matters. Strong slope winds are expected on long steep slopes provided that the atmosphere is thin enough to permit large day-night swings in temperature [Zardi and Whiteman, 2013]. Thus, we expect that terrain strongly influenced wind-erosion patterns in Mars’ past.

Currently, our model is detachment limited (i.e., only the scalar value of wind speed matters). Tackling detachment-limited processes first is simpler and is justified by that simplicity. We plan to investigate transport-limited behavior (i.e., convergence and divergence of sediment driven by wind vectors) in future work.

Patches of layered deposits veneer the slopes of some of the VM canyons [e.g., Fueten *et al.*, 2010, 2011]. Pasted-on wall-slope deposits can form in our model but tend to be removed by late-stage erosion. The observed persistence of these outliers highlights the limitations of our 2-D modeling approach. To investigate these outliers would require a fully coupled 3-D model of landscape-wind coevolution.

Although anticompensational stacking is the dominant behavior in our model, we did find cases where the slope winds model places lenses of sedimentary rock low down on the mound or in the moat (e.g., Figure 18a). These packages correspond to late-stage materials that are on close-to-modern topography. Possible real-world examples are (1) young materials in the moat SW of Ceti Mensa [Okubo, 2010], (2) the light-toned yardang-forming unit toward which the Mars Science Laboratory rover is driving, and (3) the Siccar Point group in Gale including the Stimson formation [Fraeman *et al.*, 2016].

In our model there is no *secular* climate change. This is unrealistic; secular climate change clearly occurred on Mars [Jakosky and Phillips, 2001]. Our calculations assume that climate change driven by chaotic alternations in mean obliquity introduces a large-amplitude overprint on secular change, and we focus on those alternations.

7.3. Geological Implications and Tests

Obliquity strongly influences the three limiting factors for sedimentary rock buildup on Mars: sediment supply, water supply, and erosion intensity. Orbitaly forced drape-and-scrape cycles produce a good match to observations (Figure 17). However, alternatives to φ -modulated accumulation exist. Secular variations in sediment supply, induced, for example, by regionally coordinated volcanism, could explain the unconformities. This could be tested by mapping longitudinal trends in unconformity patterns. Alternatively, volcanism might globally coordinate wet episodes via greenhouse forcing. However, volcanic greenhouse gases are either too long-lived (CO_2) or too short-lived (SO_2) to easily explain the modulations [Kerber *et al.*, 2015]. Ice/dust cover might intermittently shield rocks from abrasion, but latitudinal shifts of cover materials are likely to be

themselves φ paced. If the great unconformities are obliquity paced, then the time gaps at unconformities should be >100 Ma. This can be tested via counts of embedded craters. Only one time gap at a Mars unconformity has been constrained so far [Kite *et al.*, 2015], and the time gap is found to be >100 Ma, as predicted.

Latitudinal variations offer clues to mound origin. The biggest sedimentary mounds on Mars lie near the equator. These mounds have few obvious mound-spanning angular unconformities. By contrast, mounds poleward of $\pm 25^\circ$ (e.g., Galle and Terby) show numerous unconformities. This is expected for deposits forming at the margins of the latitudinal belt that permitted sedimentary rock formation [Kite *et al.*, 2013b]. The variation in mound height between canyons (the thickest deposits are in Northern VM, i.e., closer to Mars' equator) could be due to a preference for sedimentary rock emplacement near the equator [Kite *et al.*, 2013b]. Alternatively, greater erosion in the canyons that now have thinner deposits might explain the latitudinal trend. Tests include measuring layer thicknesses [e.g., Lewis and Aharonson, 2014; Cadieux and Kah, 2015] and unconformity spacings.

Further observations of stratal geometries, for example via detailed mapping [e.g., Fraeman *et al.*, 2016], could test our model's predictions that mound-spanning unconformities steepen up-stratigraphy, dip toward the canyon edge or crater rim, and are draped by parallel layers.

Obliquity-modulated buildup can be tested by the *Curiosity* rover's climb through sulfate-bearing layers toward the major unconformity at Gale's mound identified by Malin and Edgett [2000]. An origin via chaotic shifts in mean obliquity predicts that sedimentation episodes are long and few in number. φ control predicts long time gaps at unconformities (Figure 3), with gently dipping layers erosionally truncated and overlain by more-steeply-dipping layers draped over preexisting stratigraphy. Detection of gravels sourced from Gale's rim within strata high in Mount Sharp/Aeolis Mons would disprove our model. Instead, aeolian (and reworked-aeolian) deposits should dominate. Evidence for paleoerosion by wind should be common close to unconformities. Onlap at unconformities would support the hybrid hypothesis in Figure 16, whereas draping at unconformities would support the preferred interpretation in Figure 16.

Mound formation processes are tightly linked to early Mars runoff intermittency. Even small seasonal streams would suppress the sand migration that is required for saltation-driven erosion [Krapf, 2003], and gravity-driven stream erosion would also suppress the anticompensational growth of mounds. Aeolian sediment supply can be reconciled with lakes in VM [Harrison and Chapman, 2008] if climate permitted lakes for only a small percentage of years [Palucis *et al.*, 2016; Buhler *et al.*, 2014; Irwin *et al.*, 2015]. Wet-dry alternations during Mars' era of sedimentary-rock accumulation, including long dry periods, are predicted by our preferred scenario. Intermittent habitability is consistent with the persistence of surface olivine on Mars [Stopar *et al.*, 2006; Olsen and Rimstidt, 2007] and the detection in Gale mudstones of chemical markers for extreme aridity [Farley *et al.*, 2016]. Our data disfavor the long-standing hypothesis [McCauley, 1978] that the VM outcrops are lake deposits, but are consistent with a lacustrine origin for outcrops below the base of the topographically defined mounds in VM [Williams and Weitz, 2014] and below the clay/sulfate transition at Gale [Grotzinger *et al.*, 2015].

8. Conclusions

We introduce new data and a new model for the evolution of eight major sedimentary mounds in Valles Marineris and Gale crater.

Data:

1. Seven out of eight mounds investigated show layer orientations that dip systematically away from the mound centerline, with median dip 5° ($n = 308$).
2. Layer-orientation data have a precision and accuracy that are sufficient for the purpose of constraining mound origin.
3. Stratigraphic surfaces interpreted as major mound-spanning unconformities are well fit by a dome shape in six out of eight cases.

Interpretation:

1. When combined, the layer orientation data, draped landslides, and our interpretation of stratigraphic surfaces interpreted as unconformities require primary deposition of layers on outward-dipping slopes for the topmost ~ 1 km of the mounds.

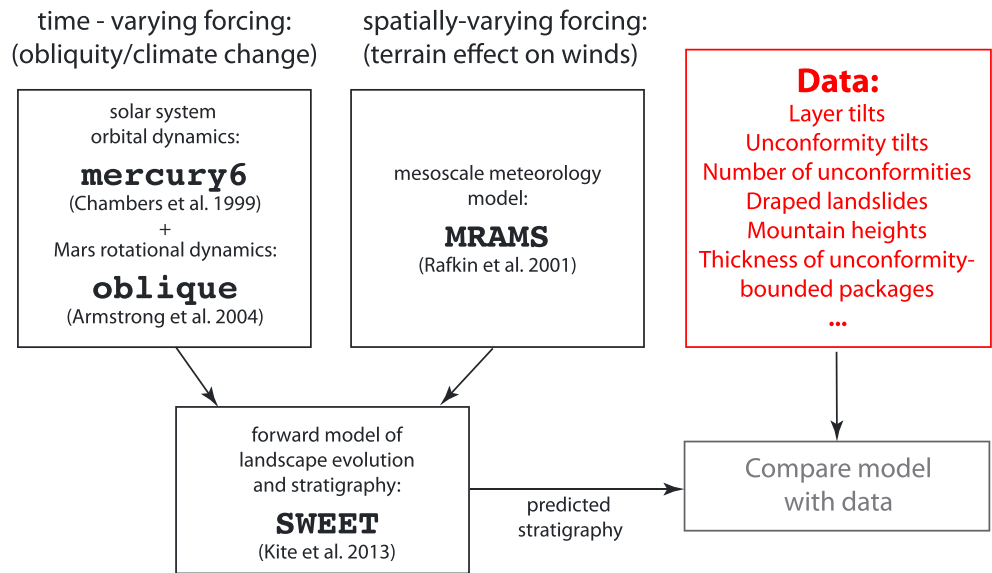


Figure A1. Sketch of SOURED model. Combining the MRAMS output with the obliquity forcing, we use the stratigraphic forward model to predict the structure of the mounds.

- Lower in the stratigraphy, the layer orientation data are consistent with either (i) primary deposition of layers on outward-dipping slopes [Kite *et al.*, 2013a] or (ii) a hybrid hypothesis in which slope-wind erosion sculpts precompacted sediments that later act as wedge-shaped indentors for differential compaction of later-deposited sediments.

Model:

- We present a model that combines spatially resolved forcing (from mesoscale meteorological simulations) and time-variable forcing (realistic orbital integrations) to make quantitative predictions for the evolution of the major sedimentary basins of Mars. The meteorological simulations confirm a strong trend of increasing wind stress with topographic slope within both craters and canyons.
- The model predicts that Mars mound stratigraphy emerges from a drape-and-scape cycle.
- The model simultaneously matches the following mound attributes: (i) layers dip away from mound crests; (ii) internal unconformities have a dome shape; (iii) average dip magnitudes cluster at the mound height:width ratio; (iv) unconformity-bounded stratigraphic packages thin upward; and (v) layer orientations frequently conform to modern topographic slope.
- We propose that major mound-spanning unconformities within Mars mountains correspond to periods of low mean obliquity [Mischna *et al.*, 2013; Kite *et al.*, 2015]. Because chaotic shifts in mean obliquity are infrequent, the 1-2 large unconformities observed in some mounds suggest a (discontinuous) span of liquid water $\gg 100$ Myr long. In our model, the major mound-spanning unconformities (once correctly oriented) can be used for planetwide correlation.
- On the Earth, first-order erosion-deposition alternations [Loss, 1963] are driven at a global scale by the Wilson cycle (via orogeny and eustasy). On Mars, climate changes driven by infrequent chaotic shifts in mean obliquity may play an analogous role in shaping the planet's sedimentary record.

Appendix Stratigraphic Model

A.1. Overview and Physical Basis of Stratigraphic Model

The central element of our SOURED model (Figure A1) is the forward model of landscape evolution and stratigraphy (section A.2), which incorporates time-varying sedimentary rock emplacement (assumed uniform within-craters/canyons for simplicity) and spatially varying feedback from slope winds. Time-varying sedimentary rock emplacement is forced by 3 Gyr long integrations of the orbit and spin-pole orientation of Mars (section A.3). Spatially varying feedback from slope winds is forced by a mesoscale wind model (Appendix B). Essentially, SOURED = an upgraded version of SWEET + MRAMS + (MERCURY6 + oblique) (Figure A1).

Slope winds are important on Mars. These diurnally reversing winds result from the combination of high relief and day-night temperature swings of up to 130 K [e.g., *Kass et al.*, 2003]. Slope winds are particularly strong within the equatorial craters and canyons that host sedimentary rock mounds, where Coriolis effects are weak and relief can approach 10 km. The coupling between long, steep slopes, and strong winds on Mars emerges from basic physical principles and is model-independent [*Spiga et al.*, 2011; *Kite et al.*, 2013a; *Zardi and Whiteman*, 2013; *Moreau et al.*, 2014; *Tyler and Barnes*, 2015; *Rafkin et al.*, 2016].

A.2. Stratigraphic Forward Model

The purpose of our forward stratigraphic model is to generate basin stratigraphies for comparison with observations. Earth models with the same purpose (but which simulate different physical processes) include SedSim [*Griffiths et al.*, 2001] and Dionisos [*Csato et al.*, 2014]. Our forward stratigraphic model is 2-D (one horizontal dimension and one vertical dimension), with a nominal resolution of ~1 km in the horizontal dimension and 1 Myr in time. Our model does not attempt to resolve processes operating at shorter scales of space and/or time.

The model is modified after the Slope-Wind Enhanced Erosion and Transport (SWEET) model of *Kite et al.* [2013a], with significant enhancements to incorporate parameterized erosion estimators obtained from mesoscale models and time-varying climate forcing (Figure A1). In SWEET,

$$dz/dt = D - e_E \quad (A1)$$

where D is deposition rate and e_E is erosion rate,

$$e_E = k_E U^\beta \quad (A2)$$

where k_E is an erodibility parameter, U is wind shear stress, and β is in the range 2–4 for wind-erosion processes [*Kok et al.*, 2012]. The threshold for sediment mobilization is omitted, which is a large simplification. Since the gap between the fluid threshold for saltation initiation and the impact threshold for saltation cessation is so large on Mars, the threshold is very uncertain. Large values of β produce a similar pattern of normalized wind erosion to large values of the mobilization threshold. Therefore, combining the threshold with β is a reasonable simplification. In earlier work [*Kite et al.*, 2013a] we treated the relative importance of slope winds (U_s) and background or “synoptic” winds U_0 as a free parameter,

$$U = U_0 + U_s \quad (A3)$$

where U_0 could be varied. Here we remove the free parameter U_0 by calculating erosion estimators directly from cell-by-cell mesoscale model output,

$$e_E(\beta, s) = k_E(\beta) \frac{1}{N_s} \frac{\Delta t}{(t - t_{su})} \sum_{s=0}^S \sum_{t_{su}}^t \tau_{s,t}^\beta \quad (A4)$$

where N_s is the number of grid cells with slopes (s) in the range of interest, t is total elapsed time, t_{su} is spin-up time ($t - t_{su}$ is always an integer number of Martian solar days (sols)), Δt is time step, τ_s is the instantaneous surface shear stress (in Pa), and β is from equation (A2). In practice we use a log-linear fit to the cell-by-cell data to get a smooth relationship between slope and erosion (Appendix B). k_E is adjusted to match the height of observed mounds. In the limit where erosion depends only on local slope (modeled here), and where $e_E \sim 0$ for $s = 0$, the model will tend to produce a cone (or triangular prism) of sedimentary rocks whose side-slope is $dz/dx = (D/k_E)^{1/\beta}$.

SWEET does not conserve mass locally. Instead, material is added from distant sources (e.g., by airfall), and eroded material is removed to a distant sink (e.g., the Martian lowlands) [*Grotzinger and Milliken*, 2012]. Layers in the model are assumed to be indurated (mobile sand is assumed to be topographically superficial or to have a geologically short residence time). Because induration probably involves cementation by mineral precipitation from aqueous fluids, long-term secular decline in Mars’ ability to form sedimentary rocks (due to, for example, water loss and CO₂ loss) means that the model is most applicable to early Mars.

A.3. Orbital Dynamics Model and Obliquity Model

The purpose of our orbital dynamics model and obliquity model is to generate an ensemble of realistic 3.1 Gyr long obliquity tracks for Mars [*Kite et al.*, 2015]. We generated ϕ tracks using MERCURY6 (the N-body

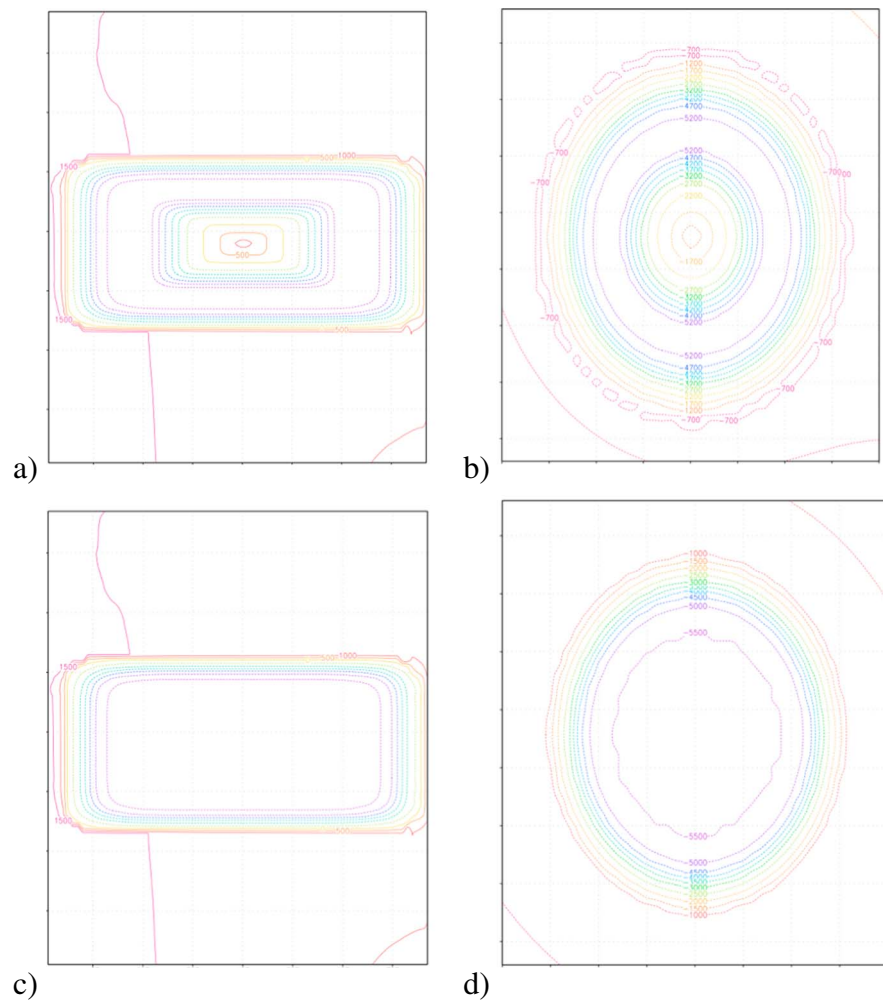


Figure B1. Topographies investigated using MRAMS simulations. Contours at 500 m intervals. (a) Rectangular canyon, width ~130 km and length ~350 km, with full-height mound. (b) Crater, 155 km diameter, with full-height mound. (c) Flat-floored canyon without sediment infill. (d) Flat-floored crater without sediment infill.

code of *Chambers* [1999]) and the obliquity code of *Armstrong et al.* [2004, 2014]. For each >3 Gyr long eight-planet solar system integration ($n = 37$) (the combined eccentricity pdf from these integrations is very similar to that of *Laskar et al.* [2004]), we seeded 24 Mars ϕ tracks drawing the initial ϕ from the long-term distribution of *Laskar et al.* [2004]. From the ensemble, we selected those ϕ tracks which ended (after 3.1 Gyr) in the range 20° – 35° (consistent with present-day Mars ϕ). The figures in this paper show a subset of the stratigraphic output forced by those ϕ tracks, chosen to illustrate a range of common stratigraphic outcomes.

Appendix Mesoscale Model

B.1. Mesoscale Model Input

The purpose of our mesoscale modeling work is to verify that wind stress increases with topographic slope. We also seek the “slope enhancement factor”—to what extent is erosion rate (assumed to scale as wind stress to some power β) faster on steep slopes than on flat slopes within-craters/canyons? We have already verified [*Kite et al.*, 2013a], using the MarsWRF model [*Toigo et al.*, 2012; *Richardson et al.*, 2007], that the strongest winds are on the steepest slopes for a simulation of 1 year’s winds at Gale crater. Here we use the Mars Regional Atmospheric Modeling System [*Rafkin et al.*, 2001] to extend our earlier results through exploring a range of idealized topographies [*Tyler and Barnes*, 2015; *Day et al.*, 2016]. MRAMS is derived from the terrestrial RAMS model [*Mahrer and Pielke*, 1976]. MRAMS has been used to model the entry and descent of all

NASA Mars landers subsequent to Pathfinder [Michaels and Rafkin, 2008; Rafkin and Michaels, 2003]. We use a horizontal resolution of 4.4 km and a vertical resolution varying from 15 m near the surface to >1 km at high altitude. A realistic diurnal cycle in insolation is imposed (including planetary-scale thermal tides). Our runs are carried out at 6 mbar; the pattern of wind forcing should be similar for other atmospheres that are thin enough for a large day-night cycle in surface temperature. The orbital parameters are for modern Mars, but the diurnally reversing mesoscale circulation should operate similarly at high obliquity (the background winds may be stronger) [Haberle et al., 2003; Newman et al., 2005]. Boundary conditions are supplied by the NASA Ames Mars General Circulation Model [Haberle et al., 1993]. For this project, we modify MRAMS to simulate idealized craters and idealized canyons. We use smoothed background topography and insert oblong canyons of width ~ 130 km and length ~ 350 km and depth ~ 4.5 km. We run the model both without mounds and for canyons containing mounds of 100% of the full height of the canyon (Figure B1). These runs correspond to idealized topography for a large canyon hosting a large mound (e.g., Candor, Hebes, and Ophir). Separately, we insert 4.5 km deep, 155 km diameter axisymmetric craters (Figure B1), with their corresponding mounds. These runs correspond to idealized topography for a large crater hosting a large mound (e.g., Gale crater and Nicholson crater). We ran for 5.7 day-night cycles for solar longitude $L_s = \{30^\circ, 90^\circ, 150^\circ, 180^\circ, 210^\circ, 270^\circ, 330^\circ\}$. The first 1.7 sols are discarded as spin-up. Simulated crater/canyon latitude is $\sim 5^\circ\text{S}$.

B.2. Mesoscale Model Output

Our MRAMS runs confirm that the strongest winds within-craters/canyons are associated with diurnally reversing (anabatic/katabatic) flows and are located on the steepest slopes (Figure B2). Terrain-controlled circulation dominates the overall circulation inside our idealized craters and canyons (consistent with Tyler and Barnes [2015]) (Figure B3). The importance of slope winds in our idealized-topography runs is somewhat offset for real craters and canyons by regional effects (e.g., the planetary topographic dichotomy boundary) [Rafkin et al., 2016]. To simplify the analysis, we assume cell-scale (4 km scale) control of terrain on wind stress. Grid cells inside a canyon or crater are generally less windy than on the plateau surrounding the depression (Figure B3). This is partly because the plateau is subject to the morning “surge” of air moving away from the canyon [Tyler and Barnes, 2015]. However, within the crater/canyon, wind stress is about 5 times greater for 15° slopes than for flat surfaces. Points just below the rim of the crater/canyon have stronger wind stress than expected for their slope, because they participate in the morning surge of air moving away from the crater/canyon. The scatter of mean wind stress is about a factor of 2. We use the crater output; the same trends were found for canyons as for craters.

How we get from mesoscale model output to erosion estimators: Even if our wind models perfectly represented wind stresses inside Mars craters/canyons, which would not be enough to correctly diagnose the rate of aeolian erosion of bedrock. Aeolian erosion of rock is a multistep process [Shao, 2008; Kok et al., 2012], and it is difficult to determine the rate-limiting step from orbit. Possibilities include breakdown of sedimentary layers to wind-transportable fragments by weathering and/or volume changes associated with hydration state changes [e.g., Chipera and Vaniman, 2007]; physical degradation by mass wasting, combined with aeolian removal of talus [Kok et al., 2012; Martin and Kok, 2016]; aeolian erosion of weakly salt-cemented sediments [Shao, 2008]; and aeolian abrasion of bedrock [Wang et al., 2011]. Rather than attempting to directly predict erosion rate, we use the strong evidence for geologically recent wind erosion of the mounds [e.g., Day et al., 2016] to establish the feasibility of aeolian sculpting of the mounds, and we use the wind models to get the pattern of past wind erosion. This requires us to accept two limitations:

1. The relationship between wind stress and erosion rate will vary depending on both past atmospheric pressure and the details of the erosion process. We parameterize this uncertainty by a power-law exponent, β .
2. Wind erosion is not carried out by the wind directly, but by sand grains carried by the wind (at least for most erosion processes), and sand grains are not tracked by the model. This is directly analogous to the tools-and-cover problem in modeling the evolution of Earth's mountains [e.g., Sklar and Dietrich, 1998, 2006] (section 7).

To get the relationship between wind stress and slope, we tried fitting the unbinned data with various functions (exponential, two-exponential, power-law, polynomial, etc.). The most visually satisfying fit is a log-linear function. The fit suffices to capture the basic tendency for wind erosion within-craters and canyons to be stronger on steep slopes than on gentle slopes, by a factor of between ~ 4 (if erosion is proportional to mean wind stress) and >10 (if erosion is proportional to wind stress raised to the fourth power).

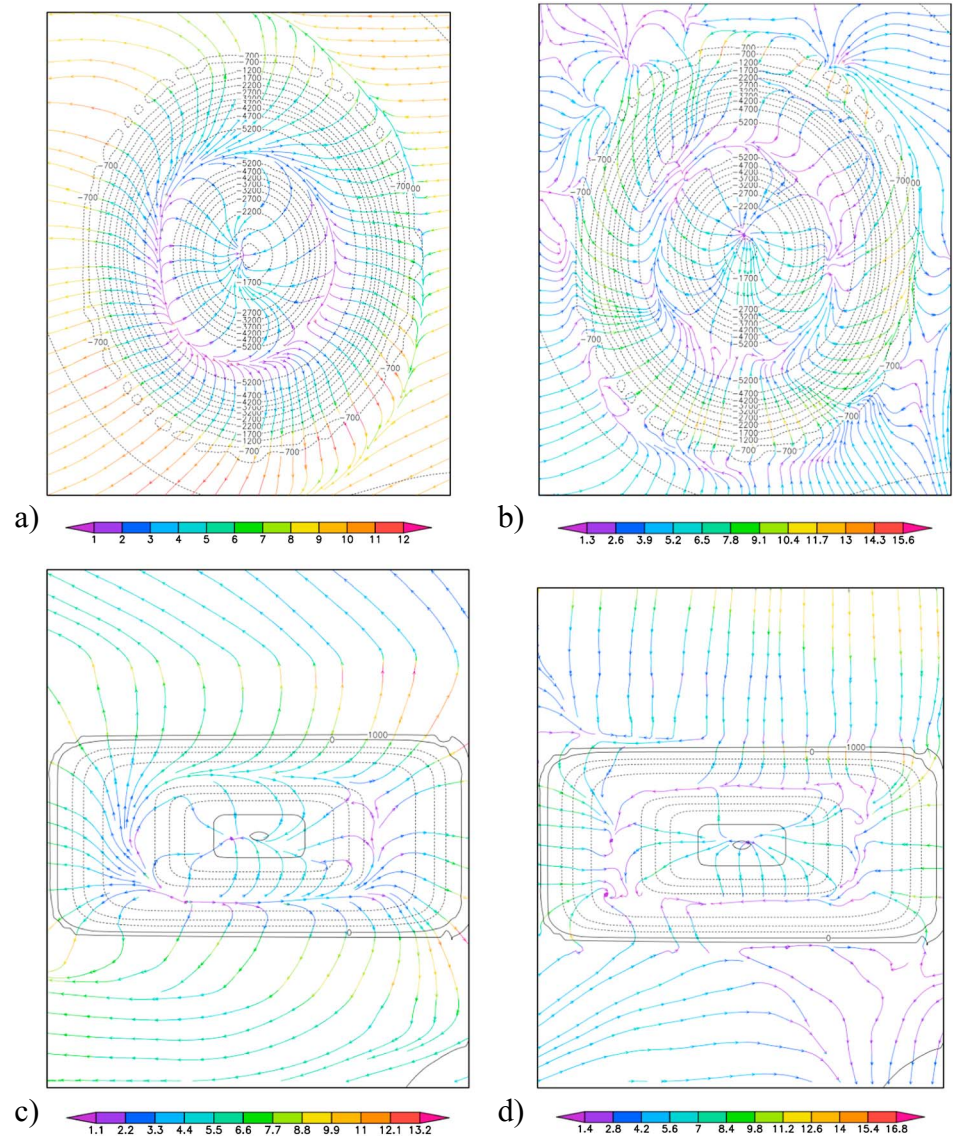


Figure B2. Winds are strong on crater/canyon walls and on mound flanks, but weak in the moat. (a) Snapshot of daytime flow in idealized-topography crater, dominated by upslope (anabatic) winds. Contours (m) are elevation. Colors are wind speed (m/s) at 15 m elevation. Topographic contour interval 500 m. (b) Snapshot of nighttime flow in idealized-topography crater, dominated by downslope (katabatic) winds. Topographic contour interval 500 m. (c) Snapshot of daytime flow in idealized-topography canyon, dominated by upslope (anabatic) winds. Topographic contour interval 1000 m. (d) Snapshot of nighttime flow in idealized-topography canyon, dominated by downslope (katabatic) winds. Topographic contour interval 1000 m. (This figure was produced using the Grid Analysis and Display System, <http://cola.gmu.edu/grads/>).

We defined erosion estimators from the MRAMS model output on a per grid cell basis as follows:

$$e_E(\beta) = \frac{k_E(\beta)}{(t - t_{su})} \int_{t_{su}}^t \tau_{sw}^\beta dt \quad (B5a)$$

$$e_E(\beta, s) = k_E(\beta) 10^{k_1(\beta)s + k_2(\beta)}. \quad (B5b)$$

We obtained e_E by regression using a log-linear fit where $e_E = 10^{(k_1 s + k_2)}$, where s is slope. We did this for the 100% mound simulation (mound-in-crater) (Figure B3). The erosion estimators are (for $\beta = 1$, i.e., erosion proportional to mean wind speed) $k_1 = 3.08(2.84, 3.31)$, $k_2 = -3.37(-3.41, -3.33)$, (for $\beta = 2$) $k_1 = 5.34(4.87, 5.82)$, $k_2 = -6.34(-6.42, -6.26)$, (for $\beta = 3$) $k_1 = 7.44(6.69, 8.18)$, $k_2 = -9.13(-9.26, -9.01)$, and (for $\beta = 4$) $k_1 = 9.42(8.39, 10.44)$, $k_2 = -11.81(-11.98, -11.64)$. Here the brackets give the formal confidence interval of the fits.

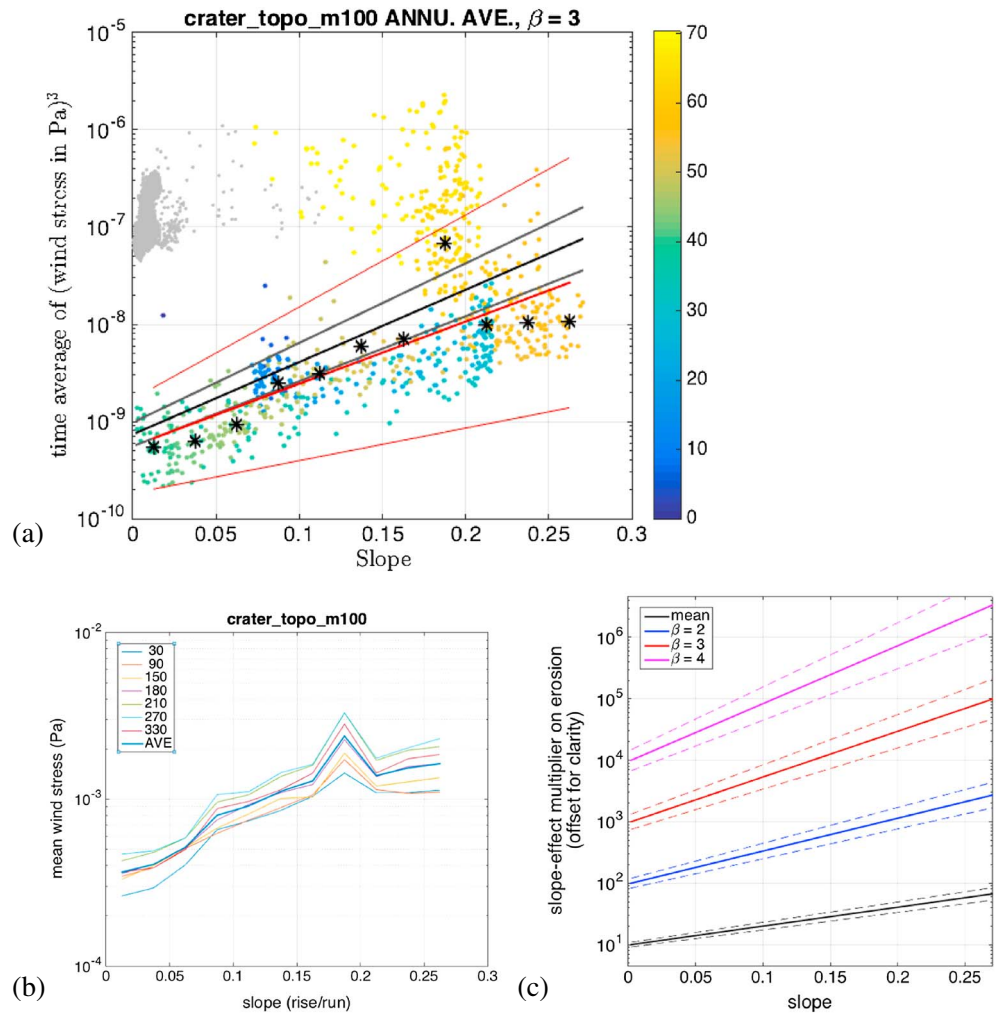


Figure B3. MRAMS run-integrated output. (a) Maximum wind stress from the last 4 sols of model runs, for topographic boundary conditions featuring large central mounds. Model output is binned according to grid cell slope, and the median for each bin is shown (stars). Color scale corresponds to distance from mound center in kilometers. The black line (and gray error bars) corresponds to the best log-linear fit to all data. The red line (and red error bars) corresponds to the best log-linear fit to the binned data (asterisk). (b) Mean wind stress from the last 4 sols of model runs at different seasons, for topographic boundary conditions corresponding to a full-height central mound inside a crater. The numbers in the legend correspond to the L_s (Martian season) of each run. (c) The overall best fits to the slope-effect multiplier (offset for clarity; for slope = 0, the slope-multiplier effect is 1 by definition).

The choice of erosion estimator depends on the paleoatmospheric pressure and on the mechanism of erosion. For low atmospheric pressure, u_{cr}^* (the surface-stress threshold for sand motion) approaches the maximum wind speed, and $\beta \rightarrow \infty$ (i.e., erosion only responds to the very strongest gusts). Sand dunes on Mars today are in active motion [Bridges *et al.*, 2012a], so $\beta < \infty$. When atmospheric pressure was higher earlier in Mars history, u_{cr}^* would become small compared to frequently encountered wind speeds. Under those circumstances, $2 < \beta < 4$ is appropriate. We used $\beta = 3$ to make the plots shown in this paper. We carried out sensitivity tests changing the β parameter, finding no qualitative difference for $2 < \beta < 4$ (after adjustment for each β of the dimensionless deposition rate in order to match observed mound heights).

The past terrain-averaged erosion rate is effectively a free parameter in our model. We find good results with maximum past rates that are comparable to Earth wind erosion rates, that agree with previous calculations of peak present-day Mars wind erosion rates [Bridges *et al.*, 2012b], and that are 1 order of magnitude greater than typical present-day Mars sedimentary rock wind erosion rates [Golombek *et al.*, 2014; Kite and Mayer, 2016], consistent with higher atmospheric pressure (or weaker rocks) in the past.

Acknowledgments

We thank Michael Lamb, Frank Fueten, Gene Schmidt, Chris Okubo, Leila Gabasova, John Grotzinger, Jeff Andrews-Hanna, Mackenzie Day, Jeff Barnes, Daniel Tyler, Claire Newman, Mark Richardson, John Armstrong, Bill Dietrich, Jasper Kok, Matt Chojnacki, Corey Fortezzo, Baerbel Lucchitta, Nathan Bridges, Brad Thomson, Martin Jackson, and David Rowley for enlightening comments and discussions and for sharing unpublished data. We thank four reviewers for timely, thorough, and thoroughly useful reviews. We thank the HiRISE team for maintaining the HiWish program, which provided multiple images that were valuable for this work. We thank UChicago's Research Computing Center. This work was financially supported by the U.S. taxpayer via NASA grant NNX15AH98G. Layer-orientation data are available as a supporting information Table S1. DTM scripts are written in Bash and are available for download from https://psd-repo.uchicago.edu/kite-lab/uchicago_asp_scripts/. DTMs and other data produced for this study may be obtained for unrestricted further use by contacting the lead author (kite@uchicago.edu).

References

- Allen, C. C., A. M. Dapremont, and D. Z. Oehler (2014), The complex, multi-stage history of Mt. Sharp, 45th Lunar and Planetary Science Conference, The Woodlands, Tex., LPI Contribution No. 1777, p. 1402.
- Allen, P. A., and J. R. Allen (2013), *Basin Analysis*, 3rd ed., Wiley-Blackwell, Chichester, West Sussex, U. K.
- Anderson, R. B., and J. F. Bell III (2010), Geologic mapping and characterization of Gale Crater and implications for its potential as a Mars Science Laboratory landing site, *Int. J. Mars Sci. Explor.*, 4, 76–128.
- Anderson, R. C., J. M. Dohm, M. P. Golombek, A. F. C. Haldemann, B. J. Franklin, K. L. Tanaka, J. Lias, and B. Peer (2001), Primary centers and secondary concentrations of tectonic activity through time in the western hemisphere of Mars, *J. Geophys. Res.*, 106(E9), 20,563–20,586, doi:10.1029/2000JE001278.
- Andrews-Hanna, J. C. (2012a), The formation of Valles Marineris: 3. Trough formation through super-isostasy, stress, sedimentation, and subsidence, *J. Geophys. Res.*, 117, E06002, doi:10.1029/2012JE004059.
- Andrews-Hanna, J. C. (2012b), The formation of Valles Marineris: 1. Tectonic architecture and the relative roles of extension and subsidence, *J. Geophys. Res.*, 117, E03006, doi:10.1029/2011JE003953.
- Andrews-Hanna, J. C., and K. W. Lewis (2011), Early Mars hydrology: 2. Hydrological evolution in the Noachian and Hesperian epochs, *J. Geophys. Res.*, 116, E02007, doi:10.1029/2010JE003709.
- Andrews-Hanna, J. C., M. T. Zuber, R. E. Arvidson, and S. M. Wiseman (2010), Early Mars hydrology: Meridiani playa deposits and the sedimentary record of Arabia Terra, *J. Geophys. Res.*, 115, E06002, doi:10.1029/2009JE003485.
- Ansan, V., et al. (2011), Stratigraphy, mineralogy, and origin of layered deposits inside Terby crater, Mars, *Icarus*, 211, 273–304.
- Armstrong, J. C., and C. B. Leovy (2005), Long term wind erosion on Mars, *Icarus*, 176(1), 57–74.
- Armstrong, J. C., C. B. Leovy, and T. Quinn (2004), A 1 Gyr climate model for Mars: New orbital statistics and the importance of seasonally resolved polar processes, *Icarus*, 171, 255–271.
- Armstrong, J. C., R. Barnes, S. Domagal-Goldman, J. Breiner, T. R. Quinn, and V. S. Meadows (2014), Effects of extreme obliquity variations on the habitability of exoplanets, *Astrobology*, 14, doi:10.1089/ast.2013.1129.
- Arvidson, R. E., et al. (2006), Nature and origin of the hematite-bearing plains of Terra Meridiani based on analyses of orbital and Mars Exploration rover data sets, *J. Geophys. Res.*, 111, E12S08, doi:10.1029/2006JE002728.
- Arvidson, R. E., et al. (2015), Mars Reconnaissance Orbiter and Opportunity observations of the Burns formation: Crater hopping at Meridiani Planum, *J. Geophys. Res. Planets*, 120, 429–451, doi:10.1002/2014JE004686.
- Ayoub, F., J.-P. Avouac, C. E. Newman, M. I. Richardson, A. Lucas, S. Leprince, and N. T. Bridges (2014), Threshold for sand mobility on Mars calibrated from seasonal variations of sand flux, *Nat. Commun.*, 5, 5096.
- Baioni, D. (2013), Morphology and geology of an interior layered deposit in the western Tithonium Chasma, Mars, *Planet. Space Sci.*, 89, 140–150.
- Banham, S. G., S. Gupta, D. M. Rubin, J. A. Watkins, D. Y. Sumner, J. P. Grotzinger, K. W. Lewis, K. S. Edgett, L. A. Edgar, and K. M. Stack (2016), Reconstruction of an Ancient Eolian Dune Field at Gale Crater, Mars: Sedimentary analysis of the Stimson Formation, 47th Lunar and Planetary Science Conference, held March 21–25, 2016 at The Woodlands, Tex., LPI Contribution No. 1903, p. 2346.
- Bennett, K. A., and J. F. Bell (2016), A global survey of Martian central mounds: Central mounds as remnants of previously more extensive large-scale sedimentary deposits, *Icarus*, 264, 331–341.
- Bernhardt, H., D. Reiss, H. Hiesinger, and M. A. Ivanov (2016), The honeycomb terrain on the Hellas basin floor, Mars: A case for salt or ice diapirism, *J. Geophys. Res. Planets*, 121, 714–738, doi:10.1002/2016JE005007.
- Beyer, R. A., O. Alexandrov, and Z. M. Moratto (2014), Aligning terrain model and laser altimeter point clouds with the Ames Stereo Pipeline, 45th Lunar and Planetary Science Conference, LPI Contribution No. 1777, p. 2902.
- Bibring, J.-P., et al. (2006), Global mineralogical and aqueous Mars history derived from OMEGA/Mars express data, *Science*, 312(5772), 400–404.
- Bibring, J.-P., et al. (2007), Coupled ferric oxides and sulfates on the Martian surface, *Science*, 317(5842), 1206.
- Bishop, J. L., et al. (2009), Mineralogy of Juventae Chasma: Sulfates in the light-toned mounds, mafic minerals in the bedrock, and hydrated silica and hydroxylated ferric sulfate on the plateau, *J. Geophys. Res.*, 114, E00D09, doi:10.1029/2009JE003352.
- Borlina, C. S., B. L. Ehlmann, and E. S. Kite (2015), Modeling the thermal and physical evolution of Mount Sharp's sedimentary rocks, Gale Crater, Mars: Implications for diagenesis on the MSL Curiosity rover traverse, *J. Geophys. Res. Planets*, 120, 1396–1414, doi:10.1002/2015JE004799.
- Bradley, B. A., Sakimoto, S. E. H., Frey, H., Zimbelman, J. R. (2002), Medusae Fossae Formation: New perspectives from Mars Global Surveyor, *J. Geophys. Res.*, 107(E8), 5058, doi:10.1029/2001JE001537.
- Brain, D. A., and B. M. Jakosky (1998), Atmospheric loss since the onset of the Martian geologic record: Combined role of impact erosion and sputtering, *J. Geophys. Res.*, 103(E10), 22,689–22,694, doi:10.1029/98JE02074.
- Brain, D. A., et al. (2015), The spatial distribution of planetary ion fluxes near Mars observed by MAVEN, *Geophys. Res. Lett.*, 42, 9142–9148, doi:10.1002/2015GL065293.
- Bridges, N., P. Geissler, S. Silvestro, and M. Banks (2013), Bedform migration on Mars: Current results and future plans, *Aeolian Res.*, 9, 133–151.
- Bridges, N. T., et al. (2012a), Planet-wide sand motion on Mars, *Geology*, 40(1), 31–34.
- Bridges, N. T., F. Ayoub, J.-P. Avouac, S. Leprince, A. Lucas, and S. Mattson (2012b), Earth-like sand fluxes on Mars, *Nature*, 485(7398), 339–342.
- Brothers, T. C., and J. W. Holt (2016), 3-dimensional structure and origin of a 1.8-km-thick ice dome within Korolev Crater, Mars, *Geophys. Res. Lett.*, 43, 1443–1449, doi:10.1002/2015GL066440.
- Brothers, T. C., J. W. Holt, and A. Spiga (2013), Orbital radar, imagery, and atmospheric modeling reveal an aeolian origin for Abalos Mensa, Mars, *Geophys. Res. Lett.*, 40, 1334–1339, doi:10.1002/grl.50293.
- Buhler, P. B., C. I. Fassett, J. W. Head, and M. P. Lamb (2014), Timescales of fluvial activity and intermittency in Milna Crater, Mars, *Icarus*, 241, 130–147.
- Burr, D. M., M.-T. Enga, R. M. E. Williams, J. R. Zimbelman, A. D. Howard, and T. A. Brennand (2009), Pervasive aqueous paleoflow features in the Aeolis/Zephyria Plana region, Mars, *Icarus*, 200, 52–76.
- Cadieux, S. B., and L. C. Kah (2015), To what extent can intracrater layered deposits that lack clear sedimentary textures be used to infer depositional environments?, *Icarus*, 248, 526–538.
- Carter, J., F. Poulet, J.-P. Bibring, N. Mangold, and S. Murchie (2013), Hydrous minerals on Mars as seen by the CRISM and OMEGA imaging spectrometers: Updated global view, *J. Geophys. Res. Planets*, 118, 831–858, doi:10.1029/2012JE004145.
- Catling, D. C. (2009), Atmospheric evolution of Mars, in *Encyclopedia of Paleoclimatology and Ancient Environments*, edited by V. Gornitz, pp. 66–75, Springer, Dordrecht.

- Catling, D. C., S. E. Wood, C. Leovy, D. R. Montgomery, H. M. Greenberg, C. R. Glein, and J. M. Moore (2006), Light-toned layered deposits in Juventae Chasma, Mars, *Icarus*, *181*, 26–51.
- Chambers, J. E. (1999), A hybrid symplectic integrator that permits close encounters between massive bodies, *Mon. Not. R. Astron. Soc.*, *304*, 793–799.
- Chapman, M. G., and K. L. Tanaka (2001), Interior trough deposits on Mars: Subice volcanoes?, *J. Geophys. Res.*, *106*(E5), 10,087–10,100, doi:10.1029/2000JE001303.
- Chipera, S. J., and D. T. Vaniman (2007), Experimental stability of magnesium sulfate hydrates that may be present on Mars, *Geochim. Cosmochim. Acta*, *71*, 241–250.
- Chojnacki, M., and B. M. Hynek (2008), Geological context of water-altered minerals in Valles Marineris, Mars, *J. Geophys. Res.*, *113*, E12005, doi:10.1029/2007JE003070.
- Chojnacki, M., J. E. Moersch, and D. M. Burr (2010), Climbing and falling dunes in Valles Marineris, Mars, *Geophys. Res. Lett.*, *37*, L08201, doi:10.1029/2009GL042263.
- Christensen, P. R., R. V. Morris, M. D. Lane, J. L. Bandfield, and M. C. Malin (2001), Global mapping of Martian hematite mineral deposits: Remnants of water-driven processes on early Mars, *J. Geophys. Res.*, *106*, 23,873–23,886, doi:10.1029/2000JE001415.
- Clow, G. D. (1987), Generation of liquid water on Mars through the melting of a dusty snowpack, *Icarus*, *72*, 95–127.
- Conway, S. J., N. Hovius, T. Barnie, J. Besserer, S. Le Mouéléc, R. Orosei, and N. Read (2012), Climate-driven deposition of water ice and the formation of mounds in craters in Mars' north polar region, *Icarus*, *220*, 174–193.
- Csato, I., O. Catuneanu, and D. Granjeon (2014), Millennial-scale sequence stratigraphy: Numerical simulation with Dionisos, *J. Sediment. Res.*, *84*, 394–406.
- Davies, R. J., and J. Cartwright (2002), A fossilized Opal A to Opal C/T transformation on the northeast Atlantic margin, *Basin Res.*, *14*, 467–486.
- Davis, B. J. (2007), Erosion-driven uplift and tectonics at Valles Marineris, Mars, Colorado School of Mines, MSci thesis.
- Day, M., and G. Kocurek (2016), Observations of an aeolian landscape: From surface to orbit in Gale Crater, *Icarus*, *280*, 37–71, doi:10.1016/j.icarus.2015.09.042.
- Day, M., W. Anderson, G. Kocurek, and D. Mohrig (2016), Carving intracrater layered deposits with wind on Mars, *Geophys. Res. Lett.*, *43*, 2473–2479, doi:10.1002/2016GL068011.
- Edgar, L., J. P. Grotzinger, A. G. Hayes, D. M. Rubin, S. W. Squyres, J. F. Bell, and K. E. Herkenhoff (2012), Stratigraphic architecture of bedrock reference section, Victoria Crater, Meridiani Planum, Mars, in *Sedimentary Geology of Mars, SEPM Spec. Publ.*, vol. 102, edited by J. Grotzinger and R. Milliken, pp. 195–209.
- Ehlmann, B. L., and J. F. Mustard (2012), An in-situ record of major environmental transitions on early Mars at Northeast Syrtis Major, *Geophys. Res. Lett.*, *39*, L11202, doi:10.1029/2012GL051594.
- Ehlmann, B. L., J. F. Mustard, S. L. Murchie, J.-P. Bibring, A. Meunier, A. A. Fraeman, and Y. Langevin (2011), Subsurface water and clay mineral formation during the early history of Mars, *Nature*, *479*(7371), 53–60.
- Fairén, A. G., et al. (2014), A cold hydrological system in Gale crater, Mars, *Planet. Space Sci.*, *93*, 101–118.
- Farley, K. A., et al. (2014), In situ radiometric and exposure age dating of the Martian surface, *Science*, *343*, 1247166.
- Farley, K. A., et al. (2016), Light and variable $^{37}\text{Cl}/^{35}\text{Cl}$ ratios in rocks from Gale Crater, Mars: Possible signature of perchlorate, *Earth Planet. Sci. Lett.*, *438*, 14–24.
- Fassett, C. I., and J. W. Head III (2007), Layered mantling deposits in northeast Arabia Terra, Mars: Noachian-Hesperian sedimentation, erosion, and terrain inversion, *J. Geophys. Res.*, *112*, E08002, doi:10.1029/2006JE002875.
- Fassett, C. I., and J. W. Head (2011), Sequence and timing of conditions on early Mars, *Icarus*, *211*, 1204–1214.
- Fastook, J. L., J. W. Head, D. R. Marchant, and F. Forget (2008), Tropical mound glaciers on Mars: Altitude-dependence of ice accumulation, accumulation conditions, formation times, glacier dynamics, and implications for planetary spin-axis/orbital history, *Icarus*, *198*(2), 305–317.
- Ferguson, R. L., L. R. Gaddis, and A. D. Rogers (2014), Hematite-bearing materials surrounding Candor Mensa in Candor Chasma, Mars: Implications for hematite origin and post-emplacement modification, *Icarus*, *237*, 350–365.
- Forget, F., R. Wordsworth, E. Millour, J.-B. Madeleine, L. Kerber, J. Leconte, E. Marcq, and R. M. Haberle (2013), 3D modelling of the early Martian climate under a denser CO₂ atmosphere: Temperatures and CO₂ ice clouds, *Icarus*, *222*, 81–99.
- Fortezzo, C. M., A. L. Gullikson, J. A. P. Rodriguez, T. Platz, and P. S. Kumar (2016), Mapping Geology in Central Valles Marineris, Mars, 47th Lunar and Planetary Science Conference, held March 21–25, 2016 at The Woodlands, Tex., LPI Contribution No. 1903, p. 1981.
- Fraeman, A. A., et al. (2013), A hematite-bearing layer in Gale Crater, Mars: Mapping and implications for past aqueous conditions, *Geology*, *41*, 1103–1106.
- Fraeman, A. A., B. L. Ehlmann, R. E. Arvidson, C. S. Edwards, J. P. Grotzinger, R. E. Milliken, D. P. Quinn, and M. S. Rice (2016), The stratigraphy and evolution of lower Mount Sharp from spectral, morphological, and thermophysical orbital data sets, *J. Geophys. Res. Planets*, *121*, 1713–1736, doi:10.1002/2016JE00509.
- Fuete, F., R. Stesky, P. MacKinnon, E. Hauber, K. Gwinner, F. Scholten, T. Zegers, and G. Neukum (2006), A structural study of an interior layered deposit in southwestern Candor Chasma, Valles Marineris, Mars, using high resolution stereo camera data from Mars Express, *Geophys. Res. Lett.*, *33*, L07202, doi:10.1029/2005GL025035.
- Fuete, F., R. Stesky, P. MacKinnon, E. Hauber, T. Zegers, K. Gwinner, F. Scholten, and G. Neukum (2008), Stratigraphy and structure of interior layered deposits in West Candor Chasma, Mars, from High Resolution Stereo Camera (HRSC) stereo imagery and derived elevations, *J. Geophys. Res.*, *113*, E10008, doi:10.1029/2007JE003053.
- Fuete, F., H. Racher, R. Stesky, P. MacKinnon, E. Hauber, P. C. McGuire, T. Zegers, and K. Gwinner (2010), Structural analysis of interior layered deposits in Northern Coprates Chasma, Mars, *Earth Planet. Sci. Lett.*, *294*(3–4), 343–356.
- Fuete, F., J. Flahaut, L. Le Deit, R. Stesky, E. Hauber, and K. Gwinner (2011), Interior layered deposits within a perched basin, southern Coprates Chasma, Mars: Evidence for their formation, alteration, and erosion, *J. Geophys. Res.*, *116*, E02003, doi:10.1029/2010JE003695.
- Fuete, F., J. Flahaut, R. Stesky, E. Hauber, and A. P. Rossi (2014), Stratigraphy and mineralogy of Candor Mensa, West Candor Chasma, Mars: Insights into the geologic history of Valles Marineris, *J. Geophys. Res. Planets*, *119*, 331–354, doi:10.1002/2013JE004557.
- Gabasova, L. R., and E. S. Kite (2016), Sediment compaction on Mars and its effect on layer orientation, 47th Lunar and Planetary Science Conference, held March 21–25, 2016 at The Woodlands, Tex., LPI Contribution No. 1903, p. 1981.
- Gendrin, A., et al. (2005), Sulfates in Martian layered terrains: The OMEGA/Mars express view, *Science*, *307*(5715), 1587–1591.
- Golombek, M. P., et al. (2006), Erosion rates at the Mars Exploration Rover landing sites and long-term climate change on Mars, *J. Geophys. Res.*, *111*, E12S10, doi:10.1029/2006JE002754.
- Golombek, M. P., N. H. Warner, V. Ganti, M. P. Lamb, T. J. Parker, R. L. Fergason, and R. Sullivan (2014), Small crater modification on Meridiani Planum and implications for erosion rates and climate change on Mars, *J. Geophys. Res. Planets*, *119*, 2522–2547, doi:10.1002/2014JE004658.

- Gourronc, M., et al. (2014), One million cubic kilometers of fossil ice in Valles Marineris: Relicts of a 3.5 Gy old glacial landsystem along the Martian equator, *Geomorphology*, *204*, 235–255.
- Griffiths, C. M., C. Dyt, E. Paraschivoiu, and K. Liu (2001), SEDSIM in hydrocarbon exploration, in *Geologic Modeling and Simulation, Computer Appl. Earth Sci.*, edited by D. F. Merriam and J. C. Davis, pp. 71–97, Springer, USA.
- Grindrod, P. M., and N. H. Warner (2014), Erosion rate and previous extent of interior layered deposits on Mars revealed by obstructed landslides, *Geology*, *42*, 795–798.
- Grotzinger, J. P. (2014), Habitability, organic taphonomy, and the search for organic carbon on Mars, *Science*, *343*, 386–7.
- Grotzinger, J. P., and R. E. Milliken (2012), The sedimentary rock record of Mars: Distribution, origins, and global stratigraphy, in *Sedimentary Geology of Mars, SEPM Spec. Publ.*, vol. 102, edited by J. P. Grotzinger and R. E. Milliken, pp. 1–48, SEPM Society for Sedimentary Geology.
- Grotzinger, J. P., et al. (2014), A habitable fluvio-lacustrine environment at Yellowknife Bay, Gale crater, Mars, *Science*, *343*(6169), 1242777.
- Grotzinger, J. P., et al. (2015), Deposition, exhumation, and paleoclimate of an ancient lake deposit, Gale crater, Mars, *Science*, *350*, doi:10.1126/science.aac7575.
- Haberle, R. M., J. B. Pollack, J. R. Barnes, R. W. Zurek, C. B. Leovy, J. R. Murphy, H. Lee, and J. Schaeffer (1993), Mars atmospheric dynamics as simulated by the NASA Ames General Circulation Model: 1. The zonal-mean circulation, *J. Geophys. Res.*, *98*, 3093–3123, doi:10.1029/92JE02946.
- Haberle, R. M., J. R. Murphy, and J. Schaeffer (2003), Orbital change experiments with a Mars general circulation model, *Icarus*, *161*(1), 66–89.
- Halevy, I., and J. W. Head III (2014), Episodic warming of early Mars by punctuated volcanism, *Nat. Geosci.*, *7*(12), 865–868.
- Harrison, K. P., and M. G. Chapman (2008), Evidence for ponding and catastrophic floods in central Valles Marineris, Mars, *Icarus*, *198*, 351–364.
- Hayward, R. K., L. K. Fenton, and T. N. Titus (2014), Mars Global Digital Dune Database (MGD3): Global dune distribution and wind pattern observations, *Icarus*, *230*, 38–46, doi:10.1016/j.icarus.2013.04.011.
- Heermance, R. V., A. Pullen, P. Kapp, C. N. Garzione, S. Bogue, L. Ding, and P. Song (2013), Climatic and tectonic controls on sedimentation and erosion during the Pliocene-Quaternary in the Qaidam Basin (China), *Geol. Soc. Am. Bull.*, *125*, 833–856.
- Holt, J. W., K. E. Fishbaugh, S. Byrne, S. Christian, K. Tanaka, P. S. Russell, K. E. Herkenhoff, A. Safaeinili, N. E. Putzig, and R. J. Phillips (2010), The construction of Chasma Boreale on Mars, *Nature*, *465*, 446–449.
- Hore, A. (2015), Structural analysis, layer thickness measurements and mineralogical investigation of the large interior layered deposit within Ganges Chasma, Valles Marineris, Mars, M. Sci. thesis, Brock Univ., St. Catherine's, Ontario, Canada.
- Howard, A. D. (2007), Simulating the development of Martian highland landscapes through the interaction of impact cratering, fluvial erosion, and variable hydrologic forcing, *Geomorphology*, *91*(3–4), 332–363.
- Hynek, B. M., and R. J. Phillips (2008), The stratigraphy of Meridiani Planum, Mars, and implications for the layered deposits' origin, *Earth Planet. Sci. Lett.*, *274*(1–2), 214–220.
- Irwin, R. P., K. W. Lewis, A. D. Howard, and J. A. Grant (2015), Paleohydrology of Eberswalde crater, Mars, *Geomorphology*, *240*, 83–101.
- Isherwood, R. J., L. M. Jozwiak, J. C. Jansen, and J. C. Andrews-Hanna (2013), The volcanic history of Olympus Mons from paleo-topography and flexural modeling, *Earth Planet. Sci. Lett.*, *363*, 88–96.
- Jackson, M. P. A., et al. (1991), Salt diapirs of the Great Kavir, central Iran, *Geol. Soc. Am. Mem.*, *177*, 1–150.
- Jackson, M. P. A., J. B. Adams, T. P. Dooley, A. R. Gillespie, and D. R. Montgomery (2011), Modeling the collapse of Hebes Chasma, Valles Marineris, Mars, *Geol. Soc. Am. Bull.*, *123*(7–8), 1596.
- Jakosky, B. M., and M. H. Carr (1985), Possible precipitation of ice at low latitudes of Mars during periods of high obliquity, *Nature*, *315*, 559–561.
- Jakosky, B. M., and R. J. Phillips (2001), Mars' volatile and climate history, *Nature*, *412*(6843), 237–244.
- Karimi, S., A. J. Dombard, D. L. Buczkowski, S. J. Robbins, and R. M. Williams (2016), Using the viscoelastic relaxation of large impact craters to study the thermal history of Mars, *Icarus*, *272*, 102–113.
- Kass, D. M., Schofield, J. T., Michaels, T. I., Rafkin, S. C. R., Richardson, M. I., Toigo, A. D. (2003), Analysis of atmospheric mesoscale models for entry, descent, and landing, *J. Geophys. Res.*, *108*(E12), 8090, doi:10.1029/2003JE002065.
- Kerber, L., F. Forget, and R. Wordsworth (2015), Sulfur in the early Martian atmosphere revisited: Experiments with a 3-D Global Climate Model, *Icarus*, *261*, 133–148.
- Kinch, K. M., J. Sohl-Dickstein, J. F. Bell, J. R. Johnson, W. Goetz, and G. A. Landis (2007), Dust deposition on the Mars Exploration Rover Panoramic Camera (Pancam) calibration targets, *J. Geophys. Res.*, *112*, E06S03, doi:10.1029/2006JE002807.
- Kirk, R. L., et al. (2008), Ultrahigh resolution topographic mapping of Mars with MRO HiRISE stereo images: Meter-scale slopes of candidate Phoenix landing sites, *J. Geophys. Res.*, *113*, E00A24, doi:10.1029/2007JE003000.
- Kite, E. S., and D. P. Mayer (2016), Mars erosion rates constrained using crater counts, with applications to organic-matter preservation and to the global dust cycle, *Icarus*, doi:10.1016/j.icarus.2016.10.010.
- Kite, E. S., K. W. Lewis, M. P. Lamb, C. E. Newman, and M. I. Richardson (2013a), Growth and form of the mound in Gale Crater, Mars: Slope-wind enhanced erosion and transport, *Geology*, *41*, 543–546, doi:10.1130/G3309.1.
- Kite, E. S., I. Halevy, M. A. Kahre, M. Manga, and M. Wolff (2013b), Seasonal melting and the formation of sedimentary rocks on Mars, *Icarus*, *223*, 181–210.
- Kite, E. S., A. Howard, A. Lucas, J. C. Armstrong, O. Aharonson, and M. P. Lamb (2015), Stratigraphy of Aeolis Dorsa, Mars: Stratigraphic context of the great river deposits, *Icarus*, *253*, 223–242.
- Kocurek, G. (1988), First-order and super bounding surface in eolian sequences, *Sediment. Geol.*, *56*, 193–206.
- Kok, J. F., E. J. R. Parteli, T. I. Michaels, and D. B. Karam (2012), The physics of wind-blown sand and dust, *Rep. Prog. Phys.*, *75*, 106901.
- Krapf, C. (2003), Contrasting styles of ephemeral river systems and their interaction with dunes of the Skeleton Coast erg (Namibia), *Quat. Int.*, *104*, 41–52.
- Lapôtre, M. G. A., et al. (2016), Large wind ripples on Mars: A record of atmospheric evolution, *Science*, *353*, 55–58.
- Laskar, J., A. C. M. Correia, M. Gastineau, F. Joutel, B. Levrard, and P. Robutel (2004), Long term evolution and chaotic diffusion of the insolation quantities of Mars, *Icarus*, *170*, 343–364.
- Le Deit, L., S. Le Mouélic, O. Bourgeois, J.-P. Combe, D. Mège, C. Sotin, A. Gendrin, E. Hauber, N. Mangold, and J.-P. Bibring (2008), Ferric oxides in East Candor Chasma, Valles Marineris (Mars) inferred from analysis of OMEGA/Mars Express data: Identification and geological interpretation, *J. Geophys. Res.*, *113*, E07001, doi:10.1029/2007JE002950.
- Le Deit, L., Laetitia, E. Hauber, F. Fueten, M. Pondrelli, A. P. Rossi, and R. Jaumann (2013), Sequence of infilling events in Gale Crater, Mars: Results from morphology, stratigraphy, and mineralogy, *J. Geophys. Res. Planets*, *118*, 2439–2473, doi:10.1002/2012JE004322.
- Le Mouélic, S., et al. (2015), The ChemCam remote micro-imager at Gale crater: Review of the first year of operations on Mars, *Icarus*, *249*, 93–107.

- Leeder, M. R. (2011), *Sedimentology and Sedimentary Basins: From Turbulence to Tectonics*, 2nd ed., 784 pp., Wiley, Chichester, West Sussex, U. K.
- Levy, J. S., C. I. Fassett, and J. W. Head (2016), Enhanced erosion rates on Mars during Amazonian glaciation, *Icarus*, 264, 213–219.
- Lewis, K. W. (2009), The rock record of Mars: Structure, sedimentology and stratigraphy, PhD Thesis (California Institute of Technology).
- Lewis, K. W., and O. Aharonson (2014), Occurrence and origin of rhythmic sedimentary rocks on Mars, *J. Geophys. Res. Planets*, 119, 1432–1457, doi:10.1002/2013JE004404.
- Lewis, K. W., O. Aharonson, J. P. Grotzinger, R. L. Kirk, A. S. McEwen, and T.-A. Suer (2008), Quasi-periodic bedding in the sedimentary rock record of Mars, *Science*, 322, 1532.
- Lewis, K. W., J. P. Grotzinger, S. Gupta, and D. M. Rubin (2015), Investigation of a major stratigraphic unconformity with the Curiosity rover, Abstract P43B-2117 presented at 2015 Fall Meeting, AGU, San Francisco, Calif.
- Li, G., and K. Batygin (2014), On the spin-axis dynamics of a moonless Earth, *Astrophys. J.*, 790(1), doi:10.1088/0004-637X/790/1/69.
- Lissauer, J. J., J. W. Barnes, and J. E. Chambers (2012), Obliquity variations of a moonless Earth, *Icarus*, 217(1), 77–87.
- Loizeau, D., N. Mangold, F. Poulet, J.-P. Bibring, J. L. Bishop, J. Michalski, and C. Quantin (2015), History of the clay-rich unit at Mawrth Vallis, Mars: High-resolution mapping of a candidate landing site, *J. Geophys. Res. Planets*, 120, 1820–1846, doi:10.1002/2015JE004894.
- Lucchitta, B. K. (1990), Young volcanic deposits in the Valles Marineris, Mars, *Icarus*, 86, 476–509.
- Lucchitta, B. K. (2010), Lakes in Valles Marineris, in *Lakes on Mars*, edited by N. A. Cabrol and E. A. Grin, pp. 111–152, Elsevier B.V.
- Lucchitta, B. K. (2015), Geologic map of West Candor Chasma, Mars: A progress report, 46th Lunar and Planetary Science Conference, Woodlands, Tex., LPI Contribution No. 1832, p. 1550.
- Lucchitta, B. K., A. S. McEwen, G. D. Clow, P. E. Geissler, R. B. Singer, R. A. Schultz, and S. W. Squyres (1992), The canyon system on Mars, in *Mars*, edited by M. S. Matthews et al., pp. 453–492, Univ. Ariz. Press, Tucson.
- Madeleine, J.-B., F. Forget, J. W. Head, B. Levrard, F. Montmessin, and E. Millour (2009), Amazonian northern mid-latitude glaciation on Mars: A proposed climate scenario, *Icarus*, 203(2), 390–405.
- Mahrer, Y., and R. A. Pielke (1976), Numerical simulation of the airflow over Barbados, *Mon. Weather Rev.*, 104, 1392–1402.
- Malin, M. C., and K. S. Edgett (2000), Sedimentary rocks of early Mars, *Science*, 290, 1927–1937.
- Malin, M. C., et al. (2007), Context camera investigation on board the Mars Reconnaissance Orbiter, *J. Geophys. Res.*, 112, E05S04, doi:10.1029/2006JE002808.
- Malin, M. C., et al. (2010), The Mars Science Laboratory (MSL) Mast-mounted cameras (Mastcams) flight instruments, 41st Lunar and Planetary Science Conference, Abstract 1123.
- Mangold, N., A. Gendrin, B. Gondet, S. Le Mouélic, C. Quantin, V. Ansan, J.-P. Bibring, Y. Langevin, P. Masson, and G. Neukum (2008), Spectral and geological study of the sulfate-rich region of West Candor Chasma, Mars, *Icarus*, 194(2), 519–543.
- Mangold, N., L. Roach, R. Milliken, S. Le Mouélic, V. Ansan, J. P. Bibring, P. Masson, J. F. Mustard, S. Murchie, and G. Neukum (2010), A Late Amazonian alteration layer related to local volcanism on Mars, *Icarus*, 207(1), 265–276.
- Martin, R. L., and J. Kok (2016), Field-based observations confirm linear scaling of sand flux with wind stress, arXiv:1609.09458.
- Mayer, D. P., and E. S. Kite (2016), An integrated workflow for producing digital terrain models of Mars from CTX and HiRISE stereo data using the NASA Ames Stereo Pipeline, 47th Lunar and Planetary Science Conference, held March 21–25, 2016 at The Woodlands, Tex., LPI Contribution No. 1903, p. 1241.
- McCauley, J. F. (1978), Geologic map of the Coprates Quadrangle of Mars, U.S. Geol. Survey Misc. Inv. Series Map 1-897, scale 1: 5,000,000.
- McEwen, A. S., et al. (2007), Mars Reconnaissance Orbiter's High Resolution Imaging Science Experiment (HiRISE), *J. Geophys. Res.*, 112, E05S02, doi:10.1029/2005JE002605.
- McKay, C. P., and S. S. Nedell (1988), Are there carbonate deposits in the Valles Marineris, Mars?, *Icarus*, 73, 142–148.
- McLennan, S. M., and J. P. Grotzinger (2008), The sedimentary rock cycle of Mars, in *The Martian Surface—Composition, Mineralogy, and Physical Properties*, edited by J. Bell, 541 pp., Cambridge Univ. Press, Cambridge, U. K.
- Metz, J., J. Grotzinger, C. Okubo, and R. Milliken (2010), Thin-skinned deformation of sedimentary rocks in Valles Marineris, Mars, *J. Geophys. Res.*, 115, E11004, doi:10.1029/2010JE003593.
- Metz, J. M., J. P. Grotzinger, D. M. Rubin, K. W. Lewis, S. W. Squyres, and J. F. Bell (2009), Sulfate-rich eolian and wet interdune deposits, Erebus crater, Meridiani Planum, Mars, *J. Sediment. Res.*, 79(5), 247–264.
- Miall, A. (2010), *The Geology of Stratigraphic Sequences*, Springer, Heidelberg, Germany.
- Michaels, T. I., and S. C. R. Rafkin (2008), Meteorological predictions for candidate 2007 Phoenix Mars Lander sites using the Mars Regional Atmospheric Modeling System (MRAMS), *J. Geophys. Res.*, 113, E00A07, doi:10.1029/2007JE003013.
- Michalski, J., and P. B. Niles (2012), Atmospheric origin of Martian interior layered deposits: Links to climate change and the global sulfur cycle, *Geology*, 40, 419–422.
- Milliken, R. E., et al. (2008), Opaline silica in young deposits on Mars, *Geology*, 36(11), 847–850.
- Milliken, R. E., J. P. Grotzinger, and B. J. Thomson (2010), Paleoclimate of Mars as captured by the stratigraphic record in Gale Crater, *Geophys. Res. Lett.*, 37, L04201, doi:10.1029/2009GL041870.
- Milliken, R. E., R. C. Ewing, W. W. Fischer, and J. Hurowitz (2014), Wind-blown sandstones cemented by sulfate and clay minerals in Gale Crater, Mars, *Geophys. Res. Lett.*, 41, 1149–1154, doi:10.1002/2013GL059097.
- Mischna, M. A., M. I. Richardson, R. J. Wilson, and D. J. McCleese (2003), On the orbital forcing of Martian water and CO₂ cycles: A general circulation model study with simplified volatile schemes, *J. Geophys. Res.*, 108(E6), 5062, doi:10.1029/2003JE002051.
- Mischna, M. A., V. Baker, R. Milliken, M. Richardson, and C. Lee (2013), Effects of obliquity and water vapor/trace gas greenhouses in the early Martian climate, *J. Geophys. Res. Planets*, 118, 560–576, doi:10.1002/jgre.20054.
- Montgomery, D. R., M. P. A. Jackson, B. C. Schreiber, A. R. Gillespie, and J. B. Adams (2009), Continental-scale salt tectonics on Mars and the origin of Valles Marineris and associated outflow channels, *GSA Bull.*, 121(1/2), 117–133, doi:10.1130/B26307.1.
- Moore, J. M., and A. D. Howard (2005), Large alluvial fans on Mars, *J. Geophys. Res.*, 110, E04005, doi:10.1029/2004JE002352.
- Moratto, Z. M., M. J. Broxton, R. A. Beyer, M. Lundy, and K. Husmann (2010), Ames Stereo Pipeline, NASA's open source automated stereogrammetry software, 41st Lunar and Planetary Science Conference, held March 1–5, 2010 in The Woodlands, Tex., LPI Contribution No. 1533, p. 2364.
- Moreau, A. J. M., R. M. Haberle, S. C. R. Rafkin, M. A. Kahre, and J. L. Hollingsworth (2014), Dust erosion and sedimentation patterns in Gale Crater as simulated by the Mars Regional Atmospheric Modeling System (MRAMS), Eighth International Conference on Mars, Abstract 1430.
- Mars Science Laboratory (MSL) Extended Mission Plan (2014), (led by Erickson, J. & Grotzinger, J.P.), Mars Science Laboratory Senior Review Proposal/Extended Missions Plan, Mission to Mt. Sharp: Habitability, Preservation of Organics, and Environmental Transitions, NASA/JPL. [Available at <http://mars.nasa.gov/files/msl/2014-MSL-extended-mission-plan.pdf>.]

- Murchie, S., et al. (2009), Evidence for the origin of layered deposits in Candor Chasma, Mars, from mineral composition and hydrologic modeling, *J. Geophys. Res.*, *114*, E00D05, doi:10.1029/2009JE003343.
- Murchie, S. L., et al. (2009), A synthesis of Martian aqueous mineralogy after 1 Mars year of observations from the Mars Reconnaissance Orbiter, *J. Geophys. Res.*, *114*, E00day, doi:10.1029/2009JE003342.
- Nedell, S. S., S. W. Squyres, and D. W. Andersen (1987), Origin and evolution of the layered deposits in the Valles Marineris, Mars, *Icarus*, *70*, 409–441.
- Neuffer, D. P., and R. A. Schultz (2006), Mechanisms of slope failure in Valles Marineris, Mars, *Quart. J. Eng. Geol. Hydrogeol.*, *39*, 227–240.
- Newman, C. E., S. R. Lewis, and P. L. Read (2005), The atmospheric circulation and dust activity in different orbital epochs on Mars, *Icarus*, *174*(1), 135–160.
- Niles, P. B., and J. Michalski (2009), Meridiani Planum sediments on Mars formed through weathering in massive ice deposits, *Nat. Geosci.*, *2*(3), 215–220.
- Okubo, C. H. (2010), Structural geology of Amazonian-aged layered sedimentary deposits in southwest Candor Chasma, Mars, *Icarus*, *207*(1), 210–225.
- Okubo, C. H. (2014), Bedrock geologic and structural map through the western Candor Colles region of Mars: U.S. Geological Survey Scientific Investigations Map 3309, pamphlet 8, scale 1:18,000, doi:10.3133/sim3309.
- Okubo, C. H., K. W. Lewis, A. S. McEwen, and R. L. Kirk (2008), Relative age of interior layered deposits in southwest Candor Chasma based on high-resolution structural mapping, *J. Geophys. Res.*, *113*, E12002, doi:10.1029/2008JE003181.
- Olsen, A. A., and J. D. Rimstidt (2007), Using a mineral lifetime diagram to evaluate the persistence of olivine on Mars, *Am. Mineral.*, *92*(4), 598–602.
- Palucis, M., W. E. Dietrich, R. M. E. Williams, A. G. Hayes, T. Parker, D. Y. Sumner, N. Mangold, K. Lewis, and H. Newsom (2016), Sequence and relative timing of large lakes in Gale crater (Mars) after the formation of Mt. Sharp, *J. Geophys. Res. Planets*, *121*, 472–496, doi:10.1002/2015JE004905.
- Parish, T. R., and D. H. Bromwich (1991), Continental-scale simulation of the Antarctic katabatic wind regime, *J. Clim.*, *4*(2), 135–146.
- Parker, T. J., W. E. Dietrich, M. C. Palucis, F. J. Calef III, and H. E. Newsom (2014), Banding in Mount Sharp, Gale crater: Stratigraphy, strandlines, or buttress unconformities?, Abstract P43D-4013 presented at 2014 Fall Meeting, AGU, San Francisco, Calif.
- Peralta, J., F. Fueten, R. Cheel, R. Stesky, J. Flahaut, and E. Hauber (2015), Layer attitude and thickness measurements in western portion of the Ophir Chasma interior layered deposit, Valles Marineris, Mars, 46th Lunar and Planetary Science Conference, held March 16–20, 2015 in The Woodlands, Tex., LPI Contribution No. 1832, p. 1153.
- Perkins, J. P., N. J. Finnegan, and S. L. de Silva (2015), Amplification of bedrock canyon incision by wind, *Nat. Geosci.*, *8*, 305–310.
- Peterson, C. M. (1981), Hebes Chasma—Martian Pyroclastic Sink, *Lunar Planet. Sci. Conf.*, *12*, 828–829.
- Pyle, D. M. (1998), Forecasting sizes and repose times of future extreme volcanic events, *Geology*, *26*(4), 367.
- Rafkin, S. C. R., and T. I. Michaels (2003), Meteorological predictions for 2003 Mars Exploration Rover high-priority landing sites, *J. Geophys. Res.*, *108*(E12), 8091, doi:10.1029/2002JE002027.
- Rafkin, S. C. R., R. M. Haberle, and T. I. Michaels (2001), The Mars Regional Atmospheric Modeling System (MRAMS): Model description and selected simulations, *Icarus*, *151*, 228–256.
- Rafkin, S. C. R., J. Pla-Garcia, M. Kahre, J. Gomez-Elvira, V. E. Hamilton, M. Marin, S. Navarro, J. Torres, and A. Vasavada (2016), The meteorology of Gale Crater as determined from Rover Environmental Monitoring Station observations and numerical modeling. Part II: Interpretation, *Icarus*, doi:10.1016/j.icarus.2016.01.031, in press.
- Ramirez, R. M., and J. F. Kasting (2017), Could cirrus clouds have warmed early Mars?, *Icarus*, *281*, 248–261.
- Ramirez, R., R. Kopparapu, M. E. Zugger, T. D. Robinson, R. Freedman, and J. F. Kasting (2014), Warming early Mars with CO₂ and H₂, *Nat. Geosci.*, *7*, 59–63.
- Richardson, M. I., A. D. Toigo, and C. E. Newman (2007), PlanetWRF: A general purpose, local to global numerical model for planetary atmospheric and climate dynamics, *J. Geophys. Res.*, *112*, E09001, doi:10.1029/2006JE002825.
- Roach, L. H. (2009), Sulfates in Valles Marineris as indicators of the aqueous evolution of Mars, PhD thesis, Brown University.
- Roach, L. H., J. F. Mustard, M. D. Lane, J. L. Bishop, and S. L. Murchie (2010), Diagenetic haematite and sulfate assemblages in Valles Marineris, *Icarus*, *207*, 659–674.
- Rossi, A. P., G. Neukum, M. Pondrelli, S. van Gasselt, T. Zegers, E. Hauber, A. Chicarro, and B. Foing (2008), Large-scale spring deposits on Mars?, *J. Geophys. Res.*, *113*, E08016, doi:10.1029/2007JE003062.
- Rubin, D. M., and R. E. Hunter (1982), Bedform climbing in theory and nature, *Sedimentology*, *29*, 121–138.
- Schmidt, G. (2016), Geology of Hebes Chasma, Valles Marineris, Mars, MSci thesis, Brock University.
- Schmidt, G., J. Flahaut, F. Fueten, E. Hauber, and R. Stesky (2015), Evidence for an unconformity within the interior layered deposit of Hebes Chasma, Valles Marineris, Mars, 46th Lunar and Planetary Science Conference, held March 16–20, 2015 in The Woodlands, Tex., LPI Contribution No. 1832, p. 1237.
- Schultz, R. A. (2002), Stability of rock slopes in Valles Marineris, Mars, *Geophys. Res. Lett.*, *29*(19), 1932, doi:10.1029/2002GL015728.
- Segura, T. L., K. Zahnle, O. B. Toon, and C. P. McKay (2013), The effects of impacts on the climates of terrestrial planets, in *Comparative Climatology of Terrestrial Planets*, edited by S. J. Mackwell et al., pp. 417–438, Univ. Ariz. Press, Tucson.
- Shao, Y. (2008), *Physics and Modeling of Wind Erosion*, 2nd ed., Springer, New York.
- Sharp, R. P. (1940), Ep-Archean and Ep-Algonkian erosion surfaces, Grand Canyon, Arizona, *Geol. Soc. Am. Bull.*, *51*, 1235–1269.
- Shean, D. E., O. Alexandrov, Z. M. Moratto, B. E. Smith, I. R. Joughin, C. Porter, and P. Morin (2016), An automated, open-source pipeline for mass production of digital elevation models (DEMs) from very-high-resolution commercial stereo satellite imagery, *ISPRS J. Photogramm. Remote Sens.*, *116*, 101–117.
- Sklar, L., and W. E. Dietrich (1998), River longitudinal profiles and bedrock incision models: Stream power and the influence of sediment supply, in *Rivers Over Rock: Fluvial Processes in Bedrock Channels*, *Geophys. Monogr. Ser.*, vol. 107, edited by J. Tinkler and E. Wohl, pp. 237–260, AGU, Washington, D. C.
- Sklar, L. S., and W. E. Dietrich (2006), The role of sediment in controlling steady-state bedrock channel slope: Implications of the saltation abrasion incision model, *Geomorphology*, *82*(1–2), 58–83.
- Silvestro, S., D. A. Vaz, R. C. Ewing, A. P. Rossi, L. K. Fenton, T. I. Michaels, J. Flahaut, and P. E. Geissler (2013), Pervasive aeolian activity along rover Curiosity's traverse in Gale Crater, Mars, *Geology*, *41*, 483–486.
- Sloss, L. L. (1963), Sequences in the Cratonic Interior of North America, *Geol. Soc. Am. Bull.*, *74*, 93.
- Soto, A., M. Mischna, T. Schneider, C. Lee, and M. Richardson (2015), Martian atmospheric collapse: Idealized GCM studies, *Icarus*, *250*, 553–569.

- Spiga, A. (2011), Elements of comparison between Martian and terrestrial mesoscale meteorological phenomena: Katabatic winds and boundary layer convection, *Planet. Space Sci.*, 59(10), 915–922.
- Spiga, A., F. Forget, J.-B. Madeleine, L. Montabone, S. R. Lewis, and E. Millour (2011), The impact of Martian mesoscale winds on surface temperature and on the determination of thermal inertia, *Icarus*, 212, 504–519.
- Stopar, J. D., G. Jeffrey Taylor, V. E. Hamilton, L. Browning (2006), Kinetic model of olivine dissolution and extent of aqueous alteration on Mars, *Geochim. Cosmochim. Acta*, 70, 6136–6152.
- Stack, K. M., J. P. Grotzinger, and R. E. Milliken (2013), Bed thickness distributions on Mars: An orbital perspective, *J. Geophys. Res. Planets*, 118, 1323–1349, doi:10.1002/jgre.20092.
- Stack, K. M., et al. (2016), Comparing orbiter and rover image-based mapping of an ancient sedimentary environment, Aeolis Palus, Gale crater, Mars, *Icarus*, 280, 3–21, doi:10.1016/j.icarus.2016.02.024.
- Straub, K. M., C. Paola, D. Mohrig, M. A. Wolinsky, and T. George (2009), Compensational stacking of channelized sedimentary deposits, *J. Sediment. Res.*, 79(9), 673–688.
- Thollet, P., et al. (2012), Most Mars minerals in a nutshell: Various alteration phases formed in a single environment in Noctis Labyrinthus, *J. Geophys. Res.*, 117, E00J06, doi:10.1029/2011JE004028.
- Thomson, B. J., N. T. Bridges, R. Milliken, A. Baldridge, S. J. Hook, J. K. Crowley, G. M. Marion, C. R. de Souza Filho, A. J. Brown, and C. M. Weitz (2011), Constraints on the origin and evolution of the layered mound in Gale Crater, Mars using Mars Reconnaissance Orbiter data, *Icarus*, 214, 413–432.
- Toigo, A. D., C. Lee, C. E. Newman, and M. I. Richardson (2012), The impact of resolution on the dynamics of the Martian global atmosphere: Varying resolution studies with the MarsWRF GCM, *Icarus*, 227(1), 276–288.
- Tyler, D., and J. R. Barnes (2015), Convergent crater circulations on Mars: Influence on the surface pressure cycle and the depth of the convective boundary layer, *Geophys. Res. Lett.*, 42, 7343–7350, doi:10.1002/2015GL064957.
- Urata, R. A., and O. B. Toon (2013), Simulations of the martian hydrologic cycle with a general circulation model: Implications for the ancient martian climate, *Icarus*, 226(1), 229–250.
- Wang, Z.-T., H.-T. Wang, Q.-H. Niu, Z.-B. Dong, and T. Wang (2011), Abrasion of yardangs, *Phys. Rev. E*, 84, 031304.
- Watkins, J. A., J. Grotzinger, N. Stein, S. G. Banham, S. Gupta, D. Rubin, K. M. Stack, and K. S. Edgett (2016), 47th Lunar and Planetary Science Conference, held March 21–25, 2016 at The Woodlands, Tex., LPI Contribution No. 1903, p. 2939.
- Weitz, C. M., and J. L. Bishop (2016), Stratigraphy and formation of clays, sulfates, and hydrated silica within a depression in Coprates Catena, Mars, *J. Geophys. Res. Planets*, 121, 805–835, doi:10.1002/2015JE004954.
- Weitz, C. M., M. D. Lane, M. Staid, and E. N. Dobrea (2008), Gray hematite distribution and formation in Ophir and Candor chasmata, *J. Geophys. Res.*, 113, E02016, doi:10.1029/2007JE002930.
- Weitz, C. M., E. Noe Dobrea, and J. J. Wray (2015), Mixtures of clays and sulfates within deposits in western Melas Chasma, Mars, *Icarus*, 251, 291–314.
- Wendt, L., C. Gross, T. Kneissl, M. Sowe, J.-P. Combe, L. Le Deit, P. C. McGuire, and G. Neukum (2011), Sulfates and iron oxides in Ophir Chasma, Mars, based on OMEGA and CRISM observations, *Icarus*, 213, 86–103.
- Williams, R. M. E., and C. M. Weitz (2014), Reconstructing the aqueous history within the southwestern Melas basin, Mars: Clues from stratigraphic and morphometric analyses of fans, *Icarus*, 242, 19–37.
- Wilson, S. A., A. D. Howard, J. M. Moore, and J. A. Grant (2007), Geomorphic and stratigraphic analysis of Crater Terby and layered deposits north of Hellas basin, Mars, *J. Geophys. Res.*, 112, E08009, doi:10.1029/2006JE002830.
- Wordsworth, R. D. (2016), The climate of early Mars, *Annu. Rev. Earth Planet. Sci.*, 44, 381–408.
- Wordsworth, R. D., L. Kerber, R. T. Pierrehumbert, F. Forget, and J. W. Head (2015), Comparison of “warm and wet” and “cold and icy” scenarios for early Mars in a 3-D climate model, *J. Geophys. Res. Planets*, 120, 1201–1219, doi:10.1002/2015JE004787.
- Wordsworth, R., F. Forget, E. Millour, J. Head, J.-B. Madeleine, and B. Charnay (2013), Global modelling of the early Martian climate under a denser CO₂ atmosphere: Water cycle and ice evolution, *Icarus*, 222, 1–19.
- Wylie, J. J., K. R. Helfrich, B. Dade, J. R. Lister, and J. F. Salzig (1999), Flow localization in fissure eruptions, *Bull. Volcanol.*, 60(6), 432–440.
- Zabrusky, K., J. C. Andrews-Hanna, and S. M. Wiseman (2012), Reconstructing the distribution and depositional history of the sedimentary deposits of Arabia Terra, Mars, *Icarus*, 220, 311–330.
- Zardi, D., and C. D. Whiteman (2013), Diurnal mountain wind systems, in *Mountain Weather Research and Forecasting, Recent Progress and Current Challenges*, edited by F. K. Chow, S. F. J. De Wekker, and B. J. Snyder, Springer, Berlin.
- Zimbelman, J., and S. Scheidt (2012), Hesperian Age for Western Medusae Fossae Formation, Mars, *Science*, 336, 1683.